Fabrication And Investigation of 3D Metallic Wire Weld Deposition Using Cold Metal Transfer Technique

A Thesis Submitted
In Partial Fulfilment of the Requirements
for the Degree of

DOCTOR OF PHILOSOPHY

in

Mechanical Engineering

by

Sudeep Kumar Jain
(2K19/PHDME/04)

Under the Supervision of

Dr. Qasim Murtaza	**Dr. Pushpendra Singh**
(Professor, DTU, Delhi)	**(Professor, DTU, Delhi)**

Department of Mechanical Engineering

DELHI TECHNOLOGICAL UNIVERSITY

(Formerly Delhi College of Engineering)
Shahbad Daulatpur, Main Bawana Road, Delhi-110042, India

November, 2024

CERTIFICATE

This is to certify that the thesis entitled **"Fabrication And Investigation of 3D Metallic Wire Weld Deposition Using Cold Metal Transfer Technique"** being submitted by **SUDEEP KUMAR JAIN**, Roll No. 2K19/PHDME/04 to the Delhi Technological University, Delhi for the award of the degree of **Doctor of Philosophy** is a bonafide record of original research work carried out by him. He has worked under our guidance and supervision and has fulfilled the requirements for the submission of this thesis, which has reached the requisite standard. The results contained in this thesis have not been submitted, in part or full, to any other University or Institute for the award of any degree or diploma.

Dr. Qasim Murtaza
Department of Mechanical Engineering
(Professor, DTU, Delhi)

Dr. Pushpendra Singh
Department of Mechanical Engineering
(Professor, DTU, Delhi)

ACKNOWLEDGEMENTS

Sudeep Kumar Jain
(2K19/PHDME/04)

CANDIDATE'S DECLARATION

I _**SUDEEP KUAMR JAIN** hereby certify that the work which is being presented in the thesis entitled **"Fabrication And Investigation of 3D Metallic Wire Weld Deposition Using Cold Metal Transfer Technique"** in partial fulfillment of the requirements for the award of the Degree of Doctor of Philosophy, submitted in the Department of _**Mechanical Engineering**_, Delhi Technological University is an authentic record of my own work carried out during the period from __**01-August-2019**__ to __**22-October-2024**__under the supervision of _**Prof. Qasim Murtaza** and **Prof. Pushpendra Singh**__.

The matter presented in the thesis has not been submitted by me for the award of any other degree of this or any other Institute.

Candidate's Signature

This is to certify that the student has incorporated all the corrections suggested by the examiners in the thesis and the statement made by the candidate is correct to the best of our knowledge.

Signature of Supervisor (s)

CERTIFICATE BY THE SUPERVISOR(s)

Certified that **Sudeep Kumar Jain** (2K19/PHDME/04) has carried out their research work presented in this thesis entitled **"Fabrication And Investigation of 3D Metallic Wire Weld Deposition Using Cold Metal Transfer Technique"** for the award of **Doctor of Philosophy** from Department of Mechanical Engineering, Delhi Technological University, Delhi, under our supervision. The thesis embodies results of original work, and studies are carried out by the student himself and the contents of the thesis do not form the basis for the award of any other degree to the candidate or to anybody else from this or any other University/Institution.

(**Dr. Qasim Murtaza**)
(Professor)
(DTU, Delhi)

(**Dr. Pushpendra Singh**)
(Professor)
(DTU, Delhi)

Date: **22-10-2024**

ABSTRACT

Additive Manufacturing (AM) has revolutionized product formation by minimizing material consumption and replacing traditional methods in some industries. Among various AM processes, Wire Arc Additive Manufacturing (WAAM) stands out for its high deposition rates, material efficiency, shorter lead times, and reduced inventory costs. Resembling welding, WAAM deposits layers to create large, complex parts, making it particularly valuable for high buy-to-fly ratio components in the aviation industry. Despite its lower equipment cost compared to other metal deposition AM processes, achieving defect-free parts with WAAM presents challenges such as deformation, cracking, porosity, and spatter. Significant research has been conducted to enhance material properties and strength, but further experimentation is needed. Future advancements in WAAM design will likely improve efficiency for specific applications, making WAAM a fast, cost-effective alternative for producing heavy metal parts. WAAM utilizes an electric arc as the primary heat source and solid wire as the material feedstock. The performance of WAAM is significantly influenced by various process parameters. Understanding and optimizing these parameters is crucial to achieving high-quality parts with desirable mechanical and structural properties. This study explores the impact of three input process parameters – current (I), welding speed (WS), and Contact Tip to Work Distance (CTWD) - each at three varying levels on three key mechanical properties of SS316L austenitic stainless steel WAAM samples. Through experimentation and analysis, the study evaluates three crucial mechanical properties: ultimate tensile strength (UTS), microhardness (MH), and residual stress (RS). The investigation uses Taguchi's Grey Relational Analysis method, employing an L9 orthogonal array design. Analysis of Variance (ANOVA) has been utilized to assess the impact of parameters on grey relational grade (GRG). A comprehensive set of characterization techniques, including Scanning Electron Microscopy (SEM), X-Ray Diffraction (XRD), and Energy Dispersive X-ray Spectroscopy (EDS), was employed to investigate the morphological attributes, elemental distribution, and crystalline configuration of the fabricated WAAM samples.

The findings from Grey Relational Analysis (GRA) highlight that optimal performance in terms of maximum UTS, MH, and RS is achieved when employing specific parameter configurations: a I (110 A), WS (0.7 m/min), and CTWD of (3 mm). The ANOVA analysis for the grey relational grade across various responses indicates that the current is the most significant factor, followed by welding speed and contact tip-to-work distance (CTWD). The contributions of current, welding speed, and CTWD are 76%, 21%, and 3%, respectively. X-ray CT results reveals that no porosity was present in either the WAAM or wrought steel samples.

Keywords: WAAM, CMT, SS 316L, Optimization, Grey Relational Analysis, XRD

TABLE OF CONTENTS

LIST OF FIGURES

LIST OF TABLES

LIST OF SYMBOLS, ABBREVIATIONS AND NOMENCLATURE

AM	Additive Manufacturing
WAAM	Wire Arc Additive Manufacturing
MAM	Metal Additive Manufacturing
SLM	Selective Laser Melting
EBM	Electron Beam Melting
SL	Sheet Lamination
DED	Directed Energy Deposition
MEX	Material Extrusion
VPP	Vat Photopolymerization
PBF	Powder Bed Fusion
BJT	Binder Jetting
MJT	Material Jetting
WLAM	Wire and Laser Additive Manufacturing
EBFF	Electron Beam Free Form Fabrication
CMT	Cold Metal Transfer
AC	Alternating Current
DC	Direct Current
GMAW	Gas Metal Arc Welding
GTAW	Gas Tungsten Arc Welding
SMAW	Shielded Metal Arc Welding
FCAW	Flux Cored Arc Welding
DCEP	Direct Current Electrode Positive
WFS	Wire Feed Speed
FCC	Face Centered Cubic
BCC	Body Centered Cubic
ANOVA	Analysis of variance
TS	Travel Speed
WFS	Wire Feed Speed

V	Voltage
I	Weld Current
WS	Welding Speed
CTWD	Contact Tip To Work Distance
OM	Optical Microscopy
SEM	Scanning Electron Microscope
XRD	X Ray Diffraction
GRA	Grey Relational Analysis
GRG	Grey Relational Grade
GRC	Grey Relational Coefficient
MADM	Multiple Attribute Decision Making
DOE	Design of Experiments
UTS	Ultimate Tensile Strength
YS	Yield Strength
PE	Percentage Elongation
RS	Residual Stress
DS	Debye Scherrer

List of Symbols

λ	Wavelength
x_{ij}	Normalized Value
y_{ij}	S/N ratio
γ	Grey Relational Coefficient
Δ_{ij}	Deviation Sequence
Γ	Grey Relational Grade
ε	distinguishing coefficient

1. Introduction

AM is a pivotal process in the fourth industrial revolution, widely recognized for its utility in industrial production, particularly in fabricating prototypes and models. AM technology's recent advancements have centered on creating complex aerospace components from nickel, titanium, aluminum, and stainless steel. This demonstrates its suitability for manufacturing medium to large-scale parts with tight tolerances. The AM process enables the fabrication of 3D parts with high deposition rates, reduced costs, optimal material utilization, enhanced quality, and near-net-shape accuracy, all guided by precise computer models.

AM has been used for advanced manufacturing processes to fabricate three-dimensional functional prototypes received directly from computer models.[1] AM enhances design flexibility, promotes weight savings, enables the production of complex components, and supports environmentally friendly manufacturing practices.[2] Additive Manufacturing (AM) is "a process where materials are combined to produce objects from 3D model data, typically layer by layer, differing from subtractive and formative manufacturing methods."[3] The AM process originated in the early 1980s, and by 1988, it was already being used in defense and aerospace applications, marking these fields as early adopters of the technology.[4] The growing need for intricate designs, complex shapes, superior material performance, and precise dimensional control in various industries has led to a significant shift toward utilizing AM processes for various applications.[5] AM provides multiple benefits, such as reduced material wastage, cost efficiency, quicker lead times, faster production, and an eco-friendly manufacturing process.[6] AM technologies are extensively used across industries like aerospace[7], automotive[8], construction[9], marine[10], and biomedical implants[11], utilizing various materials like metals[12], polymers[13], and

ceramics[14], and offering cost-effective manufacturing solutions for large, moderately complex parts.

The aerospace industry's use of AM is primarily driven by the expected growth in the aircraft market and the demand for titanium components. This sector requires developing AM techniques to replace conventional methods for producing significant components like wing ribs, stiffened panels, and cruciform.[15] Traditional manufacturing processes often result in significant material wastage when fabricating larger parts, leading to financial losses due to the high cost of materials used in aerospace and defense applications.[16] AM is fundamentally different from conventional processes like casting and forging, with its flexibility making it ideal for producing intricate parts. This flexibility also gives manufacturers greater supply chain adaptability, reducing part costs and lead times, particularly in workshop environments.[17] The main business drivers of additive manufacturing include reduced material waste and costs, enhanced design freedom, and customization. This technology has transformed projects across various sectors, including aerospace, energy, transportation, medical implants, and robotics.[18] The precedence research database estimates that the metal additive manufacturing market will generate $11.45 billion in revenue by 2030, as shown in Fig 1.1. The growing adoption of MAM technologies across industries like aerospace, automotive, healthcare, dental, and tool and molds, as well as in academic institutions, has driven demand for customized, complex, fully-dense metal parts with enhanced structural integrity and precision.[19] AM offers an easier and more economically viable solution than traditional manufacturing methods for processing and machining challenging materials like carbon steel, titanium, nickel, cobalt, and stainless steel.[20]
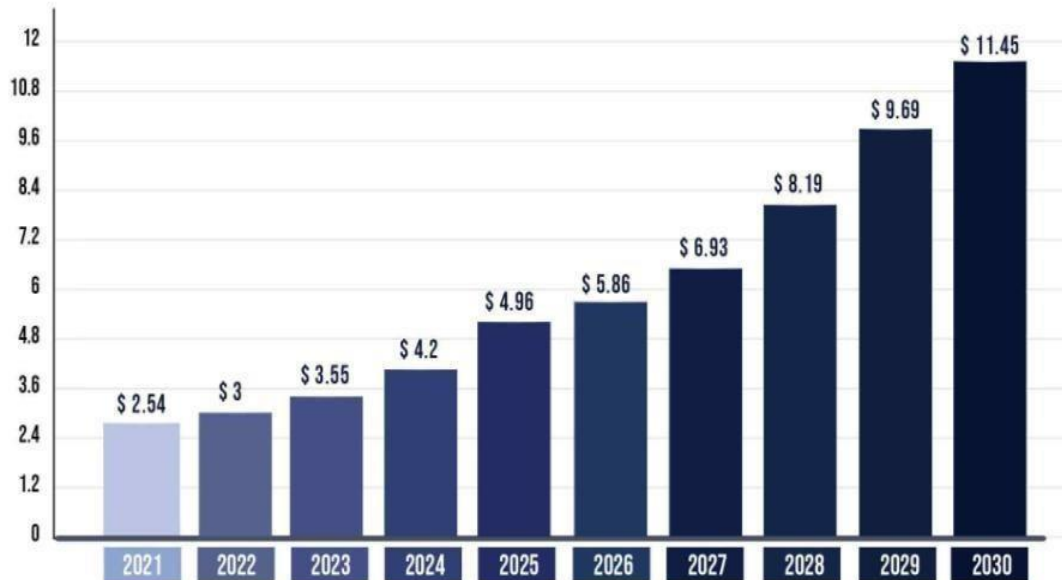
Fig 1.1 MAM Report (Precedence Research)[19]

The MAM field has seen significant research and business developments worldwide, carefully recorded over time. An AM system typically consists of a motion system, heat source, and feedstock, and its versatility makes it applicable to numerous applications.[21]

1.1 Classification of AM Processes

AM technology for metal deposition can be categorized into several types, such as SLM, BM, SL, and DED.[22] AM processes are classified according to the physical nature of the feed material and the method used to bind layers together in the final structure.[23] MAM involves melting metal powder or wire with a heat source and building the solid part layer by layer. Fig 1.2 shows the classification of the MAM process.
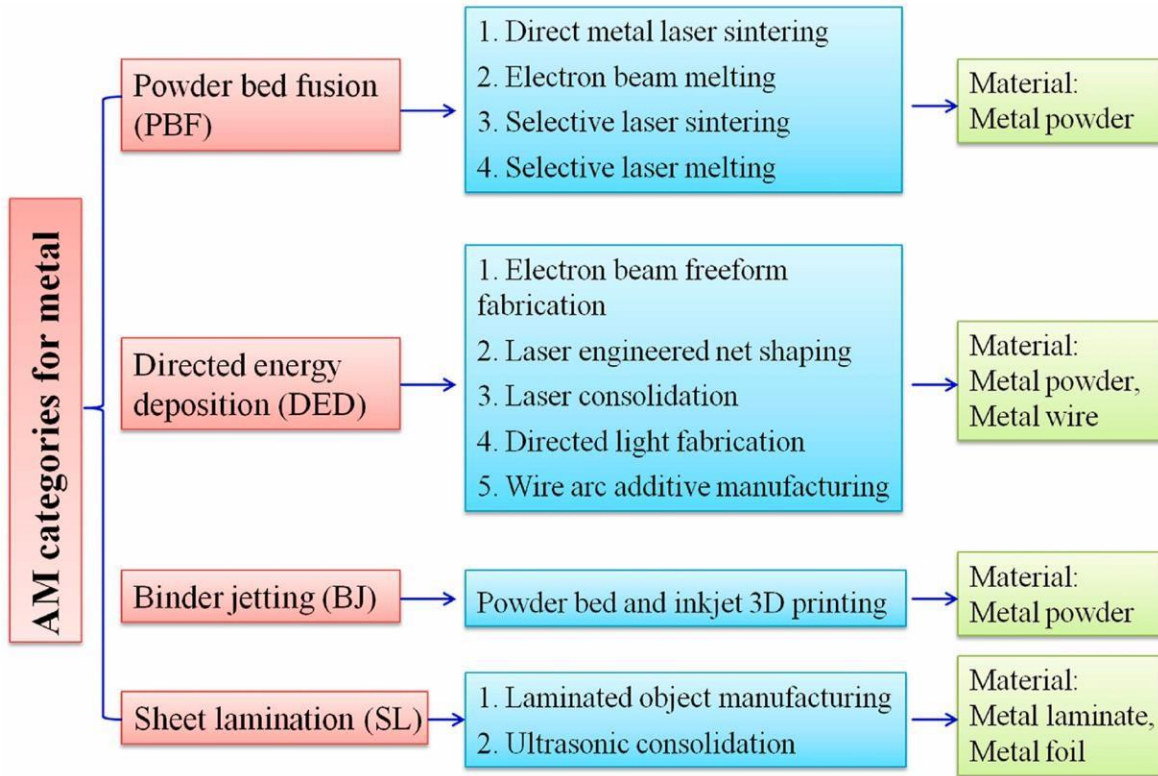
Fig 1.2 Metal Additive Manufacturing Classification [24]

AM processes are diverse in feedstock material, deposition strategy, and energy source, and can be categorized into liquid, powder, and solid-based systems. Analyzing the research and development of commercial AM systems over the past 20 years reveals the evolution of these technologies. In DED processes, the energy source and material feeder are typically integrated into a single print head that moves along the designated print path.[25]

1.2 Direct Energy Deposition

DED involves directing energy to targeted areas to heat the substrate, melting both the material and substrate, which is then deposited into the melt pool. This heat input can be supplied by a laser, electron, plasma arc or beam.[26] Energy sources play a key role in shaping the operational demands, potential applications, and complexity of DED processes. These processes enable the

construction of complete parts and are frequently employed for repairing or adding material to existing objects. The DED process utilizes feedstock in the form of wire or powder, both of which come with their own strengths and weaknesses. Powders are especially adaptable, covering most ceramic and metal materials, and are often preferred for their versatility. However, powder-based additive manufacturing faces significant challenges despite its flexibility, including safety concerns, high costs, and difficulties related to powder reusability and post-processing, which can limit its overall efficiency and practicality. The wire-based additive manufacturing process is simpler, quicker, and more cost-effective than the powder-based method. It offers the needed resolution and provides cost and energy efficiency advantages, especially for large-scale applications requiring near-net-shape production.[27] Fig 1.3 (a) & (b) depict the various DED processes. In the powder-based approach, powder is used in the feed system to create the part. Alternatively, the wire-fed process uses a laser beam for heating and wire as the feedstock material for depositing layers.
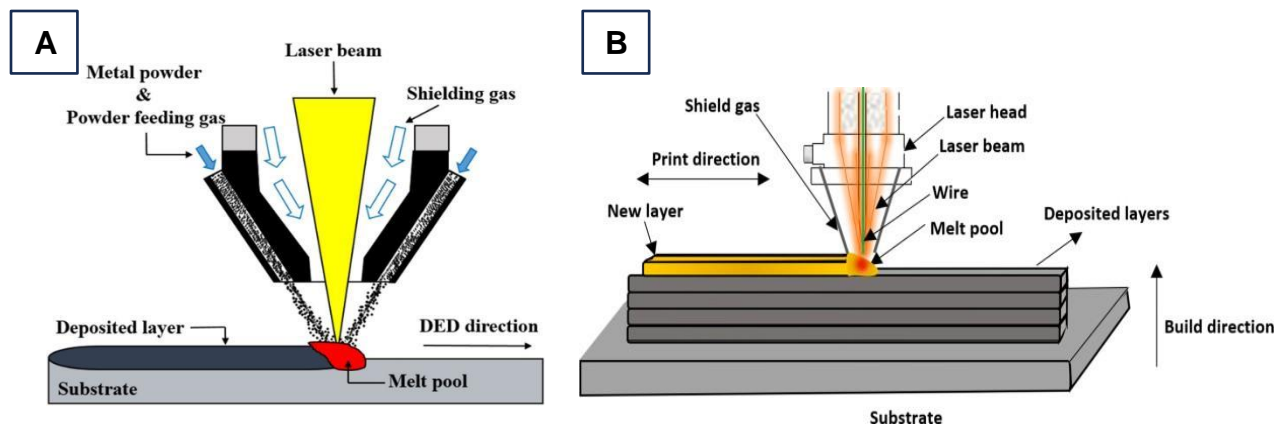
Fig 1.3 (A) Powder-Based DED [28], **(B) Laser-Based DED** [29]

DED techniques eliminate the need for specific tooling, unlike casting and forging, resulting in substantial reductions in manufacturing costs, especially for low production volumes

of parts typically forged. Additionally, DED methods can greatly reduce cycle time.[30] DED systems are employed in low production, rapid prototyping, and repair applications because they can effectively deposit and fuse material onto pre-existing parts.[31]

1.2.1 Powder-Based DED Process

Powder-based AM techniques create parts by adding material in discrete layers, following the design from a 3D CAD model. This method uses a laser, electron beam, or thermal beam to fuse metal powder spread over the top of each already joined layer[32] This approach prepares the next layer for processing, meaning the manufacturing is done in discrete steps rather than continuously. The powder is dispensed from a hopper and uniformly spread over the surface of the powder bed platform using a roller or blade. The layer thickness of dispersed powder varies based on the processing conditions and material properties. Powder sizes generally fall between 25 and 100 micrometers. The powder-based process finds applications in multiple automotive, aerospace, and medical industries. Its benefits encompass material versatility, appropriateness for prototyping, the ability to incorporate support structures, and a wide array of material possibilities.[33] According to ISO/ASTM 52900-2022, AM processes include various methods such as MEX[34], VPP[35], PBF[36], BJT[37], MJT[38], DED[39], and SL.teel's high heat absorption can pose challenges, particularly for less experienced welders, as excessive heat can lead to warping or distortion during the cooling phase. The solidification modes of stainless steel are depicted in Fig. 1.13, which illustrates the different regions on a constant iron vertical section of the Fe-Cr-Ni ternary diagram. In the primary ferrite solidification mode (FA mode), the process begins with the formation of primary ferrite, followed by a δ to γ phase transformation, often leaving residual δ-ferrite in the cell or dendrite core. Conversely, in the primary austenite solidification mode (AF mode), residual

δ-ferrite is typically found at the cell or dendrite boundaries. In practical applications, austenitic stainless-steel welds may exhibit either FA or AF solidification modes, largely influenced by the material's chemical composition and the welding process conditions. The Schaeffler equation, which utilizes Cr and Ni equivalents, is commonly used to predict the solidification mode of stainless steels.[86][40] The benefits of the powder-based additive manufacturing process include design freedom, suitability for prototypes, the ability to incorporate integrated support structures, and a wide range of material options. Fig 1.4 demonstrates the fundamental principle of this manufacturing process.
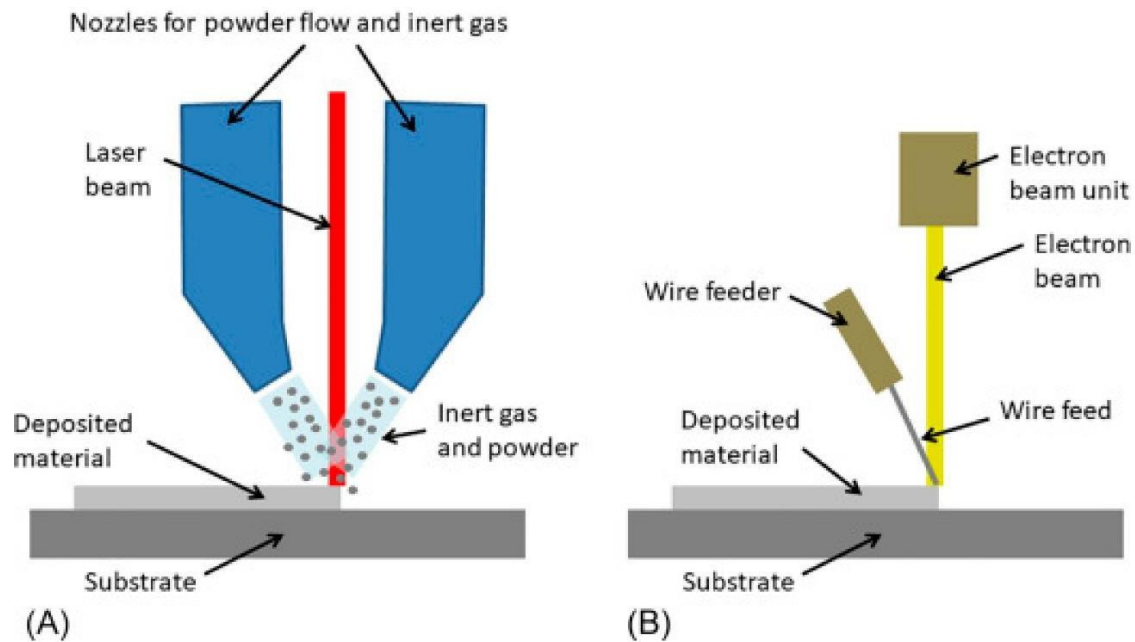
Fig 1.4 Types of Powder-Based Methods (A) Laser-Based (B) Electron-Beam Based[41]

1.2.2 Wire-Based DED Process

In the wire feed AM process, metal wire is used as the material to create components with moderate complexity. Deposition is carried out using various energy sources, including lasers, electric arcs,

and electron beams. The wire-feed additive manufacturing process can be divided into three different types: WAAM[42], WLAM[43], and EBFF.[44] The welding process focuses heat energy directly on the metal to be melted, enhancing efficiency. Wire-feed additive manufacturing is a leading technology for large-scale production, offering higher deposition rates, cost efficiency, shorter lead times, and a greener manufacturing solution. The wire-feed AM process offers several advantages, including producing high-quality parts, cost-effectiveness, reduced waste, and more straight forward repair operations. Various types of wire feed manufacturing processes are depicted in Fig 1.5.
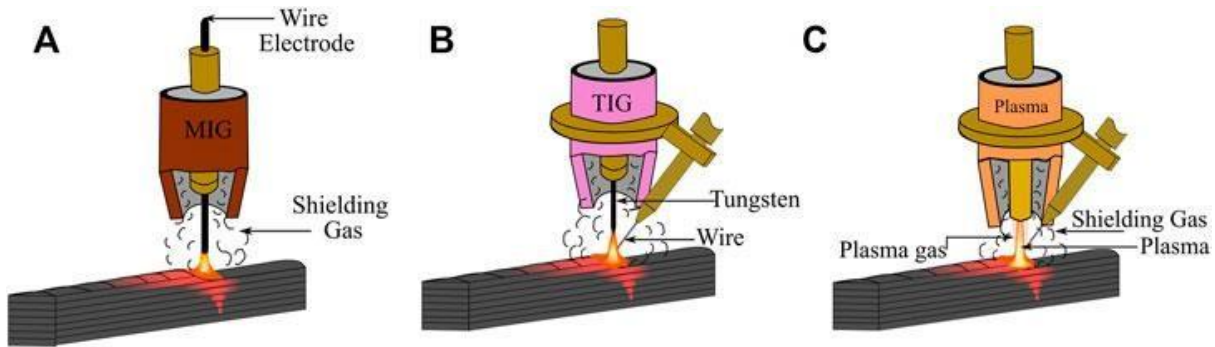
Fig. 1.5 Types of Wire Feed AM Process (A) MIG (B) TIG (C) Plasma Arc [45][51],

1.3 Wire Arc Additive Manufacturing

WAAM is a prominent method with the potential to revolutionize the production of medium to large-scale components. WAAM utilizes an electric arc as the heat source and wire as the feedstock to construct a fully formed 3D object[46]. WAAM employs various heat sources such as MIG, TIG, and PAW. A typical WAAM system comprises a computer interface, a robot controller, a power source, a wire feeder, and monitoring equipment[47]. Motion for the WAAM process is provided by either robotic systems or CNC gantries. This process is a welding-based technique

where metal layers are melted and deposited in an additive manner to form the component's final shape and size[48]. CMT is an advanced variation of the GMAW process, utilizing a controlled dip transfer mechanism that provides low heat input and eliminates spatter. This makes CMT machines ideal for depositing AM parts in the WAAM process [49]. WAAM can efficiently produce components from a broad range of materials, such as stainless steel[50], aluminum[51], titanium[52], copper[53], and cobalt[54]. The WAAM process is rapidly expanding its influence in the MAM market. It offers lower build and investment costs compared to laser-assisted MAM systems. The primary advantage of WAAM technology is its capability to produce customized metal components at higher deposition rates [55]. Laser-based and electron beam-based machines can deposit material at 2–10 g/min rates, whereas arc-based systems can achieve much higher 50–130 g/min rates due to their superior energy efficiency. Arc-based systems are 90% energy efficient, in contrast to the 30% to 50% efficiency of laser-based systems, with electron beam systems slightly outperforming laser systems in terms of efficiency [56]. The WAAM process introduces a higher level of complexity due to the need for precise wire feeding in the same direction. This requires careful management of torque, necessitating additional programming to ensure accuracy. The WAAM process introduces a higher level of complexity due to the need for precise wire feeding in the same direction. This requires careful management of torque, necessitating additional programming to ensure accuracy [57]. Therefore, the WAAM process serves as an essential approach for large-scale additive manufacturing, providing a reliable technique for creating simple structures that fulfill industrial requirements. The schematic diagram of this process is presented in Fig 1.6.
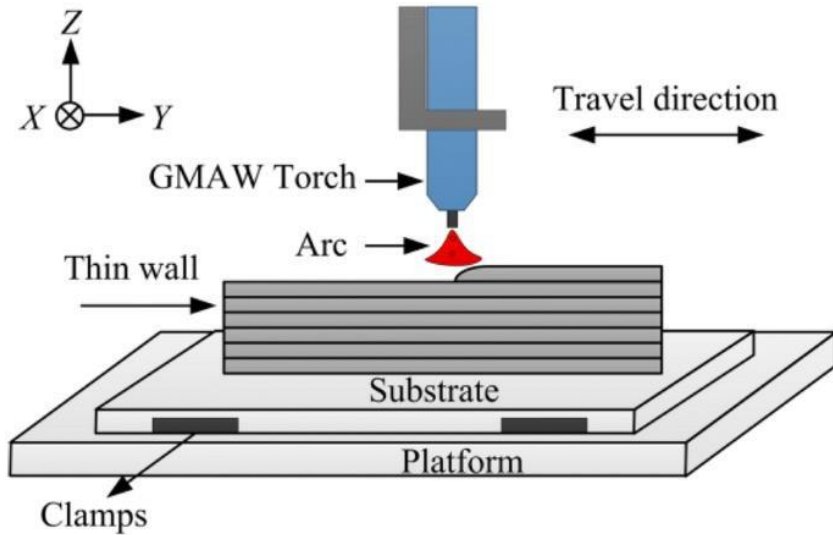
Fig. 1.6 Schematic of Wire Arc Additive Manufacturing (WAAM)[58]

1.3.1 Advantages of WAAM process

The WAAM process offers several benefits, including:

1. WAAM is capable of producing large-scale parts, solid shapes, and intricate structures at high deposition rates, achieving results in a relatively short time.

2. The WAAM technique enables the creation of complex geometries and diverse designs, offering greater design freedom. It also outperforms the powder feed process by achieving a higher deposition rate of up to 2500 cm³/h.

3. WAAM presents potential economic advantages, particularly when scaled up. It saves on material costs, eliminates the need for tooling, and reduces the amount of raw materials required to produce new parts.

4. WAAM is characterized by its high deposition volume, absence of size limitations, and excellent efficiency. It also offers low costs, shortened lead times, and superior structural integrity.

5. Arc-based heat sources provide numerous benefits over electron beam and laser heat sources, making them preferable for various applications.

6. The WAAM machine, based on open architecture designs, provides high deposition rates and is designed to be environmentally friendly. It operates in a non-hazardous environment and boasts a low BTF ratio.

7. The WAAM process is capable of depositing large components using a range of metals, including nickel, titanium, stainless steel, aluminum, and more.

8. WAAM processes utilize material more efficiently, with up to 100% of the wire material being deposited into the final parts.

1.3.2 Challenges in WAAM

1.3.3 Residual Stresses & Distortion

Residual stresses are internal stresses that remain in a component once external loads are no longer applied. If these stresses are not kept within certain limits, they can negatively affect the part's mechanical properties, geometrical tolerances, fatigue performance, and fracture resistance. The welding field frequently faces challenges with residual stresses, leading researchers to seek methods to reduce weld-induced stresses continuously.[59] Cracks will form in a component when residual stresses exceed the material's ultimate tensile strength, while plastic deformation occurs if the residual stress exceeds the material's yield strength.[60] In WAAM and other additive manufacturing techniques, distortion, and residual stresses frequently occur.[61] Optimizing process parameters such as current, voltage, feed speed, and inert gas flow is essential to manage these problems effectively.

1.3.4 Porosity

Porosity is another significant challenge in WAAM-manufactured parts, affecting their strength and fatigue performance and limiting their applications. The main causes of porosity are flawed raw materials [62] and flawed processes [63] in manufacturing. Porosity in WAAM products can be caused by moisture, impurities, and contaminants in the raw materials like wire and substrate. Process-induced porosity may arise from poor path planning and unstable deposition when creating complex geometrical components, resulting in inadequate fusion. Effective control of process-induced porosity involves optimizing process parameters, with a particular focus on shielding gas flow.[64]

1.3.5 Crack Formation and Layer Delamination

The formation of cracks in WAAM processes is determined by the thermal profile of the process and the deposition material's behavior. There are two primary types of cracks: solidification cracks, caused by disruptions in grain flow as the material solidifies, and grain boundary cracks, which form due to precipitate formation.[65] Cracks often align with the build direction and can contribute to corrosion issues. Delamination, which refers to the separation of adjacent layers, typically results from inadequate melting of deposited layers during the WAAM process.[66] This problem is more pronounced when processing bimetallic or multi-metal combinations.

1.3.6 Applications of WAAM

1. WAAM is proficient in creating medium-scale parts for a variety of industries, including aerospace, automotive, marine, and rapid tooling.

2. The WAAM process utilizes a diverse range of materials, including aluminum, copper, nickel, titanium, and stainless steel, for different applications.

3. By using WAAM, production time can be decreased by 40-60% and post-processing time can be cut by 15-20%, with the exact reductions varying based on part sizes.

4. The WAAM process can produce aerospace components from costly materials with a very low BTF and handle complex geometries effectively.

5. When used for manufacturing aircraft landing gear, the WAAM process can reduce raw material costs by 78% compared to conventional techniques.

6. WAAM technology ensures the creation of structures with complete density and without any cracks or defects.

7. In the WAAM process, the cost of filler wires is significantly lower compared to metal powders.

8. The intricate CMT-WAAM process requires attention to multiple aspects, such as process development, material quality, process monitoring, and online control.

1.4 Arc Welding for WAAM process

In arc welding, an electric arc produced by a power supply melts and joins metals. The power supply, which can be AC or DC, generates an arc between the base metal and a consumable electrode. The electrode is guided along the joint, either by hand or mechanically, to create the weld. This method of fusion welding relies on the arc's intense heat, reaching approximately 6500°F, to melt the metals and fuse them together.[67] Arc welding can be divided into four main types: GMAW, GTAW, SMAW, and FCAW. Shielding gas is used in arc welding to protect the molten pool and prevent welding defects. Arc welding, in its simplest form, is widely utilized

across numerous sectors, including aerospace, automotive, construction, marine, and oil & gas industries. It is regarded as a versatile and essential welding method for various applications, such as building ships, pipes, oil tanks, bridges, pressure vessels, and farm equipment. Arc welding offers several advantages, including high-speed welds, superior impact strength, and high deposition rates. It is also portable, produces high-quality welds, and can operate on both AC and DC power supplies. The schematic illustration of the arc welding process is presented in Fig 1.7.
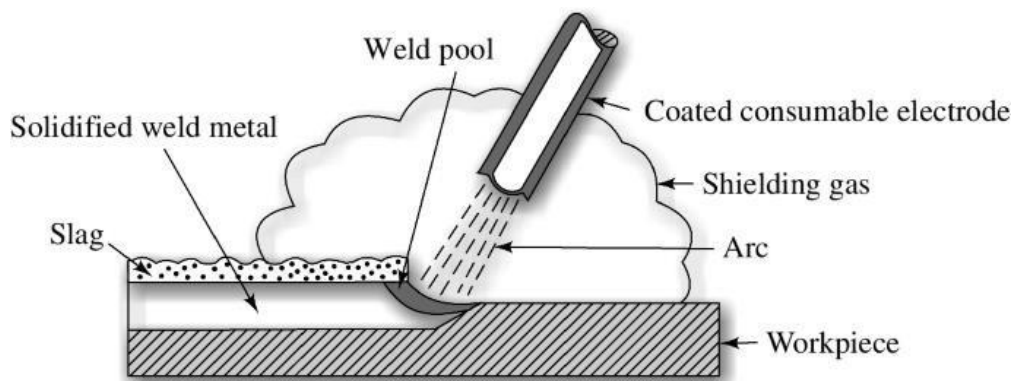
Fig. 1.7 Arc Welding Process [68]

1.4.1 Gas Metal Arc Welding (GMAW)

GMAW utilizes a continuous consumable wire electrode to create an electric arc between the torch and the workpiece, producing heat that melts both. The shielding gas protects the molten weld pool from atmospheric gases. The GMAW process typically uses DCEP.[69] GMAW offers steady, spatter-free material transfer, but the large weld pool generated necessitates keeping the workpiece horizontal to avoid gravitational issues. Common metal transfer modes in GMAW include short circuit, globular, spray, and pulsed-spray transfers.[70] Wire feed speed and voltage primarily influence the metal transfer mode in GMAW. Research indicates that various GMAW arc modes demonstrate superior mechanical properties at lower heat input levels in deposited parts.[71]

14

GMAW is typically used for various applications such as in the automotive industry, marine environments, pressure vessel manufacturing, construction projects, and repair tasks. A schematic representation of the GMAW process is shown in Fig 1.8.
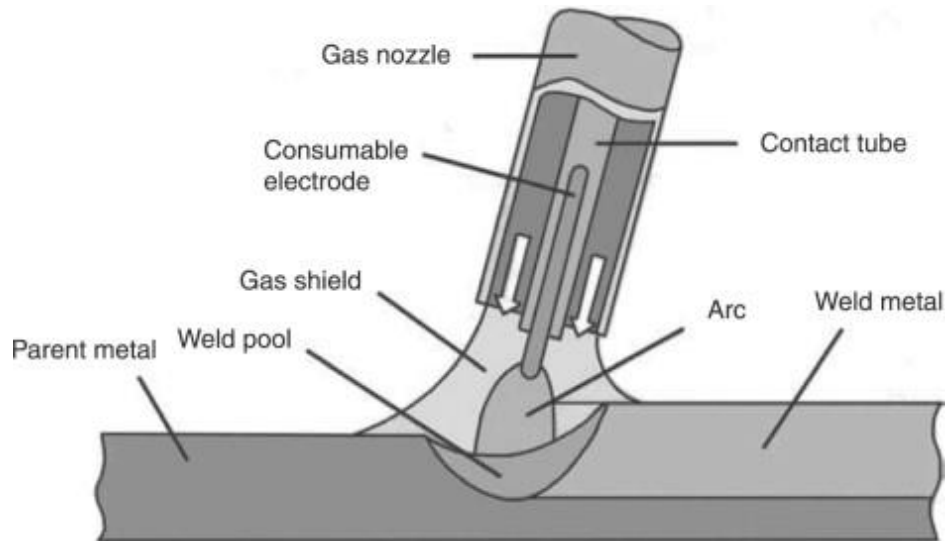
Fig. 1.8 Gas Metal Arc Welding (GMAW)[72]

1.4.2 Cold Metal Transfer (CMT)

CMT is an advanced variant of the conventional GMAW process, developed by Fronius International, Austria in 2004. It offers benefits such as reduced heat input, increased deposition rate, zero spatter, enhanced arc stability, and minimized distortion.[73] The CMT process facilitates the production of both thin and thick-walled components at a deposition rate of 2-3 kg/hr. It allows for precise control over various process parameters, including WFS, weld time, and shielding gas flow during the solidification phase. The process includes a reciprocating wire feed mechanism integrated into the electrical system, where an electrical controller synchronizes the stages of arc initiation and short-circuiting. In the CMT process, the welding operation consists of three phases: peak current, background current, and short-circuit phase. These phases occur in

repeated cycles throughout the welding duration.[74] The wire feed control system operates through several stages in the CMT process, as shown in Fig 1.9. The wire is initially fed toward the workpiece (a), then reversed when short-circuiting occurs (b). At this stage, the wire is retracted (c), and after the short circuit breaks, the wire speed is adjusted to continue feeding into the weld pool (d).
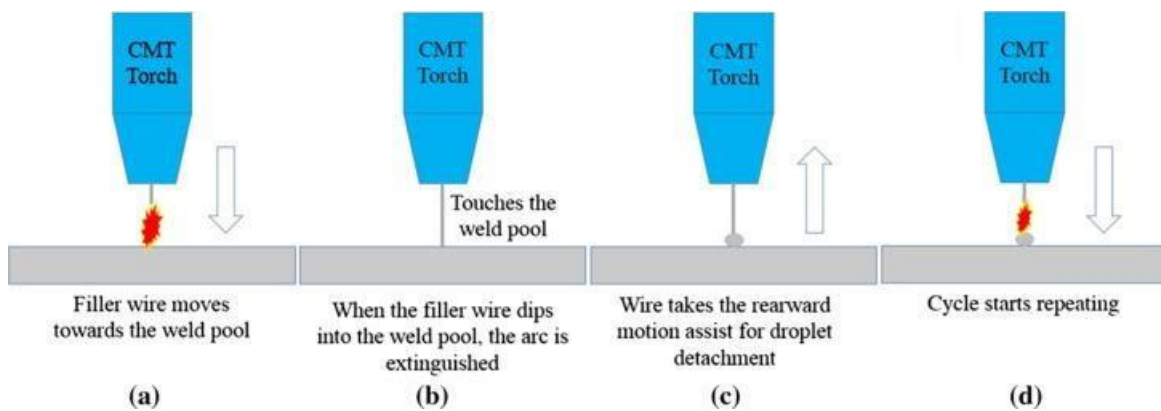
Fig. 1.9 CMT Mechanism [75]

The CMT process utilizes an innovative wire feed system combined with a six-axis manipulator to ensure uniform metal deposition with minimal thermal input.[76] The CMT process enables users to achieve optimal results when joining a variety of materials, including steel, aluminum, copper, cobalt, nickel, and titanium alloys.[77] The CMT process involves the following main steps: (i) arc initiation, (ii) short-circuiting current, (iii) wire withdrawal, and (iv) process continuation. During metal transfer, the short-circuit phase generates low heat input. In this mode, the power source heats the wire until it melts, and the increasing electromagnetic field around the wire induces a pinch effect that separates the molten metal from the electrode. As shown in Fig 1.10, when the welding wire contacts the weld pool, it delivers a molten drop. After

16

completing the cycle, the wire melts into the weld pool again, and the process repeats. This dip transfer, combined with short-circuiting, results in the lowest heat input of all transfer modes.
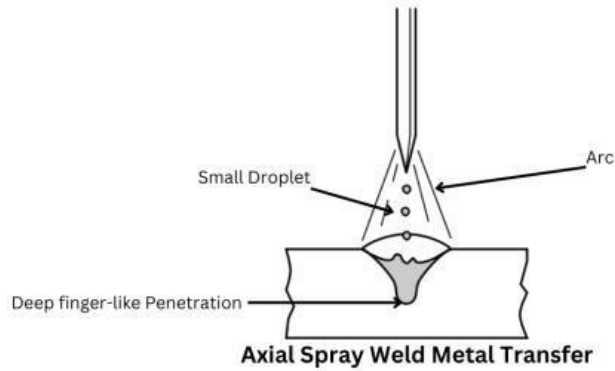
Fig. 1.10 Metal Transfer in Arc Welding [78]

The CMT process offers various waveforms in the latest CMT machines, as shown in Fig 1.11 (a) Standard CMT (b) CMT Pulse (c) CMT Advanced (d) CMT Pulse Advanced, to support future advancements in materials research. This enables the CMT process to deliver advantages such as reduced spatter, low heat input, and automatic adjustment of the electrode-to-sample distance.
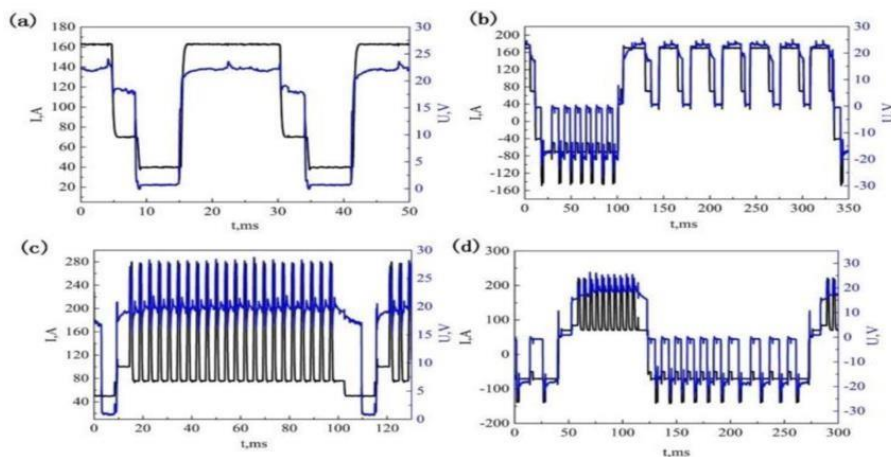
Fig 1.11. Waveforms in CMT[79]**: (a) Standard CMT, (b) CMT P, (c) CMT ADV and (d) CMT PADV**

1.4.3 CMT Advantages

1. CMT offers a low dilution ratio, higher deposition rate, faster cooling, well-synergized process, and spatter-free performance.

2. The latest MIG/MAG systems offer superior weld bead quality, reduced heat input, deeper penetration, and completely eliminate spatter.

3. The CMT method offers enhanced control over metal deposition through an advanced wire feed system, operating with low thermal heat input, allowing for drop-by-drop metal transfer.

4. Compared to standard MIG/MAG systems, the CMT process introduces ten times less heat into the weld joints.

5. CMT produces better bead profiles and smoother surfaces on components by utilizing its short-circuit phase and optimizing droplet transfer.

6. CMT offers reduced dilution, excellent penetration, low thermal input, a synergistic process, good fusion, and a controlled dip transfer mechanism.

7. CMT delivers exceptional mechanical properties, high welding speed, and excellent gap-bridging capabilities.

1.4.4 CMT Applications

1. The advanced CMT process produces superior welds, achieves faster welding rates, and joins dissimilar materials.

2. Thicker and thin materials are joined with low heat input and favorable arc properties, ensuring effective welding.

3. The CMT process ensures consistent arc deposition, minimal dilution, higher deposition rates, and optimal performance.

4. CMT is utilized across multiple sectors, such as automotive, aerospace, marine, and construction.

5. The CMT process is employed as a highly advanced technique for cladding, repair, and remanufacturing applications.

6. CMT is the preferred solution for manufacturing large-scale parts over an extended period.

1.5 316L Austenitic Stainless Steel

Stainless steel has emerged as a crucial category of engineering materials, extensively used across various applications. Iron-based alloys contain varying nickel, chromium, and molybdenum proportions.[80] Stainless steels are categorized into five primary types: austenitic, duplex, ferritic, martensitic, and precipitation hardening. Among these, austenitic stainless steels are commonly used due to their excellent corrosion resistance, ease of forming, and durability.[81] 316L stainless steel is the leading choice among austenitic stainless steels globally, known for its superior ductility, high-temperature creep resistance, and pitting resistance. It finds extensive application in aerospace, automotive, nuclear power plants, construction, pressure vessels, and biomedical implants.[82] Stainless steel is classified and assessed by adjusting alloying elements relative to the base 18Cr-8Ni system, exemplified by the 316L austenitic alloy (Sandmeyer steel). This alloy predominantly features an FCC lattice structure in the Austenite phase (γ) and, depending on its

chemical makeup and cooling conditions, may also include a minor BCC Ferrite phase (δ), as shown in Fig 1.12.
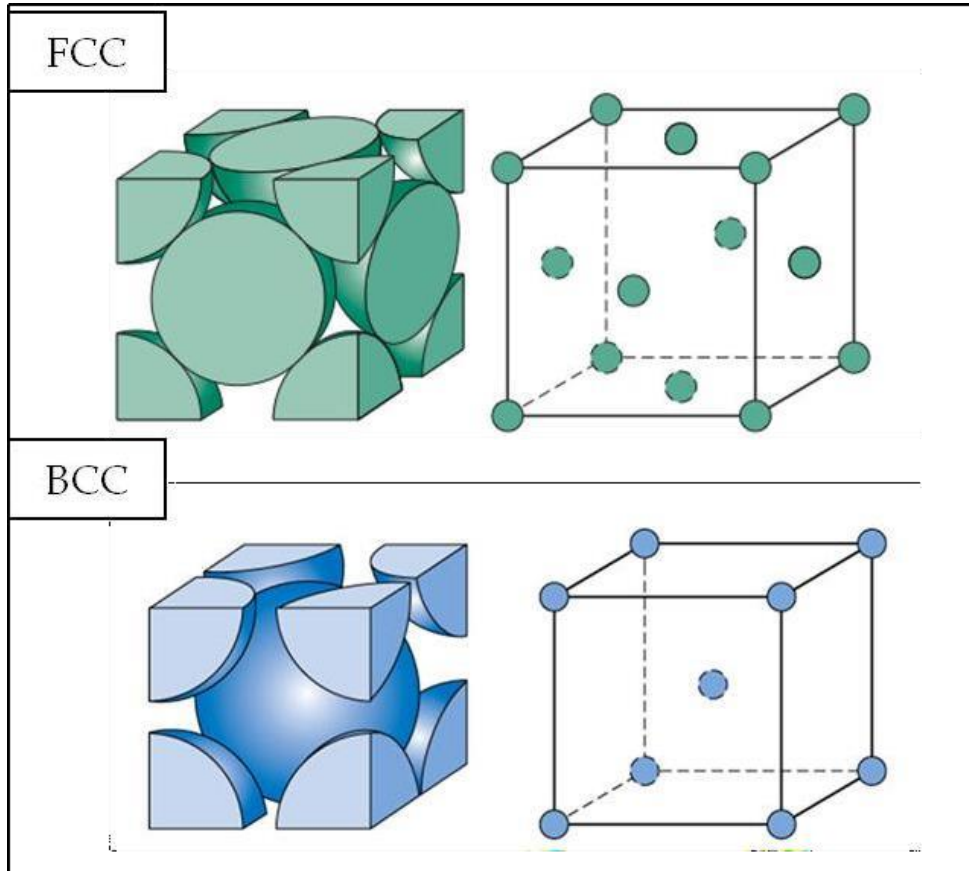
Fig 1.12. Crystal Structure of 316L Alloy[83]**, FCC - γ Austenite, BCC - δ Ferrite**

To meet the needs of applications requiring low magnetic permeability, high toughness at cryogenic temperatures, and resistance to corrosion that targets the δ phase, it is important to limit δ phase formation. Even a small amount of δ phase contributes to strengthening by decreasing austenite grain sizes and creating dislocation obstacles through ferrite grain subdivision. Moreover, the low carbon content of 316L stainless steel helps avoid sensitization during high-temperature operations such as welding.[84]

1.5.1 316L Stainless Steel in Welding

316L stainless steel remains increasingly popular due to its strength at high temperatures and its corrosion resistance. MIG, TIG, and resistance welding are techniques used to join 316L stainless steel.[85] The extent of microstructural changes and their impact on the welded product are critical factors. Stainless steel's high heat absorption can pose challenges, particularly for less experienced welders, as excessive heat can lead to warping or distortion during the cooling phase. The solidification modes of stainless steel are depicted in Fig. 1.13, which illustrates the different regions on a constant iron vertical section of the Fe-Cr-Ni ternary diagram. In the primary ferrite solidification mode (FA mode), the process begins with the formation of primary ferrite, followed by a δ to γ phase transformation, often leaving residual δ-ferrite in the cell or dendrite core. Conversely, in the primary austenite solidification mode (AF mode), residual δ-ferrite is typically found at the cell or dendrite boundaries. In practical applications, austenitic stainless-steel welds may exhibit either FA or AF solidification modes, largely influenced by the material's chemical composition and the welding process conditions. The Schaeffler equation, which utilizes Cr and Ni equivalents, is commonly used to predict the solidification mode of stainless steels.[86] The solidification modes, based on the chemical composition,

A mode: Creq/Nieq < 1.25,

A-F mode: 1.25< Creq/Nieq < 1.48,

F- A mode: 1.48< Creq/Nieq < 1.95

F mode: Creq/Nieq > 1.95

Where, Creq/Nieq is determined using the Schaeffler formula, which is calculated through the following equation:

$$Creq = Cr + Mo + (1.5 \text{ x } Si) + (0.5 \text{ x } Nb)$$

$$Nieq = Ni + (30 \text{ x } C) + (0.5 \text{ x } Mn)$$

Where A-Austenite & F-Ferrite.
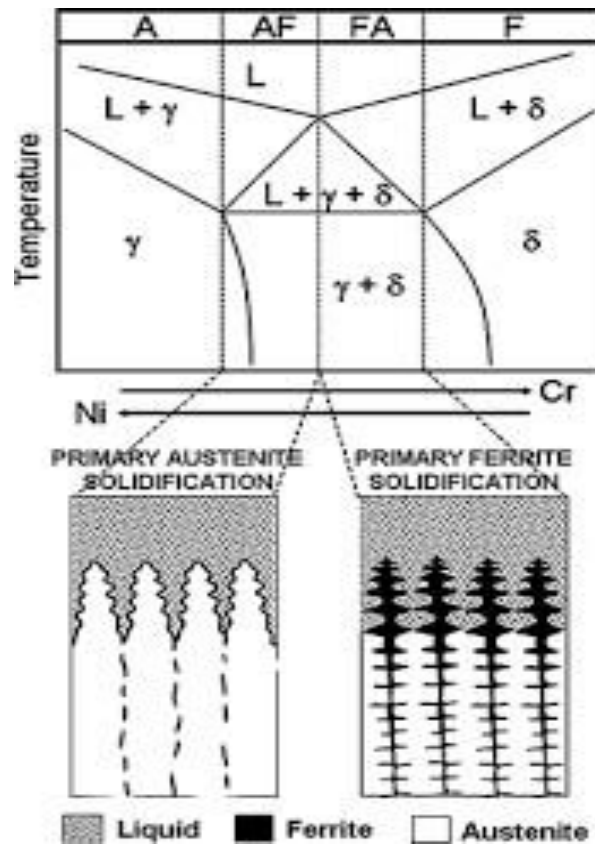
Fig 1.13. Solidification Modes of Fe-Cr-Ni ternary diagram[87]

Fig 1.13 shows that δ-ferrite exhibits different characteristics in FA mode welds compared to AF mode welds, varying in both morphology and chemical composition. In FA mode welds, the ferrite is primarily proeutectic with some eutectic ferrite, whereas in AF mode welds, ferrite forms exclusively below the eutectic. Despite these expected differences, the influence of solidification mode on thermal aging behavior remains largely unknown.

1.5.2 316L Stainless Steel for Additive Manufacturing

316L stainless steel is an industrial metal of choice due to its superior strength, corrosion resistance, ductility, and biocompatibility, making it suitable for various aerospace, marine, structural, and biomedical applications. It is one of the most prominent additive manufacturing (AM) alloys.[86] The widespread use of 316L stainless steel in the AM community is largely due to its benefits in cutting costs and minimizing material waste. The AM process can, however, introduce notable elemental segregation in the solidified material, which may result in unexpected variations in phase content, as shown in the pseudo-binary Fe-Cr-Ni phase diagram. The expected proportion of ferrite and the microstructure of austenitic stainless-steel parts created via the Directed Energy Deposition (DED) process may not match theoretical predictions, as indicated by modern weld composition diagrams used for pulse arc welding. This is because the cooling rates are comparable to power beam welding.[88] Phase changes and precipitate formation can result from heat accumulation during component fabrication. The production of 316L stainless steel components involves several steps, including machining, assembly, pre-welding, hot isostatic pressing, post-machining, and heat treatments. This multi-step approach makes it a "strong candidate" for additive manufacturing (AM), particularly in the assembly phase.

2. Literature Review

2.1 CMT-WAAM

CMT-WAAM is employed to fabricate components from 316 stainless steel, demonstrating notable impacts on bead dimensions and microstructural evolution, making it suitable for industrial applications. The CMT+P mode within this process is particularly effective at reducing grain size, especially in the deposited material's mid-section, enhancing the quality of the fabricated parts. Key parameters, including deposition current (ranging from 100 A to 175 A) and arc travel speed, influence bead dimensions and the resulting microstructure. By investigating these factors, the CMT-WAAM process reveals its potential for producing refined and well-structured stainless-steel components, optimizing performance for various industrial uses.[89]

Feng et al. examine the effects of process parameters on the bead geometry in WAAM using CMT technology. The research highlights the importance of these parameters in enhancing the quality of deposited metal parts and suggests promising avenues for future studies on deposition strategies. The results underscore the impact of process parameters on bead geometry, which could significantly influence wall deposition practices and overall bead quality.[90]

Trad et al. developed a geometrical model and set of mechanical parameters for CMT-WAAM stainless steel are introduced in this study, aiming to advance design and efficiency in wire arc additive manufacturing. The model enhances process accuracy and productivity, while the optimized mechanical parameters contribute to better quality in stainless steel components. The study also explores the calibration of mechanical properties and design values for improved CMT-WAAM performance.[91]

Huag et al. studied the highlights the effectiveness of CMT-based wire arc additive manufacturing for Inconel 625 alloy, achieving solid weld formation and a relatively consistent microstructure. Despite minor strength variations of up to 5% from bottom to top, the process provides reliable weld quality and uniform microstructural properties, with only slight variations due to the welding process itself.[92]

2.2 316L for Wire Arc Additive Manufacturing

Andrea et al. explore the AM of AISI 316L stainless steel, focusing on the techniques, challenges, and applications associated with this material. Emphasizing its customizable nature, corrosion resistance, and high strength, the paper also addresses printing parameters, common defects, mechanical properties, and the obstacles faced in utilizing AISI 316L in AM.[93]

Nabeel et al. review the properties of additively manufactured 316L stainless steel for orthopedic applications, focusing on its tunable microstructure, mechanical strength, corrosion resistance, and biocompatibility. It compares the properties of selective laser melting (SLM) 316L stainless steel with those of wrought 316L, highlighting the challenges and implications of additive manufacturing processes for orthopedic use.[94]

Kumar et al. studied WAAM for functional metals like 316L stainless steel, highlighting its process parameters and challenges in component optimization. WAAM is shown to provide mechanical properties similar to cast materials, along with cost efficiency and higher deposition rates. However, additional research is needed to overcome current issues.[95]

Zhao et al. examine the mechanical properties of WAAM stainless steel, addressing uncertainties about its anisotropic characteristics and their relation to metallographic structure, printing paths, and heat treatment. Tensile tests conducted on coupons from four different printing paths showed that WAAM stainless steel achieved high YS & UTS but had lower ductility than conventional

stainless steel. Anisotropy was noted in some printing paths, with the 45° specimens exhibiting the best mechanical properties. The study also found that non-heat-treated WAAM material had superior yield and ultimate strengths but reduced ductility compared to heat-treated samples[96]

Karpagaraj et al. discuss the effectiveness of WAAM for creating Stainless Steel 316L components, highlighting its benefits in achieving complex geometries with high accuracy and reduced material waste. WAAM is presented as an ideal technique for fabricating SS316 parts with excellent durability and corrosion resistance.[97]

Wu et al. investigate the production of thin-walled 316L stainless steel parts using WAAM with speed cold welding, focusing on how bottom current, scanning speed and cooling time affect the deposition process. A gradual reduction in bottom current improves stability and molding efficiency, while increased scanning speed or reduced cooling time leads to instability and slightly lower performance. Despite anisotropic properties, the samples meet industry standards. The study identifies that the best stability and mechanical properties are achieved with a 10-second cooling time, 30 cm/min scanning speed, and a gradual reduction in current during deposition.[98]

Kocaman et al. evaluate the suitability of WAAM as a replacement for traditional casting in producing Stainless Steel 316 components. The comparative analysis shows that WAAM parts have finer microstructures and higher yield strength due to rapid cooling, while cast parts exhibit coarser grains and lower δ-ferrite content. Although cast parts achieved better wear resistance after heat treatment, WAAM components outperformed in corrosion resistance, particularly with a dwell time of 120 seconds. These results suggest that WAAM is a promising alternative to casting for manufacturing complex-shaped stainless-steel parts with optimized process parameters.[99]

Vora et al. investigate the fabrication of a multi-layered SS316L structure using the GMAW-WAAM process with optimized parameters. The analysis focused on the microstructure,

macrostructure, and mechanical properties of the WAAM-built structure, including tensile strength, impact resistance, and microhardness, at various zones (top, middle, and bottom). Findings reveal robust inter-layer bonding, a defect-free macrostructure, and uniform microhardness across zones. The tensile and impact properties of the WAAM structure are comparable to or exceed those of wrought SS316L, underscoring the process's effectiveness for industrial use.[100]

Souza et al. examined the effects of WAAM on the properties of 316L stainless steel. The WAAM process resulted in a microstructure with ferrite in an austenitic matrix and variations in grain size between different regions. This caused an irregular microhardness profile, with a higher average (276 HV) than in the annealed condition. Mechanically, WAAM reduced the yield strength by 23% and elongation by 78%, while increasing UTS by 9%, still meeting industry standards. Electrochemically, WAAM 316L demonstrated similar corrosion resistance to conventional samples, with enhanced passivation potential.[101]

Pragana et al. examined the formability of WAAM AISI 316L stainless steel sheets and their compatibility with hybrid additive manufacturing involving sheet metal forming. Compared to wrought AISI 316L, WAAM sheets display stronger anisotropy and lower formability due to their dendritic structure. However, the sheets still demonstrate the ability to handle large plastic deformations, making them viable for integration into hybrid manufacturing processes.[102]

2.3 Optimization of Process Parameters

Doan et al. predict and optimize process parameters for the WAAM of 316L stainless steel, a widely used material in metallic AM. Using the Taguchi method and L16 orthogonal array, the researchers analyzed the effects of voltage, welding current, and travel speed on four key weld bead characteristics: width, height, penetration, and dilution. Analysis of variance (ANOVA)

revealed that travel speed most significantly affects bead width and height, while voltage primarily influences penetration and dilution. The optimal parameters—22 V, 110 A, and 0.3 m/min—were identified using GRA and TOPSIS methods, and their accuracy was confirmed through validation experiments.[103]

Chaudhari et al. focus on optimizing GMAW-WAAM variables—TS, WF, and V—to achieve desired bead geometries on an SS316L substrate. Multivariable regression equations were developed using the Box–Behnken design (BBD) technique, and ANOVA confirmed their feasibility. WFS was found to be the most significant factor influencing bead width (BW) and bead height (BH). Heat Transfer Search (HTS) optimization identified optimal parameters, resulting in a multi-layer structure with seamless fusion and no disbonding, making the findings valuable for industrial applications.[104]

Meena et al. focus on optimizing the CMT-WAAM process for fabricating super Duplex 2507 stainless steel by analyzing current, welding speed, and gas flow rate effects on bead geometry and material properties. The optimal parameters identified were 190.46 A current, 8.94 mm/s welding speed, and 15 l/min gas flow rate. The study found that current was the most critical factor influencing bead width, height, and dilution. Microstructural analysis showed ferrite and austenite phases in the weld bead, and the fabricated samples displayed good microhardness, making this process viable for stainless steel additive manufacturing[105]

Meena et al. optimized welding parameters for the WAAM process, focusing on Inconel 718. Using RSM and a central composite design, the researchers established a single-bead geometry model and determined optimal settings: 210 A current, 6.91 mm/s speed, and 25 l/min gas flow rate. Microstructural analysis revealed varying grain structures across layers, from small dendritic

grains at the top to columnar grains at the bottom. These findings are crucial for enhancing the quality of Inconel 718 parts in industrial WAAM applications.[106]

Mamedipaka et al. developed machine learning models, including regression-based and neural network approaches, to predict the mechanical properties of WAAM steel based on input parameters like current and wire feed speed. The study used 137 experimental datasets, and the results showed that the random forest model provided more accurate predictions than the neural network. Microstructural analysis of the 316L thin wall indicated that the presence of ferrite, austenite, and σ-phase inclusions affected hardness and mechanical properties, with average hardness, YS, and UTS measured at 185 Hv0.2, 303 ± 6 MPa, and 490 ± 18 MPa, respectively.[107]

Prasanna et al. investigated the fabrication of a 308L stainless steel cylinder using WAAM and CMT, with process optimization achieved through response surface methodology. The microstructure is characterized by vertical austenite dendrites and residual ferrite, with a hardness of 220 HV0.5. Mechanical properties include a yield strength of 368.5 MPa, ultimate tensile strength of 593 MPa, and elongation of 50.5%. The tensile strength shows minimal anisotropy (less than 10%), and the cylinder's performance is equal to or exceeds that of traditional 308L stainless steel, indicating its potential for industrial use.[108]

Koli et al. investigated how varying currents, welding speeds, and gas flow rates affect the mechanical properties of SS308L stainless steel in WAAM-CMT. By applying Taguchi's L9 orthogonal array, the study assessed changes in ultimate tensile strength, microhardness, compressive residual stress, and total elongation. The optimal process parameters were identified as 140A current, 8 mm/s welding speed, and 16 l/min gas flow rate, using fuzzy AHP and MARCOS for parameter optimization. The results indicated that current has the greatest impact

on the properties, and the samples met industrial stainless-steel standards based on XRD and EDX analysis.[109]

Lima et al. investigated how different process parameters affect the quality of 316LSi stainless steel preforms made via WAAM with CCC metal transfer. Using a 22 + 3 DoE approach, seven preforms were analyzed for geometric characteristics, hardness, and microstructure. The optimal settings were a torch travel speed of 300 mm/min and a wire feed speed of 4 m/min, which provided a superior surface finish, regular hardness profile, and a fine-grain microstructure while minimizing internal defects.[110]

Figueiredo et al. investigated how arc frequency, traverse speed, and wire feed speed affect the ferrite number and geometry of 316LSi stainless steel built using wire + arc additive manufacturing with pulsed gas metal arc welding. The experimental design revealed that increasing arc frequency reduces ferrite number and the height/width ratio, whereas higher wire feed and traverse speeds enhance these properties. The research also highlights the need for comprehensive geometric integrity assessments, including stability and spatter analysis. Optimized conditions were achieved, successfully fabricating a 74-layer, 4.12 kg structure, demonstrating the feasibility of large-sized 316LSi components.[111]

Kumar et al. optimized parameters for single-layer weld bead deposition in WAAM using GMAW and characterized the resulting structures. Findings indicate that grain structures differ due to thermal cycles, with ferrite and pearlite near the base, coarser grains along the deposition, and finer grains with ferrite and bainite near the final layer. XRD analysis identifies various chemical compounds across different layers. Surface defects such as cracks and porosity are prominent at layer interfaces, and micro-hardness values vary, with the flat wall measuring 162.806 HV and the circular wall 172.191 HV.[112]

Gu et al. investigated AISI 316L stainless steel parts fabricated by laser metal deposition additive manufacturing. Microstructural analysis reveals a bulk structure of columnar and equiaxed crystals, forming a remelted zone over earlier deposition layers. Tensile tests show similar strength in both parallel and perpendicular orientations to the laser scanning direction, but better elongation perpendicular to the scanning direction due to differences in crystal distribution. Residual stress measurements indicate tensile stress up to 315 MPa at the top surface and compressive stress at the part/substrate interface.[113]

2.4 Microstructural Properties

Gowthaman et al. investigate 316L stainless steel parts manufactured via the CMT-based WAAM process, examining the microstructure and mechanical properties. The microstructure features columnar and equiaxed grains with epitaxial growth, though radiographic tests reveal defects like pores and cracks. Microhardness is uniformly distributed, with an average of 220 HV. Tensile tests indicate anisotropy, with horizontal samples showing higher strength than vertical ones. The fracture analysis reveals a ductile nature with sufficient plastic deformation. Overall, the WAAM-fabricated parts outperform traditional 316L stainless steel casting, forging, and wrought methods regarding microstructure and mechanical properties.[114]

Chen et al. employed the CMT process to fabricate 316L stainless steel, resulting in a microstructure characterized by austenitic coarse columnar grains and scattered ferrite. As-built CMT 316L and annealed wrought 316L were subjected to dynamic compression tests using a Split-Hopkinson Pressure Bar. The CMT 316L demonstrated nearly isotropic behavior under dynamic loading. It exhibited higher dynamic yield strength and flow stress at low strains than the wrought material but lower values at higher strains due to twinning-induced plasticity. Microstructural analysis revealed that twin thickness in CMT 316L peaks at strain rates of 1000–1500 s^{-1}.[115]

Yang et al. focused on the microstructure and corrosion resistance of 316L stainless steel fabricated using GTAW-AM with different arc currents. Higher arc currents (140 to 180 A) led to coarser austenite grains, reduced ferrite content, and the formation of α phases. These microstructural transformations, especially the emergence of α phases due to chromium depletion, resulted in a marked reduction in the corrosion resistance of the additive-manufactured stainless steel.[116]

Belotti et al. focus on the microstructure of thick 316LSi stainless steel parts made by WAAM. It reveals large, oriented columnar grains with predominant <100> texture and austenite matrix, mixed with ferrite and oxide inclusions. The texture variation is attributed to thermal gradients and processing conditions during manufacturing. The study highlights the detailed structural characteristics of multi-walled WAAM parts, including the complex interplay of grain orientation and local thermal effects.[117]

Zhong et al. assessed the feasibility of depositing SS316L nuclear nozzles onto PWR pipelines using WAAM and CMT, providing comprehensive microstructural and mechanical data. Hierarchical molten pool structures and low defect levels characterize the microstructure. The mechanical properties surpass ASTM A370 standards due to the beneficial effects of ferrite dispersion and dislocation density. The study suggests that future work should address surface oxidation, internal pores, and δ-ferrite content to improve corrosion resistance and mitigate atomic segregation issues.[118]

Xu et al. studied the effects of in-situ rolling and heat treatment on WAAM 316L stainless steel to assess changes in microstructure, mechanical properties, and corrosion behavior. In-situ rolling led to significant microstructural changes, including a shift from dendritic to reticulated ferrite and the formation of low-angle grain boundaries. Heat treatment at 650 °C increased tensile strength but decreased yield strength and elongation. Above 1000 °C, rolled WAAM 316L exhibited better

strength and ductility than unrolled samples. Corrosion resistance initially decreased with increasing heat treatment temperature but improved afterward, with in-situ rolling decreasing corrosion current density while affecting the stability of the passive film.[119]

Rodrigues explored the impact of heat treatments on the microstructure of 316L stainless steel walls produced via WAAM. δ-ferrite dendrites were observed in as-built samples, and σ-phase precipitation was noted during early isothermal holding at 950 °C. Heat treatments at 1050 and 1200 °C significantly reduced δ-ferrite levels to about 6.5% and 0.4%, respectively, with a direct relationship between δ-ferrite content and hardness values. The study utilized synchrotron X-ray diffraction and thermodynamic calculations to analyze the microstructural evolution of WAAM-fabricated 316L stainless steel under various heat treatments.[120]

Le et al. focus on WAAM of 308L stainless steel, optimizing the welding parameters to achieve ideal weld bead geometry for thin-walled structures. The resulting microstructure consists of vertically oriented austenite dendrites with ferrites at the grain boundaries. Mechanical testing reveals a microhardness of 163 HV0.1, UTS of 532-553 MPa, YS of 344-353 MPa, and elongation between 40-54%, which aligns closely with the properties of traditionally wrought 308L stainless steel, indicating the material's suitability for industrial use.[121]

Wang et al. investigated the effects of heat treatment temperature on the microstructure and tensile properties of WAAM-fabricated 316L stainless steel. Heat treatments below 1000 °C did not significantly affect the multilayered structure but altered ferrite and σ phase characteristics. As the temperature increased, the transformation of ferrite to σ phase led to reduced strength and improved elongation. After solution annealing above 1000 °C, the ferrite and σ phase nearly dissolved, the multilayered structure was destroyed, and austenite recrystallized, resulting in significantly improved elongation and reduced anisotropy.[122]

Wang et al. explored how varying heat input affects the performance of 316L stainless steel components produced by WAAM, specifically focusing on a partition plate structure used in heat exchangers. Using Q235 steel as the base, it was found that higher heat inputs (up to 3.59 kJ/cm) coarsened the grain structure, reduced hardness, and negatively impacted tensile strength and corrosion resistance. The best mechanical properties were achieved at the lowest heat input (2.41 kJ/cm), while the highest input resulted in the poorest corrosion resistance, with a self-corrosion current of 3.853×10^{-5} A·cm^{-2}.[123]

Rao et al. investigated how welding current and travel speed influence bead geometry and microstructure in WAAM-deposited 308L stainless steel. Higher currents expand bead width, while increased travel speeds reduce bead height and enhance the ferrite phase content. Optimal deposition was achieved at 120 A and 25 mm/min, yielding uniform layers ideal for WAAM applications. These findings are particularly relevant for optimizing the production of customized orthopedic knee implants, enhancing their quality and performance.[124]

Long et al. examined how linear energy input (LEI) and cooling rate (CR) affect steel's microstructure and mechanical properties in CMT-WAAM. δ-ferrite and austenite dendrites dominate the microstructure, with σ phase forming under low CR. Lower LEI or higher CR results in finer dendrite spacing, increased tensile strength, and reduced elongation. Fracture mechanisms differ: low LEI leads to pore coalescence, while high LEI causes cracks due to dislocation accumulation around δ-ferrite.[125]

2.5 Residual Stress in WAAM

Li et al. examined the formation and impact of residual stress in metal AM, particularly focusing on the challenges posed by the unique thermal cycles in processes like PBF and DED. The research highlights that residual stress is primarily caused by high-temperature gradients and rapid cooling,

leading to part distortion and reduced functionality. Various mitigation methods are discussed, including preheating, process planning, and heat treatment. The study emphasizes that residual stress research in AM is still developing, with future work needed in measurement techniques, stress mitigation, and its effects on part performance.[126]

Goviazin et al. explored the use of WAAM-fabricated 316L stainless steel cylinders in a flow-forming operation to produce high-strength, thin-walled components. Although the material tolerated significant plastic deformation without pre-treatment, the process introduced considerable residual stresses. Heat treatments ranging from 400 to 800 °C were investigated to reduce these stresses. Results showed that heat treatment up to 600 °C enhanced strength by around 20% while decreasing residual stress, whereas full stress relief and strength reduction occurred at 800.[127]

Theodore et al. focused on mitigating residual stresses and strains in thick stainless-steel parts produced by the Double-WAAM process. By combining two different filler metals, austenitic 304L and ferritic 430, the research aims to reduce these undesirable effects. The optimal mix of 50% 304L and 50% 430 fillers on a 304L baseplate resulted in a significant reduction in strain (67%) and stress (40%) compared to using only 304L filler. Analysis methods, including neutron diffraction and profilometry, confirmed the effectiveness of this approach, with close agreement between the measured stress results.[128]

Gordon et al. examined the fatigue and fracture behavior of wire and arc additively manufactured 304L stainless steel, focusing on the microstructure-property relationships. Mechanical tests were performed on specimens oriented horizontally and vertically within the build to assess crack growth resistance. The findings indicate that vertical orientations provide the highest resistance to crack growth, following Paris Law behavior, comparable to wrought steel alloys. Scanning

electron microscopy and electron backscatter detection were employed to analyze microstructural effects on crack propagation, providing insights into how the material's microstructure influences its mechanical performance.[129]

Guo et al. investigated Residual stress distribution in 316L stainless steel produced via the DED process was measured using a fine synchrotron X-ray beam. The study found that at the macroscopic scale, stress was highest near the travel map region, with cooling rate changes identified as a key factor. At the mesoscopic scale, stress variations were linked to local changes in thermal gradient during solidification, corresponding with fluctuations in microstructural features. These findings highlight the influence of solidification conditions on residual stress patterns in DED-manufactured components.[130]

Wildenhain et al. investigate the effects of heat input and cooling conditions on RS and cold-cracking susceptibility in WAAM of high-strength steels. The study found that increased heat input prolongs cooling time and reduces surface residual stresses by about 200 MPa, potentially lowering the risk of cold-cracking. These results offer critical guidance for optimizing WAAM processes and establishing standardized practices to safely and efficiently manufacture high-strength steel components.[131]

Feng et al. addressed the critical issue of residual stress in metal AM caused by high-temperature gradients and rapid cooling during processes like PBF and DED. High tensile residual stress is common, especially near the surface of AM parts, which can lead to distortion and compromised functionality. The study discusses in-process and post-process methods to mitigate these stresses. It calls for further research into residual stress measurement, mitigation strategies, and their impact on part performance, such as fatigue and corrosion resistance.[132]

2.6 Motivation of The Present Work

Many industries are exploring AM as a preferred approach for design and manufacturing, recognizing its benefits in cutting material waste, lowering costs, reducing lead times, accommodating complex geometries, achieving near-net shapes, and improving overall production efficiency. In the CMT-WAAM process, controlling heat input by adjusting various process parameters enhances microstructure characteristics, mechanical properties, corrosion and wear resistance, and residual stress management. However, these improvements often come at the cost of geometrical accuracy and tolerance consistency. WAAM can build 3D parts layer by layer, which could transform various industries. Its advantages include higher deposition rates, the ability to produce large components quickly and at a lower cost, effective part repair, and an environmentally friendly process.[88] 316L stainless steel is widely used in aerospace, automotive, chemical processing, defense, nuclear, and bio-medical industries for manufacturing, repairing, and replacing components. Hence, exploring the use of 316L stainless steel in the WAAM process under different heat input scenarios is necessary, given that this approach is considerably more efficient, economical, and sustainable than forging and casting. Presently, WAAM research has concentrated on straightforward structures. Investigating complex parts and methods that offer better deposition and design flexibility is crucial to fulfill industry needs. Variations in final quality can occur due to different heat input levels and parameter conditions. However, there is a shortage of research on 316L stainless steel walls deposited with varying heat inputs. This study aims to improve the performance of 316L stainless steel walls by optimizing various process parameters, including I, WS, and CTWD, to achieve a fine, dense structure with enhanced mechanical properties. The study investigates the microstructure, mechanical properties, and residual stresses of 316L stainless steel walls fabricated using the CMT-WAAM process. It performs optimization

to identify the best input parameter combinations for superior mechanical and microstructural outcomes.

2.7 Research Gap

The GMAW process effectively fabricates large and medium-sized components, including 316L stainless steel parts. However, traditional GMAW faces challenges like spattering, arc instability, and imprecise weld bead placement. The CMT process, an advanced variant of GMAW, offers spatter-free welds with low heat input, high deposition rates, and improved quality, making it ideal for AM applications. WAAM, which uses metal wire and an electric arc, benefits from the CMT process, making it more cost-effective, safer, and efficient.

Despite significant progress in optimizing parameters to enhance the mechanical and metallurgical properties of WAAM, notable research gaps remain. A considerable body of work has focused on refining parameters to improve the overall performance of WAAM components. However, specific optimization of critical parameters such as I, WS, and CTWD is still lacking. These parameters play a crucial role in determining the quality and reliability of the final product, influencing factors like heat input, cooling rates, and material deposition characteristics. Achieving consistent and superior mechanical and metallurgical properties without precise optimization remains challenging. Addressing this gap is essential for advancing the WAAM process and realizing its potential in industrial applications.

2.8 Objectives of Present Work

The sole aim of the present work is to develop and characterize 3D metallic WAAM samples and comparison with wrought metal. This objective will be achieved by following the following steps.

1. To develop the 3D metallic WAAM samples using Cold Metal Transfer technique.

2. To study the Metallography of metallic 3d WAAM samples such as Optical Microscope (OM), Scanning Electron Microscope (SEM) and X Ray Diffraction.

3. To investigate and analyze the mechanical properties of WAAM samples such as micro-hardness, tensile behavior and residual stresses compared to equivalent parent material.

4. To analyze the thermal properties of WAAM sample compared to the parent material.

5. To determine the optimal parameters for 3D metallic WAAM samples.

3. Research Methodology

This section describes the experimental details for implementing and executing the experiments at several phases. This chapter comprises the fabrication of WAAM samples using the Robotic CMT technique. Several characterization techniques are employed to study WAAM's microstructure and microstructural properties.

3.1 Substrate Material

In the current work, SS316L substrate is used. The steel substrate's selected dimension is 200 x60x6 mm3. Before the fabrication of the SS316L WAAM samples welding process commenced, a thorough cleaning procedure was administered to an SS316L substrate. This involved using a steel wire brush and acetone to remove surface oxides and impurities effectively. The base was securely affixed to the welding table using C-type clamps.

3.2 Selection of Filler Wire

A 1.2 mm diameter SS316L filler wire was utilized in fabricating WAAM samples. The superior corrosion resistance and mechanical strength of SS316L are primarily attributed to its composition, which includes elements like Mo, Ni, and Cr. With a welding temperature range between 1300°C and 1400°C, SS316L is ideal for ensuring effective fusion between layers in additive manufacturing due to its excellent weldability. The SS316L wires, with their higher deposition rate, are ideal for GMAW, allowing the creation of high-strength components with outstanding mechanical properties. SS316L is a low-carbon austenitic stainless steel, containing just 0.03% carbon by weight. Its exceptional corrosion resistance, excellent weldability, high strength, ductility, robust biocompatibility, and affordability make it a preferred material for various industrial sectors, such as maritime and offshore structures, biomedical devices, automotive parts,

petrochemical plants, and nuclear reactors. The chemical composition of SS316L, analyzed via chemical spectroscopy according to ASTM E415, is provided in Table 3.1, while Tables 3.2 andm3.3 detail its physical and mechanical properties.

Table 3.1 Chemical composition of SS316L

				Element (Weight %)						
Material	Cr	Ni	Mo	C	Mn	S	Si	P	Cu	Fe
SS316L	18.56	11.55	2.53	0.01	1.53	0.01	0.59	0.027	0.17	Rest

Table 3.2 Physical Properties of SS316L

Property	Value
Density	8.00 g/cm^3
Electrical Resistivity	$0.74 \times 10^{-6} \ \Omega.\text{m}$
Modulus of Elasticity	193 GPa
Melting Point	$1400°\text{C}$
Thermal Conductivity	16.3 W/m.K
Thermal Expansion	$15.9 \times 10^{-6}/\text{K}$

Table 3.3 Mechanical Properties of SS316L

Property	Value
UTS (MPa)	485
YS (MPa)	170
PE	40
Hardness (HV)	Brinell-217 HV Rockwell- 95 HV

3.3 Experimental Setup

The research work employs a KuKa robot (Model: KR 8 R1440, Germany) and a CMT source from Fronius (Model: TPS 400i, Austria). A schematic diagram of the CMT-WAAM setup is presented in Fig. 3.1. To optimize the process, preliminary trials were conducted to identify the

most effective process parameters. The CMT welding process has an intrinsic relationship between current, voltage, and wire feed rate. Adjusting one of these parameters automatically influences the settings of the other two. For instance, increasing the wire feed rate typically requires a corresponding adjustment in current and voltage to maintain a stable arc and ensure proper fusion. This interdependence underscores the importance of carefully selecting the initial settings to achieve the desired welding outcomes and maintain consistency in the additive manufacturing process. As a result, the current settings were established through a series of trial runs and an extensive literature review. It is important to note that welding speed is a critical factor influencing the quality of WAAM, as it significantly affects the mechanical properties of the fabricated components. Additionally, the contact tip to work distance (CTWD) is a key parameter that greatly impacts bead geometry and deposition conditions. This, in turn, has a substantial effect on both the surface finish of the weld and the stability of the welding arc. Considering their influence on the mechanical characteristics witnessed during trial runs, current, welding speed, and CTWD were selected within the array of diverse welding parameters. The shielding gas and its corresponding flow rate were selected after thoroughly reviewing the available literature, acknowledging their significant influence on microstructural properties. Consequently, a consistent supply of a gas mixture comprising 97% Ar and 3% CO_2 with 99.99% purity was maintained at a flow rate of 15 liters per minute. The current studies focus on optimizing input parameters to address multiple response variables simultaneously. Recognizing the need for more comprehensive research. In light of this, the study initiated additive experiments to explore the effects of input parameters, namely current, welding speed, and CTWD, and effects on the microstructural and mechanical properties of WAAM samples. Furthermore, the study includes material characterization and microstructural analysis for the sample produced using optimal input

parameter combination. The study examined three mechanical properties: UTS, MH, and RS in CMT-WAAM samples. Fig 3.2 shows the experimental setup of the CMT-WAAM.
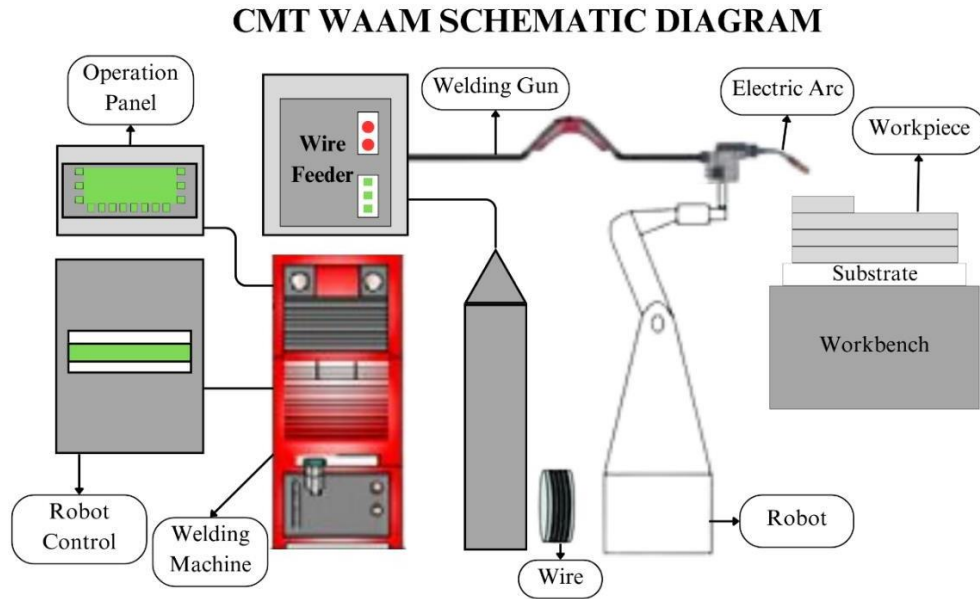
Fig 3.1 Schematic Diagram of CMT-WAAM Setup
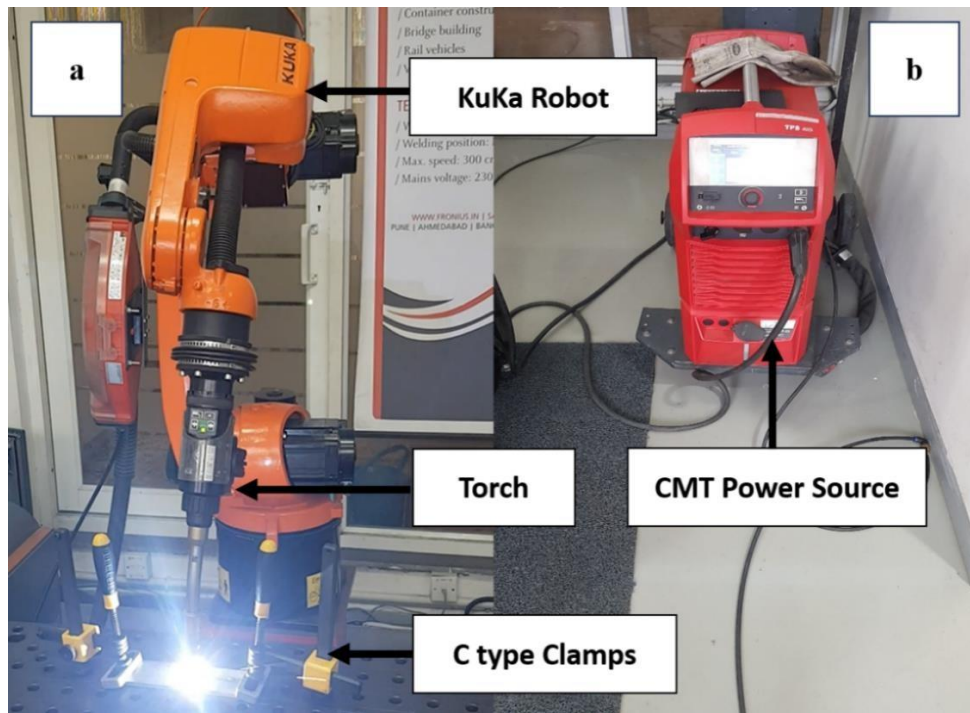
Fig 3.2 Robotic CMT WAAM setup (a) KuKa Robot (KR 8 R1440) (b) CMT Welding Source (TPS 400i)

3.3.1 KuKa Robot (Model: KR 8 R1440)

Designed for enhanced dynamic performance, the KR 8 R1440 robot has a standard payload capacity of 8 kg. Reducing the load center distances and optimizing supplementary loads.[133] Technical Specification is presented in Table 3.4

Table 3.4 Technical Specification of KuKa KR 8 R1440

Maximum reach	1441 mm
Pose repeatability (ISO 9283)	± 0.04 mm
Maximum payload	14.5 kg
Footprint	333.5 mm x 307 mm
Rated payload	8 kg
Weight	167 kg
Mounting position	Floor; Ceiling; Wall; Desired angle
Number of axes	6

3.3.2 Robot Program for WAAM samples

```
1        DEF WAAM_SUDEEP

2

3        decl int layer

4        INI

5        base_data[5]=base_data[1]

6        Layer=0

7        SPTP HOME Vel = 20% DEFAULT
```

8	SPTP P01 CONT Vel = 20% PDAT1 Tool [2] : Tool2 Base [1] : table
9	SPTP P01 CONT Vel = 20% PDAT2 Tool [2] : Tool2 Base [1] : table
10	ARCON WDAT1 LIN P03 Vel = 2 m/s CPDAT 01 Tool [2] : Tool2 Base[1] : table
11	ARCSWI WDAT1 LIN P12 CPDAT 09 Tool [2] : Tool2 Base [5] :base5
12	ARCSWI WDAT1 LIN P13 CPDAT 10 Tool [2] : Tool2 Base [5] :base5
13	For layer = 0 to 40
14	ARCSWI WDAT2 LIN P04 CPDAT 02 Tool [2] : Tool2 Base [5] :base5
15	ARCSWI WDAT2 LIN P05 CPDAT 03 Tool [2] : Tool2 Base [5] :base5
16	ARCSWI WDAT2 LIN P06 CPDAT 04 Tool [2] : Tool2 Base [5] :base5
17	base_data[5]. Z=base_data[5].z + 3.0
18	Endfor
19	ARCOFF WDAT2 LIN P15 CPDAT12 Tool [2] : Tool2 Base[5] : base5
20	SPTP P09 CONT Vel = 20% PDAT3 Tool [2] : Tool2 Base[1] : table
21	SPTP HOME Vel = 20% DEFAULT
22	→END

3.3.3 Welding Source (CMT Fronius-Model: TPS 400i)

Technical specification of Fronius TPS 400i is presented in Table 3.5

Table 3.5 Technical Specification of Fronius TPS 400i

Mains voltage	3 x 400V
Open-circuit voltage	73 V
Mains frequency	50-60Hz
Welding current max/min	400 A /3 A
Duty cycle [10min/40°C]	40%

Dimensions	LxWxH (in mm)
	706 x 300 x 510
Weight	36,45 kg

3.4 Characterization Equipment

Two types of characterization were performed: Mechanical Tests and Microstructural analysis. Mechanical Tests were conducted to evaluate the material's strength, hardness, and durability. Microstructural Characterization: Microstructural Analysis involves examining the material's microstructure using optical microscopy and SEM techniques. These methods provide detailed images of the material's internal structure, revealing grain size, phase distribution, and potential defects or inclusions. XRD Analysis: XRD analysis determines the material's crystalline structure, phase composition, and orientation. This technique can identify and quantify the various phases by measuring the diffraction patterns of X-rays passing through the sample, providing crucial information about the material's composition and structural properties.

3.4.1 Optical Microscopy

The Olympus GX41, as shown in Fig 3.3 and detailed in Table 3.6, is a compact, portable inverted metallurgical microscope. It provides fast, accurate specimen characterization with outstanding image quality, high resolution, and ergonomic features, making it suitable for brightfield and polarized illumination. Initially, the epoxy-mounted samples underwent a stepwise polishing regimen, progressing through emery papers with grit sizes ranging from 400 - 2500. Following this, Before being observed under the microscope, the polished samples were etched for 45 seconds in Keller's reagent, a solution made up of 2.5% HNO3, 1% HF, 1.5% HCl, and distilled water.
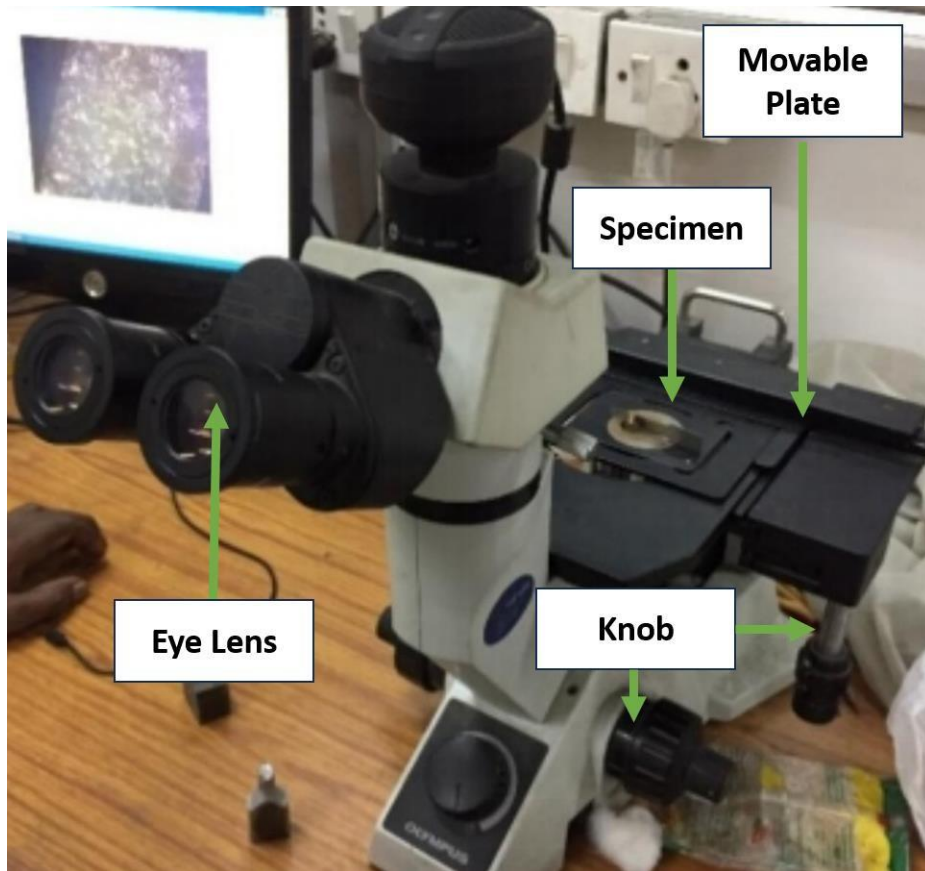
Fig 3.3 Optical Microscope (Olympus GX41)

Table 3.6 Specification of Olympus GX41 Optical Microscope

Optical system	UIS2
Light Source	6V30: long-life halogen lamp 6V30: High-intensity halogen lamp
Revolving nose piece	Quadruple revolving nose piece
Plane stage	Size: 160 (W) x 250 (D) mm
Stroke	120 mm (X) x 78 (Y) mm
Observation Method	Reflected light brightfield observation, reflected light simple polarizing observation

Coaxial handle	attachable to right/left side of the plane stage
Rated power	6 V~30 VA
Rated voltage, current & frequency	100-120 V/220-240 V~0.85/0.45 A, 50/60 Hz
Power consumption	85 VA 40 W
Dimensions	236 x 624 x 407mm
Weight	10Kg

3.4.2 Field Emission Scanning Electron Microscopy (FESEM)

FESEM, illustrated in Fig 3.4 and detailed in Table 3.7, uses a finely focused electron probe to achieve high-resolution imaging. The electron beam scans the entire specimen through a process called raster scanning, where accelerated electrons interact with the specimen, resulting in scattered signals that form the image. The FESEM specimens were first polished in sequence using SiC papers with grit sizes ranging from 400 to 2400, followed by polishing with a 2.5 µm diamond paste. To conclude, the specimens were etched using Keller's reagent, a solution composed of 2.5% nitric acid (HNO_3), 1% hydrofluoric acid (HF), 1.5% HCl, and distilled water.

Fig 3.4 ZEISS FESEM (Gemini 1 Sigma 300)

Table 3.7 Specification of Gemini Sigma 300 FESEM

Magnification	x10-1M
Probe current	3pA-20nA
Acceleration	Voltage 0.02-30kV
5-axes motorized eucentric specimen stage	(X,Y=130mm, Z=50mm, T=-3deg-70deg, R-360deg)
Detector	Inlens Secondary Electron Detector Everhart Thornley Secondary Electron Detector

3.4.3 Energy Dispersive X-ray Spectroscopy (EDS)

EDS, often called EDX or EDXS, is a typical method used in analytical electron microscopy. Characteristic X-rays are emitted during inner-shell electron transitions, with their energy specific to each element, allowing for element identification via EDS. Higher atomic numbers increase X-ray emission probability, making EDS especially useful for detecting heavy elements.[134] The Oxford Instruments EDS utilized in this work is depicted in Fig 3.5.
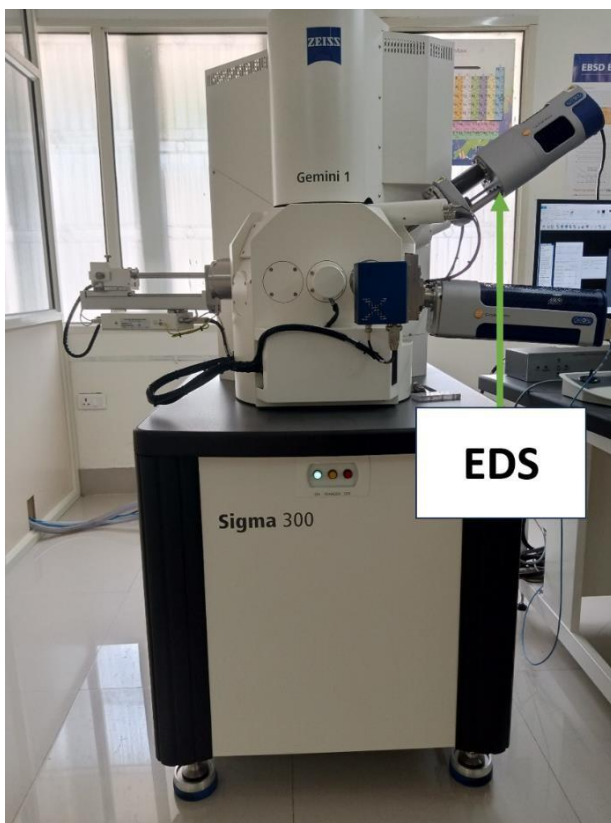
Fig 3.5 Oxford Instruments EDS

3.4.4 X-ray Diffraction (XRD)

Diffraction patterns arise when light scatters off a periodic array with long-range order, resulting in constructive interference at specific angles. This interference, visible only at certain angles, enables the analysis of crystal structure trends, further examined using the Miller indices of the

diffraction peaks. The X-rays used have wavelengths comparable to interatomic distances, causing diffraction patterns to form as the X-rays interact with the atoms. These patterns provide crucial information about the crystal's atomic arrangement. The XRD spectrum, shown in Fig. 3.6, was acquired using the X-ray diffractometer (Model: RIGAKU SMART LAB), with its technical specifications listed in Table 3.8.

Fig 3.6 XRD (Rigaku Hypix 400 SmartLab)

In XRD, the diffraction peaks are directly related to the atomic planes in the crystal, providing insights into the atomic and microstructural characteristics. The positions of these diffraction peaks are calculated using Bragg's law ($n\lambda = 2\ d_{hkl}\ \sin\theta$), Here, d_{hkl} represents the spacing between the parallel planes in the crystal, θ is the angle between the incident X-ray beam and the normal to the lattice plane, λ denotes the wavelength of the X-rays, and n indicates the order of reflection. Bragg's law is essential for determining the angles at which constructive interference, and thus diffraction peaks, occur due to X-ray scattering from the crystal planes. The intensity and positioning of these peaks depend on the crystal structure, indicating how atoms are periodically arranged across the crystal.

51

Table 3.8 Specification of XRD (Rigaku Hypix 400)

Pixel size	100 µm x 100 µm
Active area	9.6 mm x 38.5 mm
Pixels	96 x 385 = 36,960 pixels
Count rate per pixel	> 1 x 106 cps/pixel
Global count rate	>3.7 x 10 10 cps
Readout mode	Long (31-bit) mode, Diff mode, 0-dead time mode
Framing rate	131 fps (Diff mode), 87 fps (Long mode)
Energy range	4 to 30 keV
Counting efficiency	99% (at CuKa)
Energy resolution	<25% (at CuKa)
Operating Temperature	15-35° C
Weight	Approx. 900 g

3.4.5 Residual Stress Measurement

Residual stresses at different locations on the weldment were meticulously measured using the Pulstec µ-X360n Full 2D High-Resolution X-ray Diffraction (HR-XRD) machine, as shown in Fig. 3.7. This advanced HR-XRD system allows for precise, high-resolution measurements of residual stresses across the weldment, ensuring a detailed understanding of stress distribution within the material. The technical specifications of the Pulstec µ-X360n, which highlight its capabilities in capturing fine stress details, are outlined in Table 3.9, further emphasizing the machine's role in accurate and comprehensive stress analysis.

Fig 3.7 Pulstec μ-X360n X-ray Diffraction (XRD)

Equipped with a standard Cr X-ray tube functioning at 30 kV and 1 mA, and a 1 mm collimator, the device is designed for high-precision measurements. The Cosα method is employed to capture the complete Debye-Scherrer ring in one swift X-ray exposure using a 2D detector. This approach effectively reveals critical details such as grain orientation, texture, and grain coarsening, offering a thorough examination of the material's microstructural properties.[135] This technique is more efficient than the traditional $\sin^2\psi$ method, as it does not require tilting the sample at various angles. The X-ray penetrates up to 1 μm into the material, measuring the spacing of atomic planes and any changes induced by processing, with the data collected from the Debye ring in just one measurement. The irradiation of the samples was executed with precise parameters, encompassing a beam current (0.66 mA) and voltage (30 kV). The incident angle of the X-ray beam on each sample was deliberately set at 30°. Measurement parameters for the sample included crucial values

such as the diffraction angle (148.513 degrees), interplanar spacing (d = 1.083 Å), and X-ray wavelength (Cr) for both the K-alpha (2.29093 Å) and K-beta (2.08480 Å) lines.

Table 3.9 Specification of Residual Stress Measurement (Pulstec μ-X360n)

Measurement	Single Incident X-ray
Method	Cosα
Power	100-240 V, 130W
Collimator Size	φ 1 mm
Operability	60 – 100 secs
Weight	Sensor unit – 2.4 Kg Power Supply- 6.2 Kg

3.4.6 X-ray Computed Tomography

The WAAM samples were inspected for porosity using Nikon Metrology's XTH 225 ST and XTH 225/320 LC CT scan machines, as illustrated in Fig. 3.8. The technical specifications of the CT scanner are listed in Table 3.10. The X-ray scanning was conducted with a voltage of 220 kV and a current of 32 mA, exposing each sample for 1000 ms per projection. In total, 3300 projections were obtained, achieving a high scanning resolution of 7.3 µm (effective pixels). Nikon Metrology Inspect-X and XT CT Pro/CT agent software were employed to configure the scanner and reconstruct the CT volume. Subsequently, Volume Graphics GmbH (VG 2.2) software was used to analyze the reconstructed volume, allowing for detailed delamination assessment of the metal printed layers.

Fig 3.8 Nikon XTH 225 ST X-ray CT Scanner

Table 3.10 Specification of X-ray CT Scanner (Nikon XTH 225 ST)

X-ray Source	
Type	Open Tube Microfocus
Energy	225 KV (max)
Power	450 W (max)
Focal spot	1 µm (max)
Detector	
Max area	432 mm x 432 mm
Max Pixel	2880 x 2880
Min Pixel	150 µm
Max Frame Rate	30 fps

System	
Max CT Swept Diameter	265 mm
Max Focus Imager Distance	1110 mm nominal
Max Sample weight	50 Kg
Cabinet	
Dimensions (in mm)(L x W x H)	2414 x 1275 x 2202
Weight	4200 Kg

3.4.7 Thermal Imaging Camera

The FLIR E96 is a pioneering pistol-grip thermal camera featuring a high-resolution detector of 640×480 pixels, enabling inspectors to safely survey high-voltage and hazardous targets while efficiently diagnosing electrical and mechanical issues. Equipped with various lens options, the E96 provides comprehensive coverage for both close and distant inspections. With the FLIR FlexView™ dual field-of-view lens, users can effortlessly switch between wide-angle and telephoto views with just a push of a button. The FLIR E96 infrared camera, depicted in Fig. 3.9, was used for thermographic analysis during the steel sample fabrication in this study. The camera measures temperatures up to 1500 °C and provides a measurement accuracy of ±2%, thermal sensitivity of 50 mK, a refresh rate of 30 Hz, and a resolution of 640×480 pixels. The detailed specifications are presented in Table 3.11.
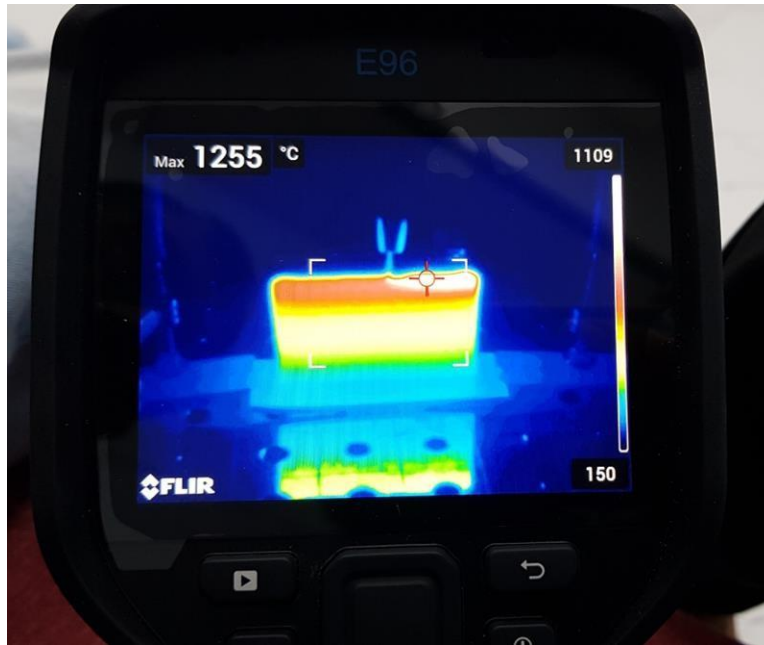
Fig 3.9 Flir E96 Thermal Imaging Camera

Table 3.11 Specification of Thermal Imaging Camera (Flir-E96)

IR Resolution	640×480 pixels
Thermal Sensitivity	<40 mK at 30°C
Accuracy	±2°C (±3.6°F) or ±2%
Display	4", 640×480-pixel touchscreen LCD
Digital Zoom	1-8
Image Frequency	30 Hz
Minimum Focus Distance	0.15 m
Digital Camera	5 MP
Digital Zoom	1-8
Spectral Range	7.5-14 µm

3.4.8 Tensile Test

Material selection in engineering is predominantly based on mechanical properties such as tensile strength and percentage elongation. Tensile testing plays a vital role in assessing these properties and providing essential documentation for the tensile characteristics of new materials. This documentation helps compare and stabilize new materials against existing options in the market. Various factors, such as tensile strength, influence a material, with some key attributes outlined below. Intermolecular forces, which are directly linked to molecular structure, play a significant role; even minor changes in molecular arrangement can impact tensile strength. Additionally, tensile strength generally increases with rising temperatures up to a certain point, after which it begins to decline. The composition of a material also affects its molecular structure and binding forces, thereby influencing its UTS. The tensile strength of a material can only be accurately measured through tensile testing. The tensile test samples, depicted in Fig. 3.10, have a dog bone shape. The research employed a Universal Testing Machine (Instron 4482), shown in Fig. 3.11, with its technical specifications detailed in Table 3.12. Samples were prepared following the ASTM-E8M standard, using wire EDM for accurate extraction. The tensile tests were performed at room temperature with a consistent cross-head speed of 1 mm/min.
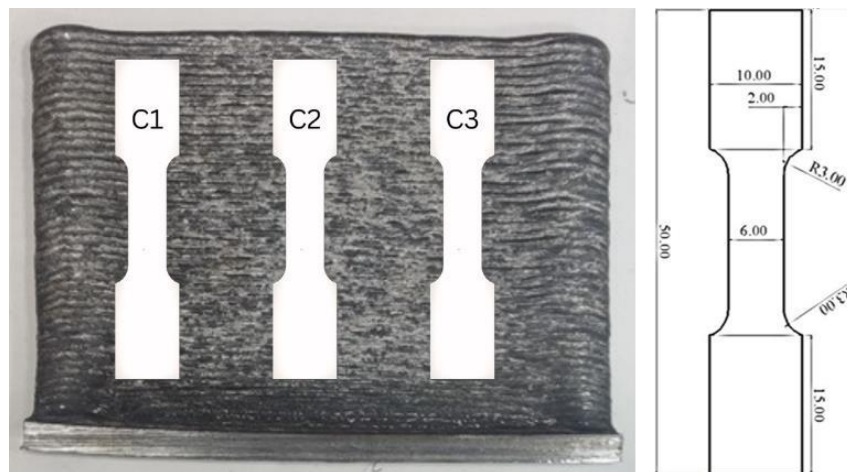
Fig 3.10 ASTM (E8M) DOG BONE Sample
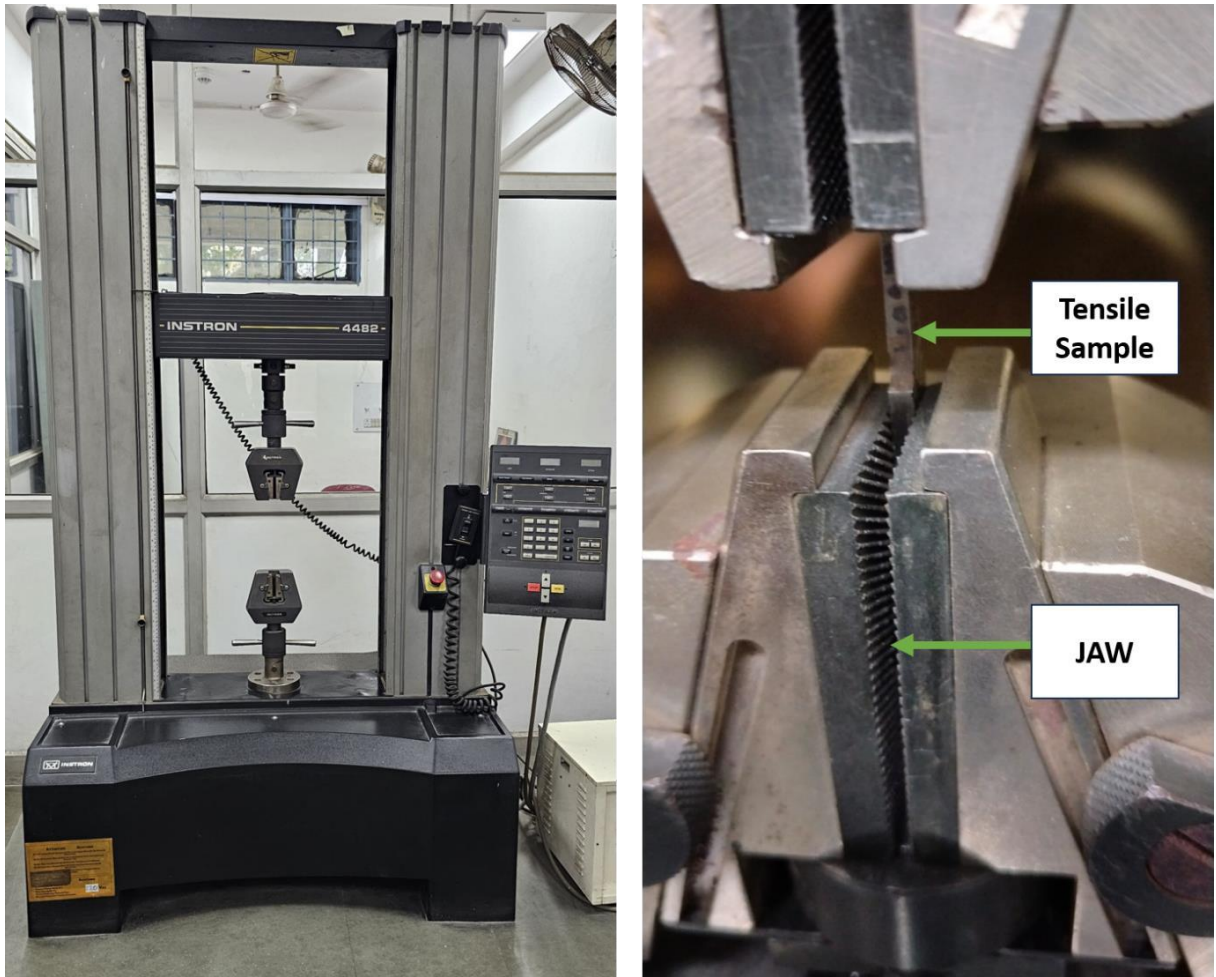
Fig 3.11 Instron Universal Testing Machine

Table 3.12 Specification of Universal Testing Machine (Instron-4482)

Capacity	100 KN
Load Weight Accuracy	±0.01% of full scale or ±0.5% of reading
Operating temperature (°C)	+10 to +38
Dimensions (HxWxD) H: Height, W: Width, D: Depth	Height: 406.4 mm Width: 280 mm Depth: 58.2 mm
Weight	2.7 kg approx
Strain measurement standards:	ASTM E83, ISO 9513, BS3846, EN1002-4

3.4.9 Microhardness Testing

Microhardness testing is employed to evaluate the hardness or resistance to penetration of materials, especially useful for small or thin samples or specific regions within a welded sample. For this analysis, the Struers Duramin-40 was utilized, following ASTM E384 standards. The Microhardness machine, depicted in Fig. 3.12, is detailed in Table 3.13. During testing, a Vickers diamond indenter with a 500-gram load is pressed into the surface of the material. This load induces penetration, causing permanent deformation in the shape of the indenter. The test is conducted under controlled conditions with pressure monitored for a dwell time of approximately 10 seconds. The diagonal length of the indentation is measured to calculate the Vickers hardness value using the standard formula.

Fig 3.12 Vickers Microhardness Testing Machine

Table 3.13 Specification of Vickers Microhardness Testing (Duramin-40)

Capacity	10 gf – 10 kgf
XY-stage	90 x 90 mm
Test height	0-200 mm
Overview camera	FOV 200 x 160 mm
Machine weight	101 kg
Evaluation camera resolution	18 MP

3.5 Selection of Input Parameters

In this study, the input parameters considered include Current (I), Welding Speed (WS), and CTWD (Z). The samples were fabricated using a DOE approach using the Taguchi L9 orthogonal array.

3.5.1 Design of Experiments

The Taguchi experimental design was selected for the fabrication of WAAM samples. If a different design were adopted, it would require many experiments. For the design of experiments, Taguchi L9 with 3 levels of 3 factors was utilized, as presented in Table 3.14, where A, B, and C are current (I), welding speed (WS), and CTWD (Z), respectively. Since every parameter was designed to be orthogonal to each other, no two components interacted with one another. Every component exists independently from the others.

Table 3.14 WAAM input parameters and their levels

Level	I (A)	WS (m/min)	Z (mm)
	A	B	C
1	100	0.5	2.5
2	110	0.6	3.0
3	120	0.7	3.5

Hence, the Taguchi L9 design, with three levels of 3 factors, was employed for the experiment design. The L9 orthogonal array with combinations of input parameters is presented in Table 3.15. Fabrication of nine WAAM samples (S1-S9) was conducted in a random sequence, adhering to the design specifications shown in Fig 3.13. The current (I), welding speed (WS), and CTWD (Z) settings were established based on Table 3.15 for each sample. The profiles of the CMT-WAAM samples are detailed in Table 3.16.

Table 3.15 L9 Orthogonal Array

Sample	A	B	C
S1	100	0.5	2.5
S2	100	0.6	3.0
S3	100	0.7	3.5
S4	110	0.5	3.0
S5	110	0.6	3.5

S6	110	0.7	2.5
S7	120	0.5	3.5
S8	120	0.6	2.5
S9	120	0.7	3.0

Table 3.16 Dimensions of Fabricated Samples

Sample	Height (mm)	Thickness (mm)	Avg. layer thickness (mm)
S1	99.68	5.38	2.49
S2	113.23	5.89	2.83
S3	99.34	5.31	2.48
S4	130.35	7.05	3.26
S5	113.24	6.52	2.83
S6	99.62	5.54	2.49
S7	127.35	7.06	3.18
S8	112.45	6.82	2.81
S9	99.75	6.30	2.49
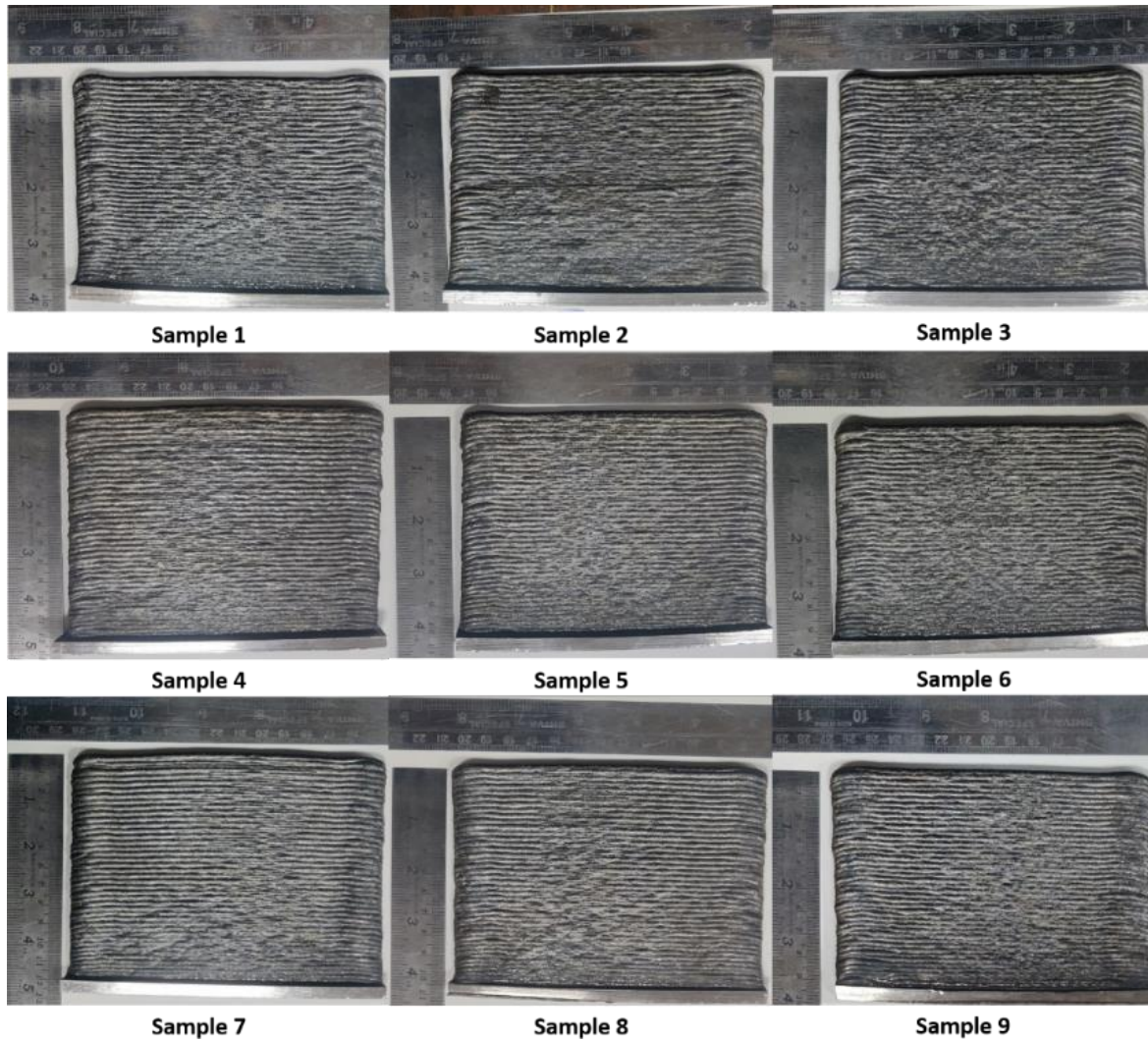
Fig 3.13 Robotic CMT WAAM Samples

3.6 Fabrication of WAAM Samples

The samples for this study were prepared using a KuKa Robot integrated with a CMT welding source. The main goal of the research is to fabricate thin-wall samples using the WAAM process. A series of trial runs were performed before finalizing the parameters to determine the optimal range of input parameters. This preliminary testing was essential to identify the suitable settings to ensure the successful fabrication of the thin walls, allowing for precise control over the material deposition and achieving the desired structural characteristics.

During the trial runs, it was observed that setting the current at 90 A resulted in incomplete fusion and improper bead formation, indicating insufficient energy for adequate material bonding. Conversely, raising the current to 130 A resulted in a much thicker wall than desired for thin-wall fabrication. This occurred because the higher current levels increased heat input, which caused excessive material deposition. The current was ultimately set within the range of 100 A to 120 A to strike a balance between these extremes. This range was chosen to provide adequate heat input for proper fusion and bead formation while maintaining the desired wall thickness for the WAAM process.

It was noted that setting the welding speed below 0.5 m/min resulted in a thicker wall due to excessive material deposition caused by increased heat transfer to the metal. On the other hand, increasing the welding speed beyond 0.7 m/min led to inadequate fusion during the process. The faster speed reduced the heat transfer to the metal, leading to inconsistent bead formation and poor bonding. A similar pattern was noted with the CTWD. When CTWD was set at less than 2.5 mm, the high heat transfer to the metal produced a thicker wall, while setting it beyond 3.5 mm resulted in inconsistent bead formation. This inconsistency was due to insufficient heat generation at the weld bead, highlighting the delicate balance required in setting the CTWD to achieve optimal results in the WAAM process. Trial run at I=130 A, WS=0.5 m/min, CTWD=3.00 mm is shown in Fig. 3.14

Fig 3.14 Trial Run of WAAM sample

With current, welding speed, and CTWD identified as the key independent parameters, optimizing these inputs to improve the quality of the WAAM-fabricated samples was crucial. A DOE was designed to facilitate this optimization, focusing on finding the best combination of these parameters. This DOE aimed to achieve superior mechanical and microstructural properties in the final samples. The Taguchi L9 orthogonal array was chosen for this purpose, providing a robust framework for systematically exploring the effects of each parameter. The specifics of the L9 orthogonal array are presented in Table 3.15, and the nine corresponding samples produced during this experimental phase are shown in Fig 3.13. WAAM sample just after fabrication is shown in Fig 3.15.
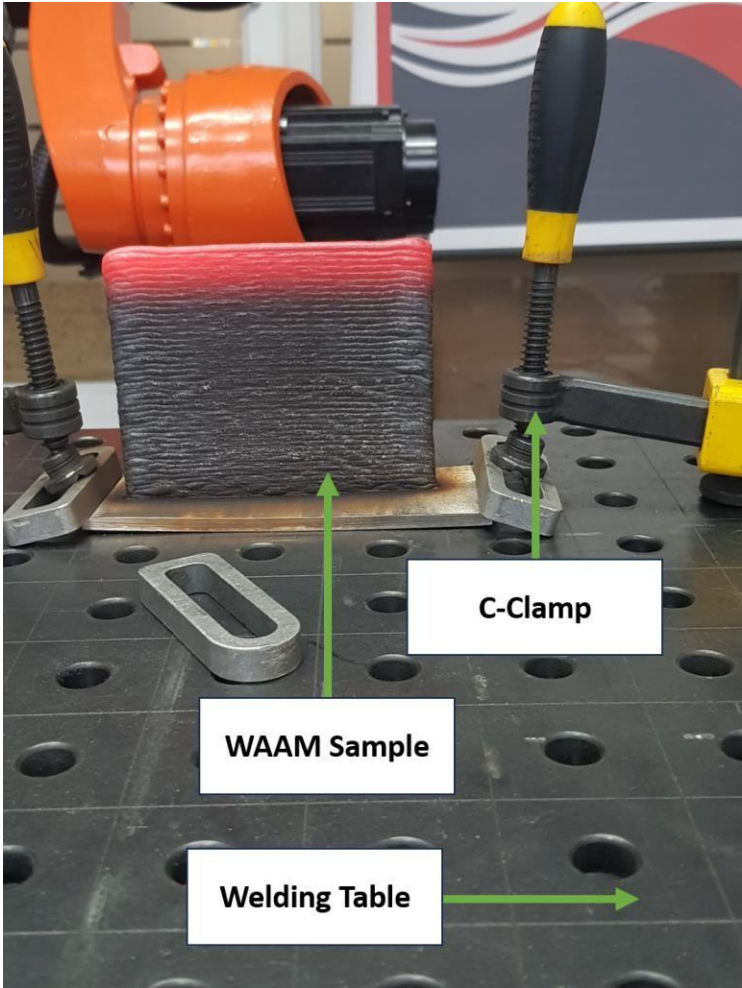
Fig 3.15 WAAM Sample After Fabrication

During the fabrication process, as well as after the completion of the WAAM samples, thermal images were captured using an Infrared Thermal Imaging camera. These images provided valuable insights into the temperature distribution and heat flow throughout the manufacturing process. The thermal images, which are crucial for understanding the thermal behavior of the samples during and after fabrication, are presented in Fig. 3.16.
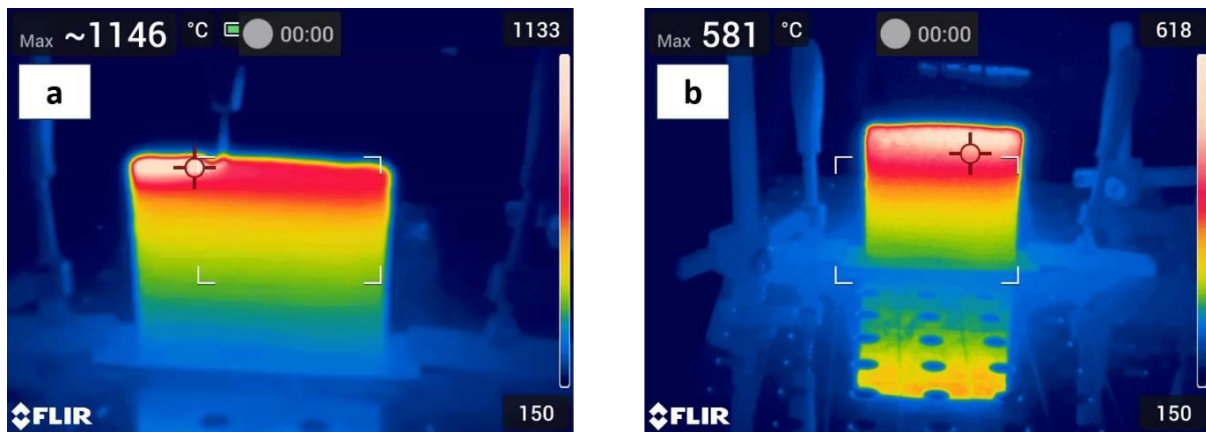
Fig 3.16 Thermal Imaging Camera (a) During Fabrication (b) After Fabrication

Summary

In summary, this study focuses on the detailed exploration of fabricating a multilayer structure of WAAM samples using 316L stainless steel through the Robotic-CMT process. The chapter provides an in-depth discussion of the various machines employed in the research and their technical specifications, highlighting their roles in the fabrication process. The DOE approach used to select the optimal parameters is also thoroughly examined.

Results and Discussion

4.1 Microstructure and Phase Analysis of SS316L WAAM Samples

This chapter thoroughly examines the SS316L WAAM samples fabricated using Robotic CMT welding for their microstructure and subjected to XRD analysis. The microstructural analysis includes detailed investigations using techniques such as optical and scanning electron microscopy (SEM) to reveal the grain structure, phase distribution, and potential defects or inclusions within the samples. To evaluate the crystalline structure, phase composition, and orientation of the fabricated samples, XRD analysis was performed. This detailed analysis provides a deeper understanding of the material properties and reveals the influence of the Robotic CMT welding process on the microstructure and quality of the SS316L WAAM samples.

4.1.1 Microstructure Analysis of SS316L WAAM

For macrostructure evaluation, a cross-sectional slice was taken from the multi-layered structure. The surface was then polished with abrasive papers of various grits (240, 400, 600, 800, 1000, 1200, and 2000) and finished with a 0.5-micron alumina paste on a cloth. Subsequently, the component was etched for 2 minutes in a solution of Hydrochloric Acid (HCl), Nitric Acid (HNO_3), and Glycerol ($C_3H_8O_3$) in the proportions of 40:20:40 to reveal a clearer microstructure and surface detail. Fig 4.1 shows the microstructure of the built multi-layered structure from nine samples. Grains were formed at different temperatures, resulting in variations in grain orientations at some levels. These observations suggest complete fusion with the absence of oxidation, which the continuous flow of argon shielding gas prevented. The microstructure of the extreme zones (top and bottom) showed no unwanted geometries, and the lack of porosity suggests that the component was defect-free.
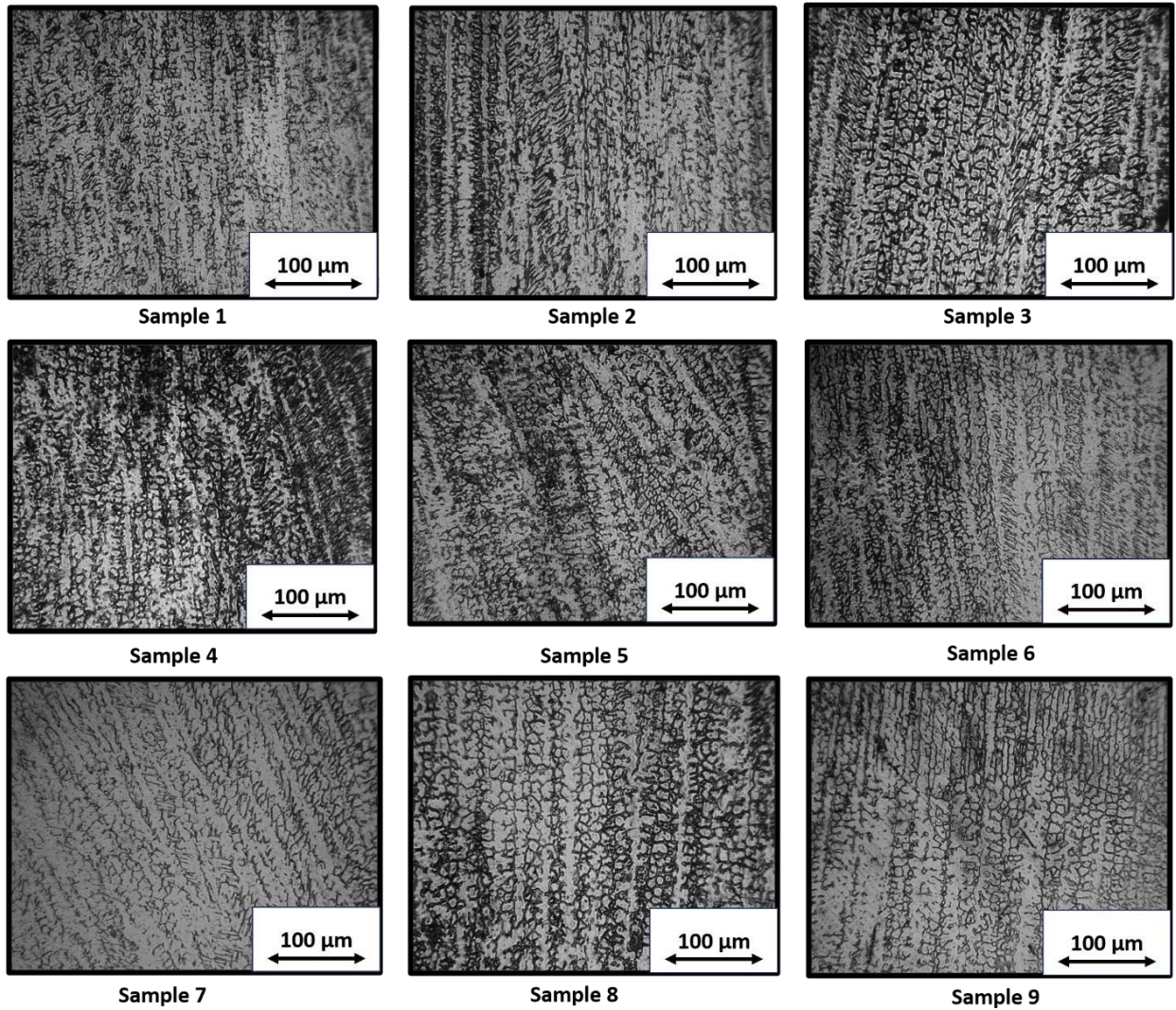
Fig 4.1. Microstructure of SS316L WAAM samples

Fig 4.2 shows the FESEM image of the WAAM sample. The prominent characteristic observed in the CMT-WAAM 316L samples was their multilayered microstructure, primarily from the intricate thermal histories involved. The multilayered structure exhibited alterations in ferrite, austenite, and residual stress. Fig 4.2 (a) FESEM image shows the occurrence of the WAAM sample's δ-ferrite phase, depicted in white and distributed within the γ-austenite matrix, with grain growth predominantly occurring in the vertical direction. During the initial solidification phases, ferrite was the main phase that precipitated from the liquid phase, followed by a distinct

accumulation of Cr and Mo atoms within the δ-ferrite. As ferrite grows, Ni atoms are released from the ferrite into the liquid phase, thereby establishing a favorable environment for the subsequent formation of γ-austenite.[136] Continuous deposition-induced heat accumulation, compounded by the concurrent cooling effect of the shielding gas, produced a subrapid cooling rate for the liquid alloy due to the cumulative thermal effects. Such thermal conditions led to a solidification behavior in the alloy characterized by the concurrent existence of the γ-austenite and δ-ferrite phases. In the early solidification stages, liquid metal witnessed the formation of high-temperature δ-ferrite. Following this, a transformation occurred where a segment of the δ-ferrite, along with the surrounding liquid, underwent a peritectic conversion into γ-austenite. Residual liquid at that point solidified directly, resulting in the formation of γ-austenite. Ongoing heat accumulation prompted the transformation of some primary δ-ferrite phases into γ-austenite. The residual ferrites were then dispersed within the austenitic matrix, forming a net-like and skeletal structure.[137] The optical microscopy image shown in Fig 4.2 (b), the WAAM's microstructure, demonstrates a ferrite-austenite mode. Fig 4.2 (c) shows the FESEM image of WAAM sample with lathy and skeletal ferrite. In this microstructure, γ-austenite serves as the primary phase, while δ-ferrite at the grain boundaries of γ-austenite. Both lathy (parallel structure) and skeletal (dispersed structure) structures were observed in δ-ferrite. A substantial enrichment of Cr (21.6%) and Ni (3.6%) within the microstructure is unveiled through the EDX analysis results plot and chemical spectrum presented in Fig 4.3.
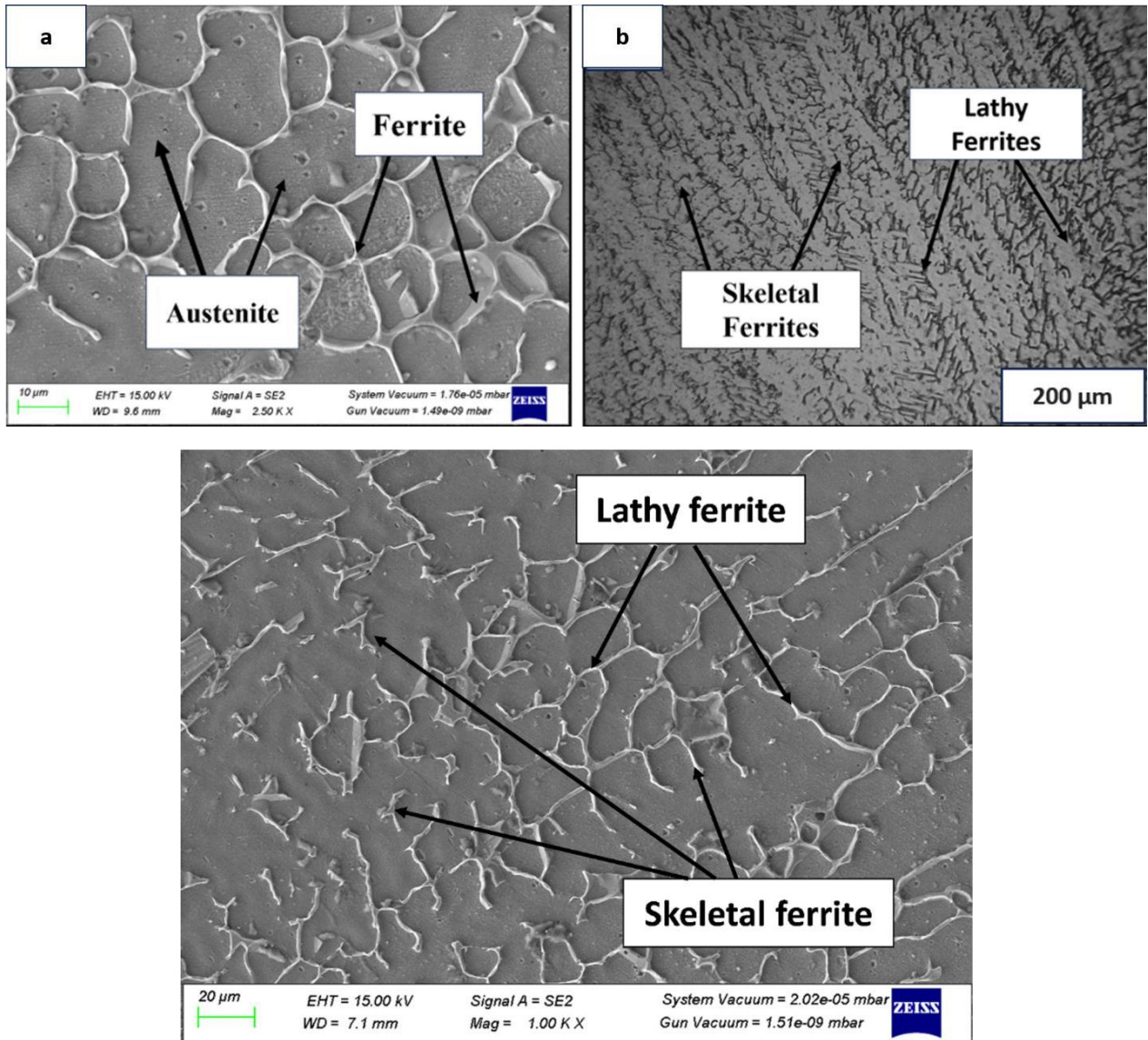
Fig 4.2 (a) FESEM of WAAM, (b) Optical Microscopy of WAAM, (c) FESEM of WAAM

The solidification modes, based on the chemical composition,

A mode: $\qquad$ $Cr_{eq}/Ni_{eq} < 1.25$,

A-F mode: $\qquad$ $1.25 < Cr_{eq}/Ni_{eq} < 1.48$,

F- A mode: $\qquad$ $1.48 < Cr_{eq}/Ni_{eq} < 1.95$

F mode: $\qquad$ $Cr_{eq}/Ni_{eq} > 1.95$

where, Cr_{eq}/Ni_{eq} is determined using the Schaeffler formula, which is calculated through the

following equation:

$$Cr_{eq} = Cr + Mo + (1.5 \times Si) + (0.5 \times Nb) \qquad 1$$

&

$$Ni_{eq} = Ni + (30 \times C) + (0.5 \times Mn) \qquad 2$$

Where A-Austenite & F-Ferrite.[138] For the WAAM sample, the Cr_{eq}/Ni_{eq} value is 1.92 ($Cr_{eq}/Ni_{eq} = 21.86/11.36$), while for wrought 316L, the Cr_{eq}/Ni_{eq} value is 1.86 $Cr_{eq}/Ni_{eq} = 20.23/10.85$). Therefore, the solidification mode of the deposited components was characterized as the F–A mode.
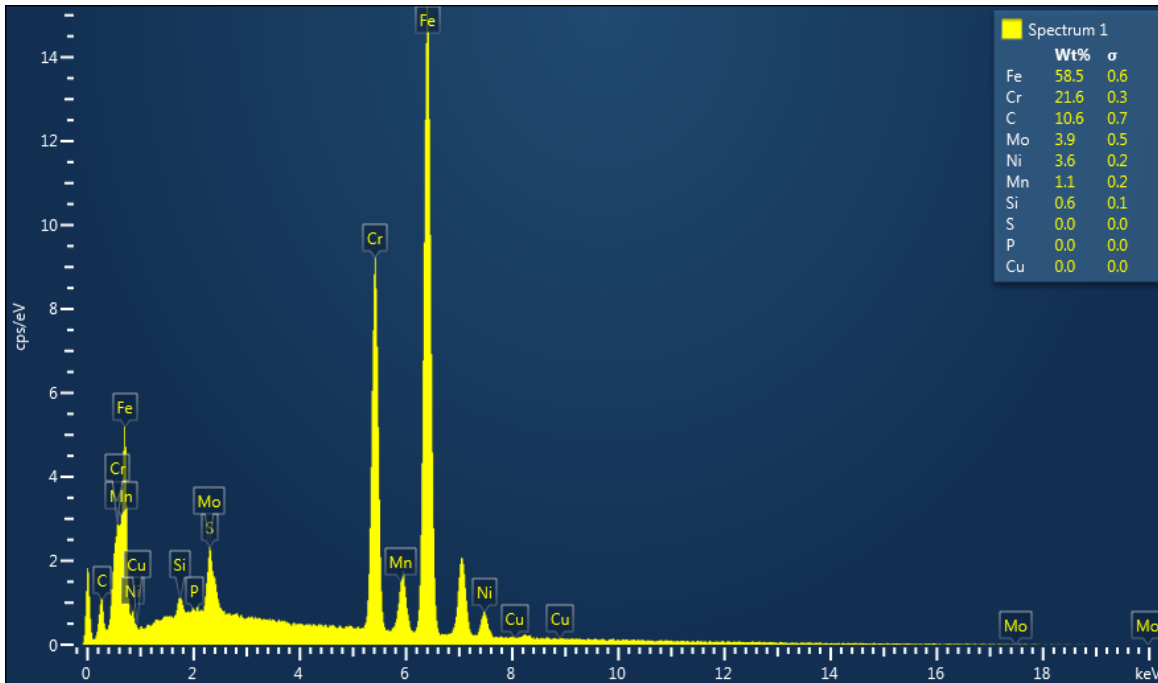
Fig 4.3 EDX plot of WAAM sample

4.1.2 Phase Identification of WAAM Samples

The XRD spectrum Fig 4.4 (a) & Fig 4.4 (b) of the WAAM sample and wrought SS316L, respectively, revealed that several austenite and ferrite phases were examined. The wrought SS316L and WAAM sample's primary phase was γ phase, and its favored crystal plane was (111). The diffraction peaks observed at 41°, 50°, and 74° correspond to austenite (JCPDS No 01-071-

4649). The presence of δ-ferrite is indicated by the peak at 42°. Consequently, both the WAAM

sample and wrought SS316L consist of δ-ferrite and γ-austenite. The high diffraction peaks of the

austenite planes {111} and {200} show that these are the two most favorable orientations of the

dendrites. Furthermore, the XRD patterns of the deposited section demonstrate the predominant

phase, and the results are consistent with the WAAM and wrought SS316L microstructure.
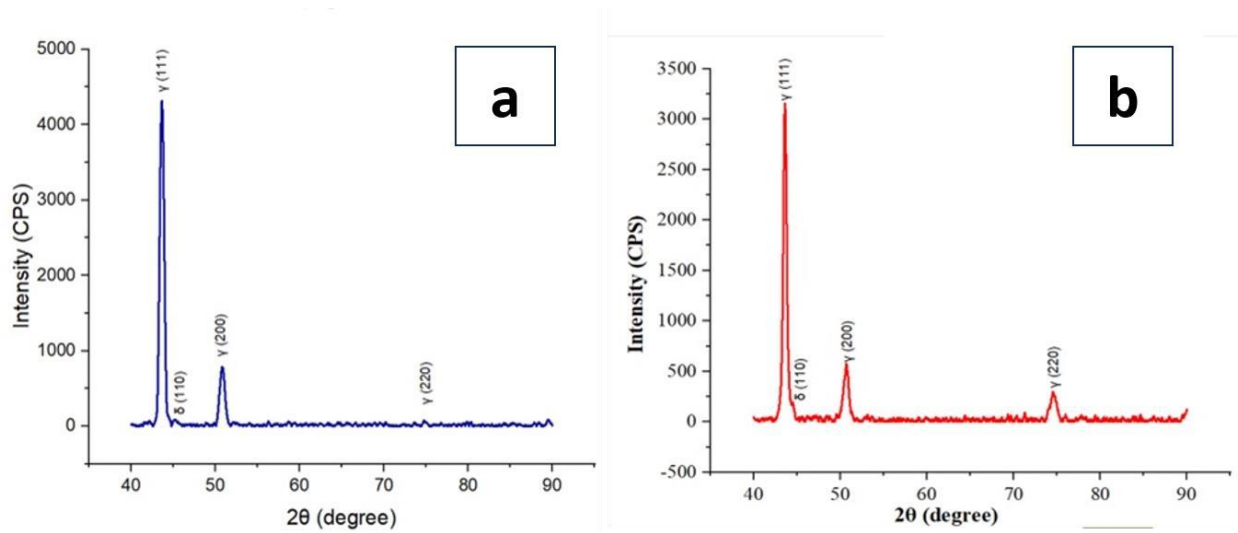
Fig 4.4. XRD plot (a) SS316L WAAM & (b) Wrought SS316L

4.1.3 Fractography

The fracture surfaces are illustrated in Fig 4.5 (a), and the FESEM fractography of tensile coupons

for WAAM and wrought 316L are illustrated in Fig 4.5 (b) and Fig 4.5 (c). The fractured surface

of the tensile specimens revealed distinct signs of equiaxed dimples and void deposition across the

layers. A significant number of dimples, evenly distributed across the fracture surface, confirmed

a ductile fracture mode and implied satisfactory toughness in the as-formed materials.[139] The

EDS graph for WAAM and wrought steel is presented in Fig 4.6 (a) and 4.6 Fig (b). EDS results

concluded that the oxygen weight percentage for the WAAM and wrought steel was 1.4 and 1.3%

respectively, indicating a low oxidation level. A significant presence of oxygen implies that the

oxidizing impurities are present within the dimples, which generally act as a source of brittleness and initiate cracks.[140] Fig 4.7 shows the FESEM images of all 9 samples fractured surface.
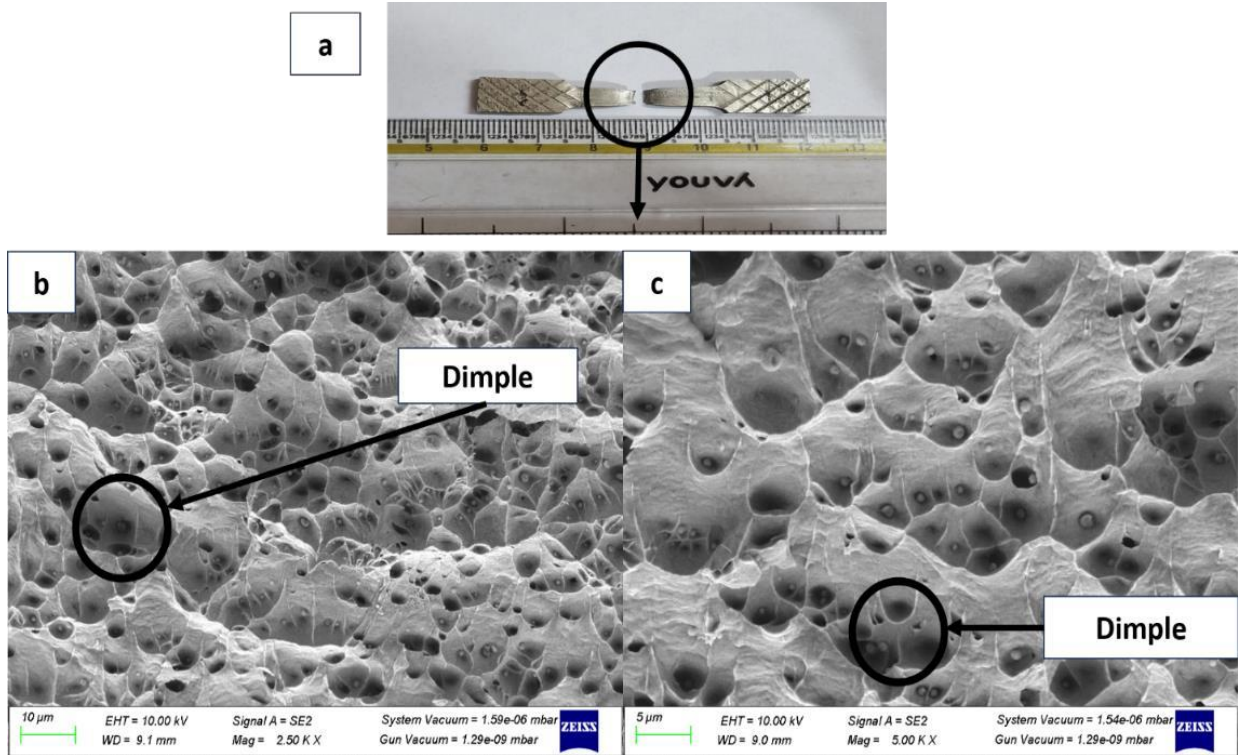
Fig 4.5. (a) Fracture image of Tensile Specimen (b) FESEM of WAAM (c) FESEM of Wrought 316L
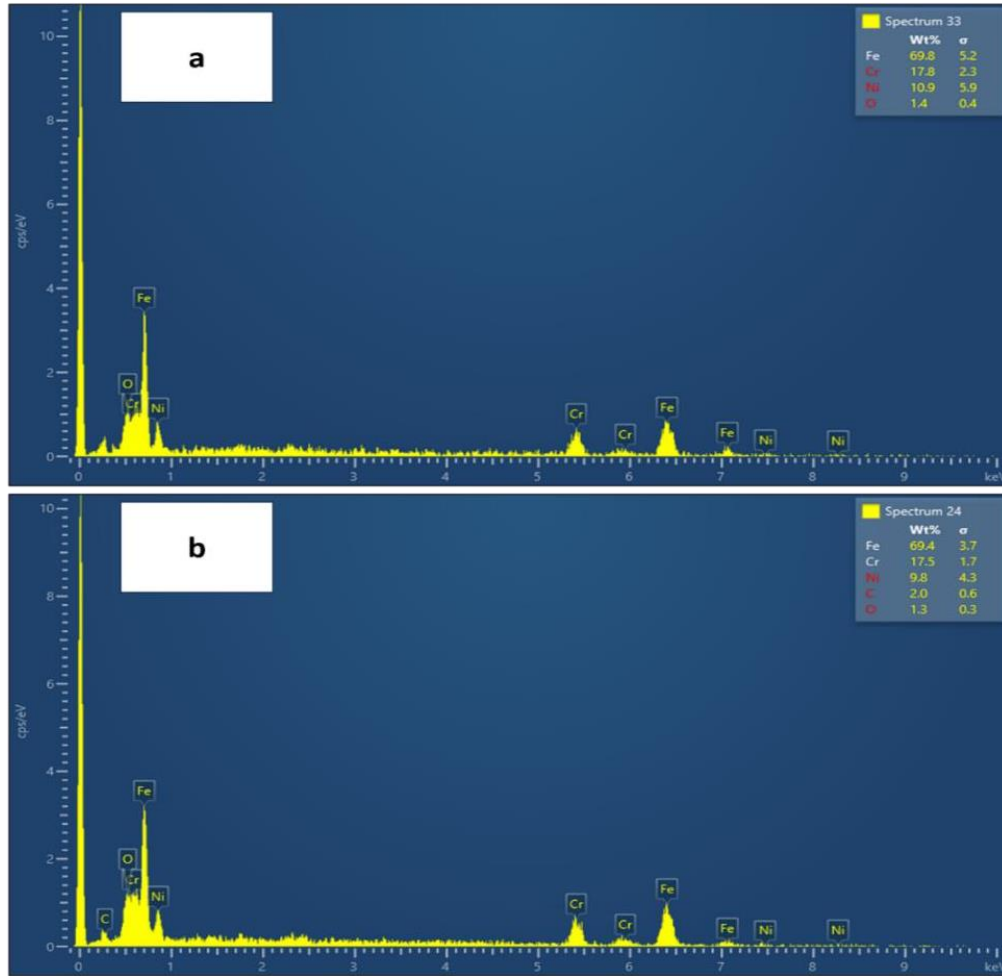
Fig 4.6 (a) EDS Fractured WAAM (b) EDS Fractured Wrought 316L

4.1.4 X-Ray Tomography Results

To determine the porosity levels in WAAM and wrought 316L stainless steel, X-ray CT scanning was employed. Samples were extracted using wire cut EDM, with dimensions set at $10 \times 10 \times 3$ mm³ for WAAM and $10 \times 10 \times 5$ mm³ for wrought steel. Before conducting the scan, the samples were carefully polished with emery paper, progressing from 400 to 2000 grit, to ensure precision in the results. X-ray radiography was then performed in all directions, revealing no porosity in the WAAM or wrought steel samples, as depicted in Fig 4.8.
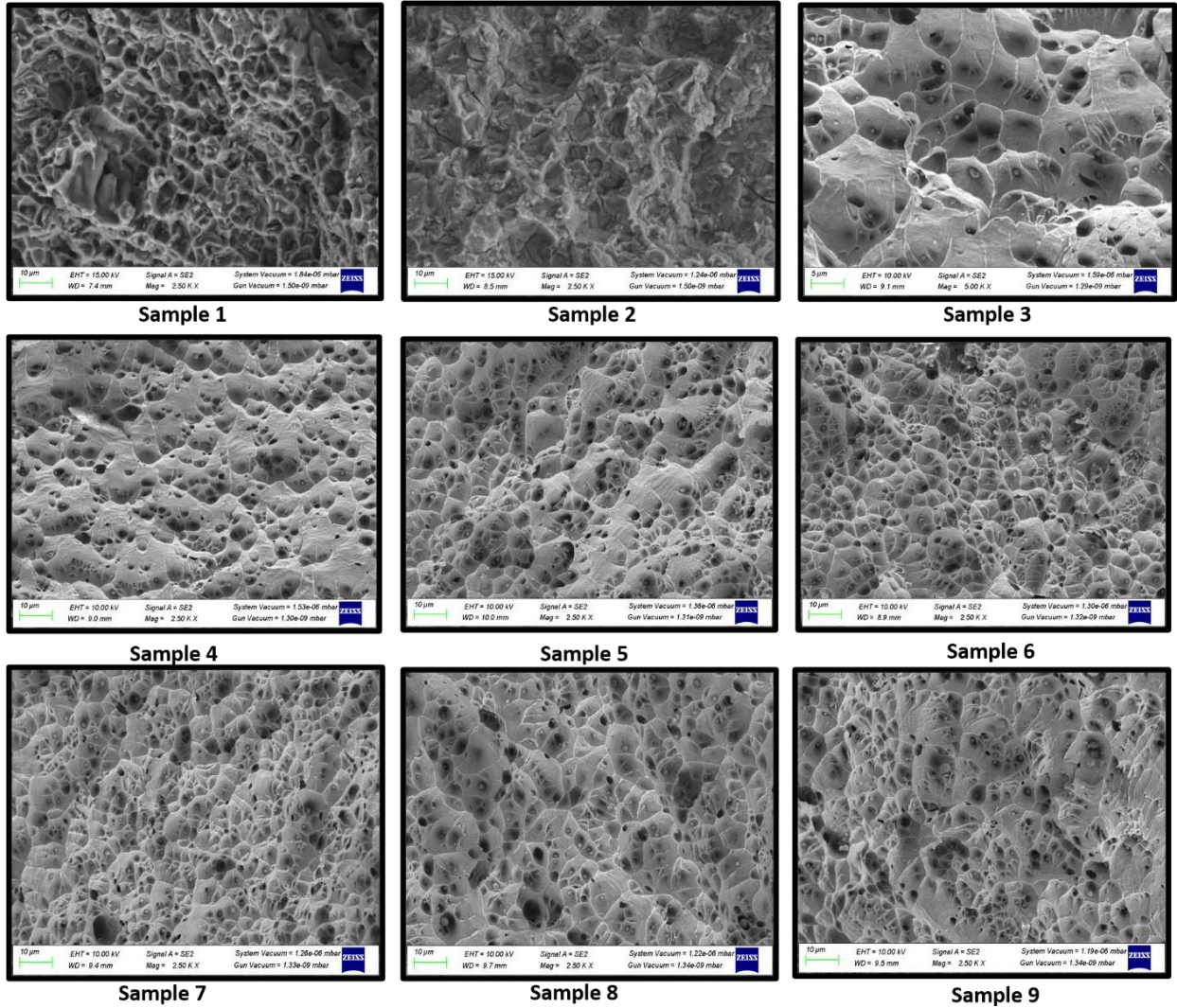
Fig 4.7 Fractography of WAAM Tensile Samples

However, when full WAAM samples were analyzed through X-ray CT scanning, as shown in Fig 4.9, porosity was detected near the base, specifically in the first and second beads. Beyond this region, no porosity was observed, indicating that WAAM-fabricated samples are highly dense and well-suited for dynamic loading applications. This suggests that WAAM can be a superior alternative to casting, potentially eliminating porosity issues and producing components that rival those made through forging.
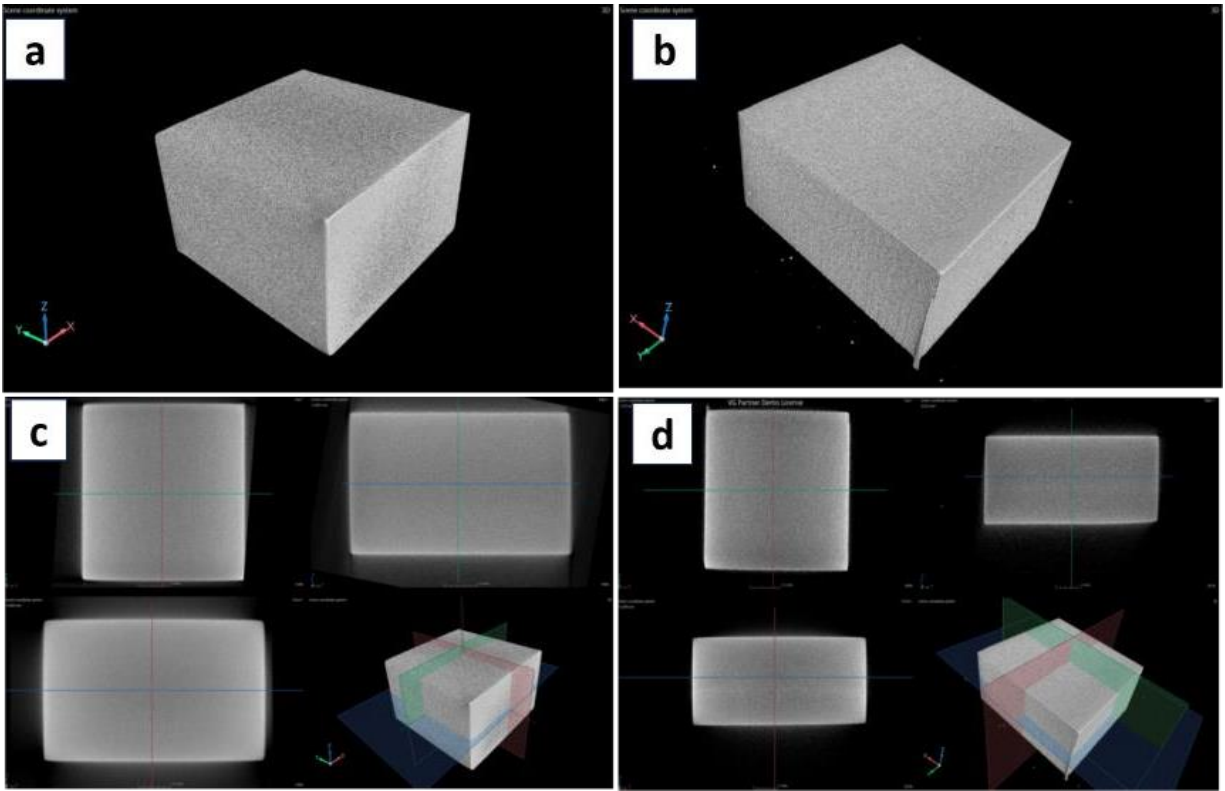
Fig 4.8 (a) CR 316L (b) WAAM (c) CR 316L Sectioning (d) WAAM Sectioning
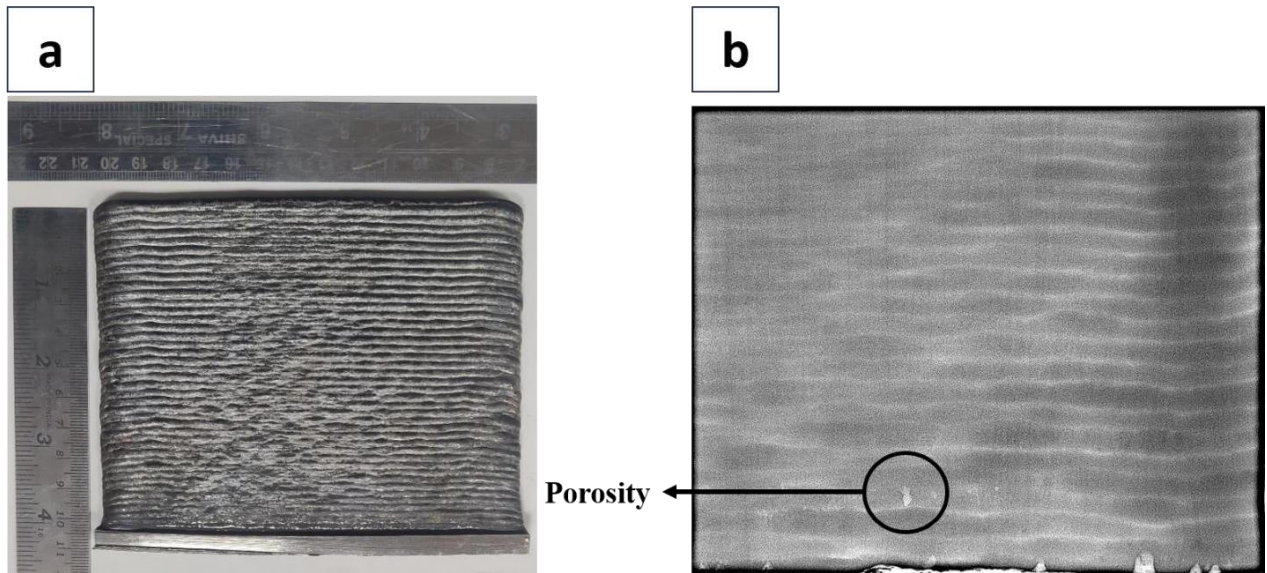
Fig 4.9 (a) Fabricated WAAM (b) X-ray CT scan of WAAM sample

Summary

The microstructural analysis of WAAM and wrought SS316L samples revealed a composition primarily consisting of γ-austenite and δ-ferrite. Notably, the δ-ferrite displayed both lathy and skeletal structures, contributing to the material's unique properties. Energy Dispersive X-ray (EDX) analysis further highlighted significant enrichment of chromium (21.6%) and nickel (3.6%) in these phases. The diffraction patterns for both samples showed prominent peaks at the {111} and {200} planes, indicative of favorable dendrite orientations. These orientations enhance the material's overall stability and performance. Examination of the tensile specimens' fractured surfaces showed equiaxed dimples and void deposition, suggesting a ductile fracture mode with satisfactory toughness. X-ray CT scan results also confirmed the absence of porosity in both WAAM and wrought steel samples. This finding is particularly promising, as it suggests that the WAAM process could effectively replace traditional casting methods, which are often plagued by porosity issues.

4.2 Mechanical Properties: Microhardness, Tensile Test and Residual Stress Measurement

This section explores the mechanical properties of the SS316L WAAM samples, focusing on tensile behavior, microhardness, and residual stress. Understanding these properties is vital for assessing the material's performance, durability, and reliability in practical applications. Tensile behavior provides insights into the material's strength and ductility, revealing how it responds to external forces. Microhardness measurements offer detailed information on the hardness distribution across the structure, highlighting any variations due to the fabrication process. Residual stress analysis is crucial for detecting internal stresses impacting the material's structural

integrity and lifespan. Combined with other evaluations, this analysis offers a thorough understanding of the mechanical properties of the SS316L samples.

4.2.1 Tensile Test Results

The tensile testing was performed on an INSTRON instrument (Model: 4482, USA) at a controlled, steady speed of 1 mm/min. This consistent testing rate was carefully maintained to ensure the accuracy and consistency of the tensile property data obtained during the experiment. The highest tensile strength among the samples is achieved by Sample 5 reaching 599 MPa, while the lowest is observed in Sample 8 at 491 MPa. Furthermore, the UTS for the remaining samples range between 505 to 587 MPa, representing 85.55% to 99.4% of the UTS of rolled steel (590 MPa). These findings are based on tensile strength assessments carried out in the transverse direction, known to be the orientation that produces the weakest strength measurements. Many practical applications adhere to an operational approach that restricts work to the elastic region. This approach ensures that stresses remain below the threshold for plastic deformation, thereby mitigating the risk of failure. As a result, stress is diligently regulated to stay below the elastic limit. The yield strength (YS) of the fabricated samples displayed a remarkable rise, reaching approximately 290 MPa, representing a substantial improvement over the 230 MPa yield strength commonly observed in traditionally manufactured stainless steel. This notable advancement underscores the superior mechanical properties exhibited by the fabricated samples. Fig 4.10 presents the Stress-Strain diagram for the WAAM samples. A notable range of PE, from 43.8% to 59.6%, is observed among the fabricated samples under varying process parameters. Maximum PE was observed in sample 7. The analysis indicates a significant enhancement in ductility for the fabricated samples utilizing CMT compared to other conventional manufacturing processes.
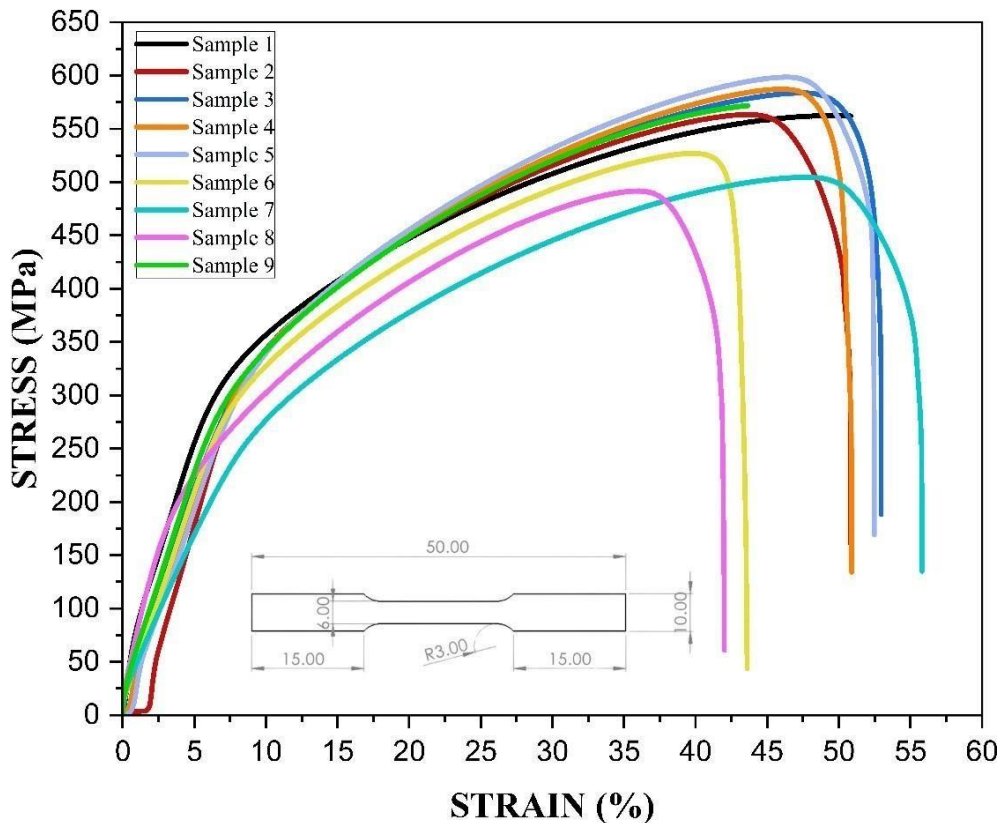
Fig 4.10 Stress-Strain diagram for WAAM samples

Tensile testing was performed on both SS316L WAAM with parameters Current (A) 100, welding speed 0.7 (m/min), CTWD 3.0 (mm) and wrought SS316L, with the results visually depicted in Fig 4.11. SS316L WAAM ultimate tensile strength (UTS) measured 592.31 MPa, accompanied by a yield strength (YS) of 276.46 MPa. Additionally, the ultimate tensile strength of wrought steel was measured at 557.62 MPa, yielding 284.39 MPa. SS316L WAAM showcased superior tensile strength with a 6.28% increase in performance compared to the wrought material. The WAAM part exhibited a percentage elongation of 53.20%, while conventional manufactured steel recorded a slightly higher percentage elongation of 59.85%. The variations in the tensile properties of SS316L WAAM are mainly due to the heterogeneous microstructural changes caused

by the thermal stresses experienced during the fabrication of multilayer structures.[141] Kumar et al. in their research for SS316L reported similar results.[142] Fig 4.12 demonstrates the bar chart for comparing tensile properties of WAAM and wrought 316L.
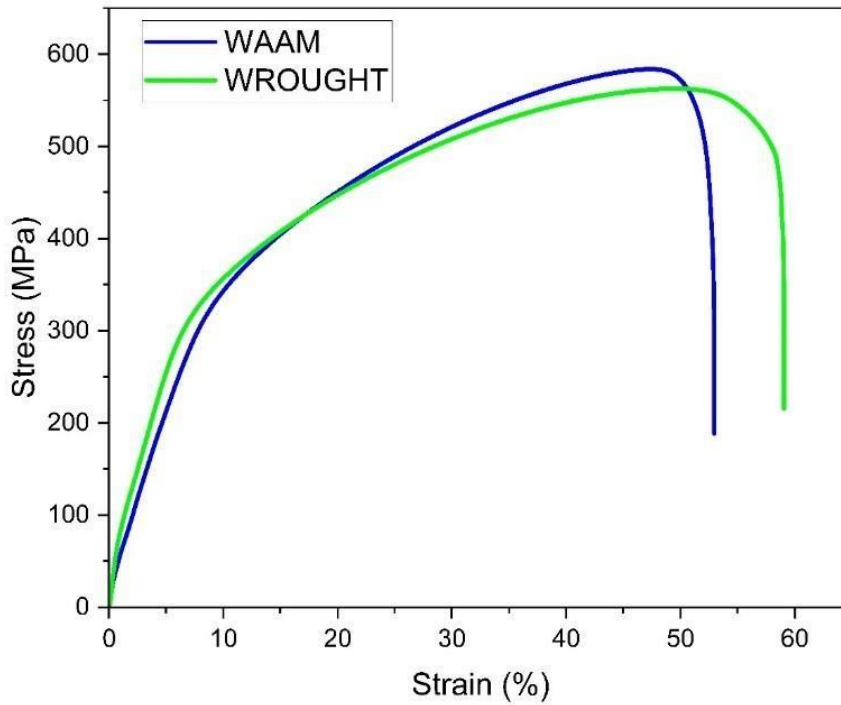
Fig 4.11 Stress-Strain curve for WAAM and Wrought SS316L

4.2.2 Microhardness Results

Microhardness measurements were conducted at seven positions along the vertical direction. In the horizontal direction, ten readings were recorded, and the average of these readings was used for analysis. Averaging the values helped streamline the analysis. Furthermore, the test results unveil the MH range from 215 to 280 HV. Fig 4.13 depicts the variation in hardness along the vertical axis. The increased hardness observed near the base results from the effective heat dissipation, facilitating quicker cooling rates relative to the top section.
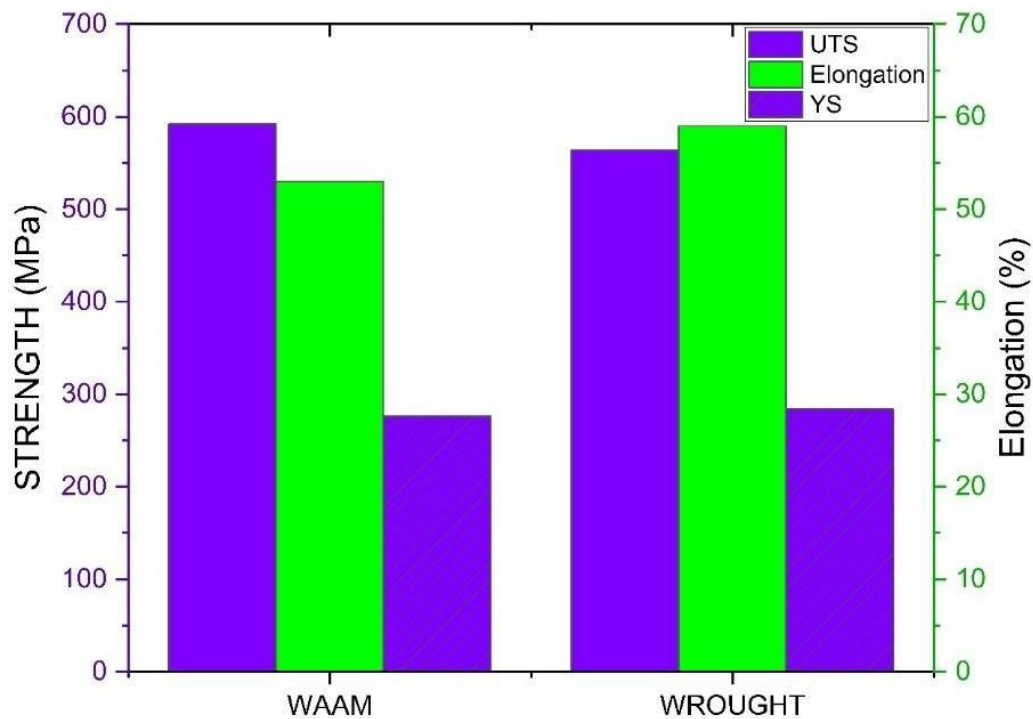
Fig 4.12 Bar chart of Tensile properties of WAAM and Wrought 316L

The findings indicate an uneven temperature distribution, with hardness gradually decreasing from the base to the top. Similar observations were reported by Denovitzer et al., demonstrating a trend wherein hardness values decreased as the distance from the substrate increased while registering higher values nearer to the substrate.[143] Hardness is higher near the base due to its more efficient heat dissipation, with results showing a gradual decrease in hardness as you move from the base to the top, reflecting an uneven temperature distribution. The coarse microstructure in the top region slows down the cooling rate, leading to lower hardness values and validating the Hall–Petch relationship. On the other hand, higher micro-hardness values indicate increased heat input, finer grain refinement, and better heat dissipation.[144] This can be attributed to the fine-grain strengthening resulting from the rapid cooling effect of the substrate, which leads to increased

microhardness at the bottom of the samples. The uniform MH values observed across all zones suggest consistent structural behavior, mitigating the potential for brittle failure. the accumulation of significant heat between layers results in a continuous reduction in hardness as time progresses.[145]

Microhardness testing was performed on both SS316L WAAM with parameters Current (A) 100, welding speed 0.7 (m/min), CTWD 3.0 (mm), and wrought SS316L; test was conducted at seven positions spanning from the bottom (near the base) to the top, as depicted in Fig 4.14. It was observed that the hardness steadily reduced from the base to the top due to a non-uniform temperature distribution.[146] Microhardness evaluation conducted on the WAAM sample reveals an average value of 242.74 HV near the base, followed by a midrange value of 231.57 HV in the middle zone. The top zone exhibits an average microhardness measurement of 217.24 HV. The WAAM sample displayed a maximum hardness value of 246.63 HV near the base, with the lowest value of 209.10 HV measured at the top. Compared to the top and middle zones, a slight increase in microhardness was observed in the bottom zone, which is likely associated with the larger heat dissipation from the substrate plate. The uniformity in hardness values across all zones suggests consistent behavior within the built structure, reducing the potential for brittle failure. In contrast, as time passes, there is a substantial increase in heat accumulation between layers, leading to a gradual decline in hardness.[147] It has been found that the average microhardness of the SS316L WAAM is larger than the wrought 316L, which has a hardness of 192 HV. This observation is supported by numerous studies in the literature, indicating that the microhardness of additive-manufactured parts of 316L SS is generally higher than the conventionally manufactured 316L SS parts.[148]
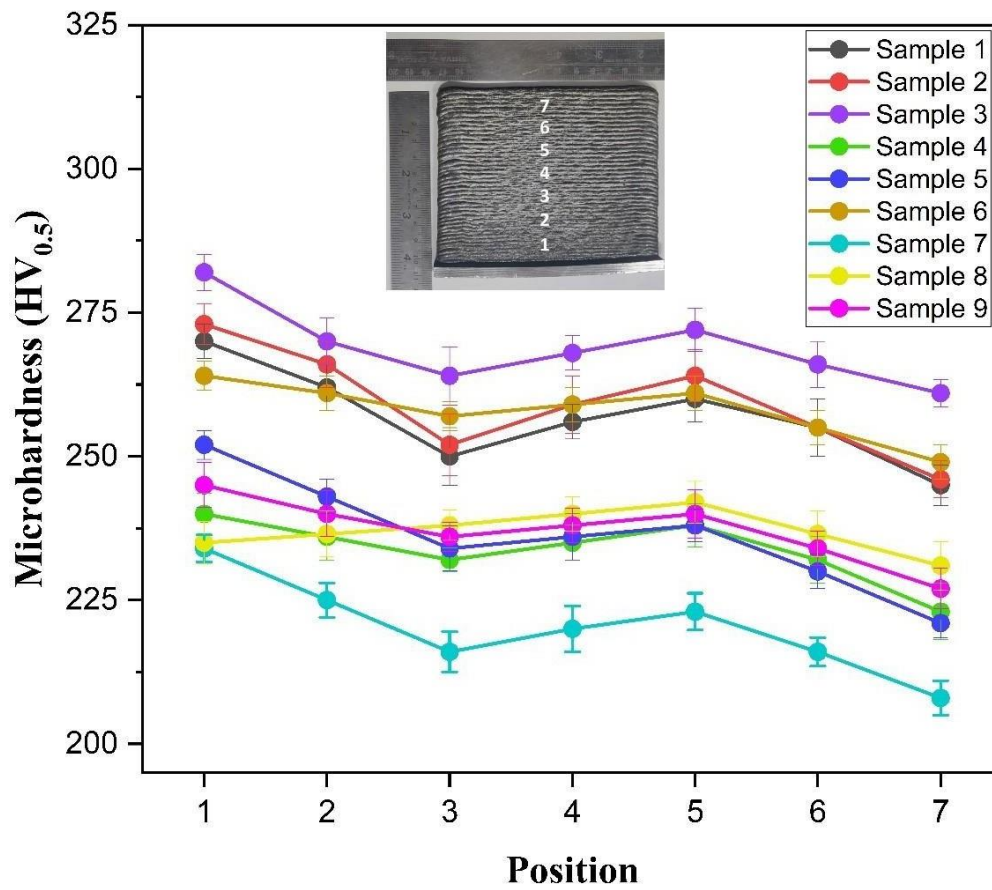
Fig 4.13 Microhardness variation of WAAM samples
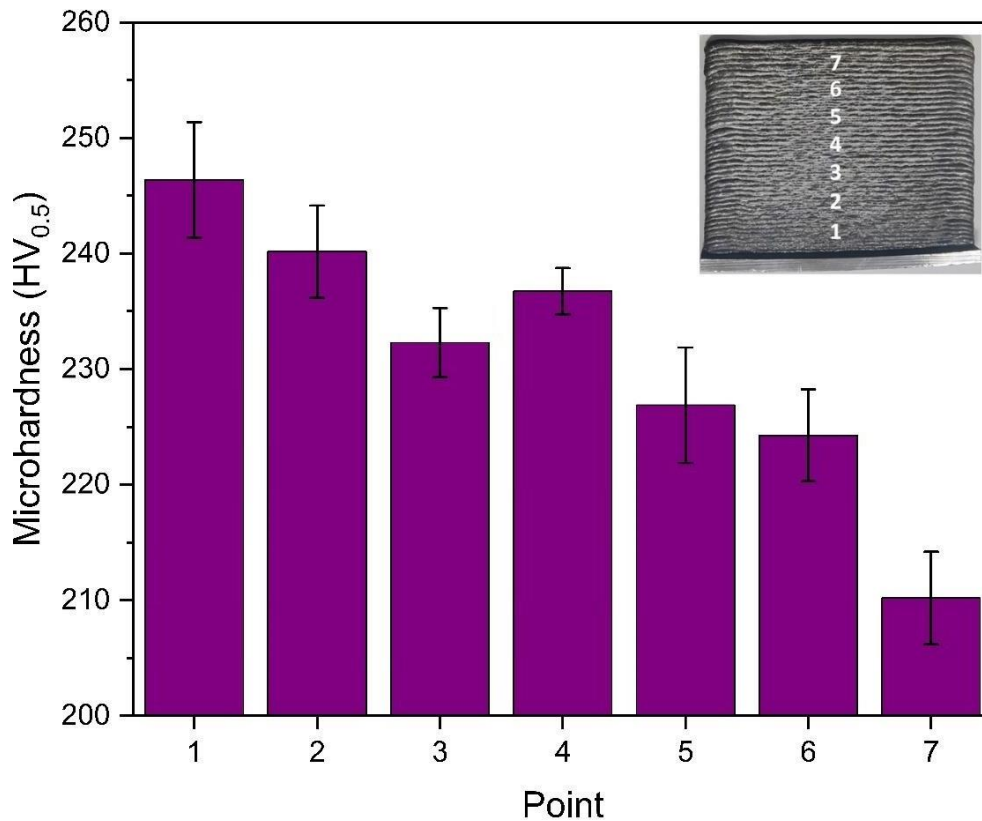
Fig 4.14 Microhardness plot of WAAM sample

4.2.3 Residual Stress Measurement Results

RSM were conducted at three regions from bottom to top (1-3). Five readings were taken in the horizontal direction, with the average value employed for the analysis. Compressive RS, generated due to high heat input and rapid cooling, enhances the fatigue strength of WAAM samples. When subjected to tensile loads, tensile RS promotes the initiation and propagation of cracks, ultimately resulting in tensile failure. Compressive RS is most pronounced at Position 1 on the welding base, primarily due to stress concentration. Conversely, locations away from the base in the transverse direction undergo tensile RS. At point 1 near the substrate, compressive RS is generated. The cold substrate causes the bottom fiber to yield tensile stresses in the longitudinal direction (in the

direction of welding) leading to the bending of the substrate. This results in compressive stresses at the layers of WAAM near the substrate. When the temperature gradient disrupts the connection between the WAAM layers and the substrate, tensile RS increases as the WAAM height grows[147]. Fig 4.15 displays the variation of RS in the vertical direction. This research's primary consideration is the average RS, with a comprehensive analysis conducted on nine samples. A collective analysis of nine samples consistently demonstrates a compressive nature in the average stress values.
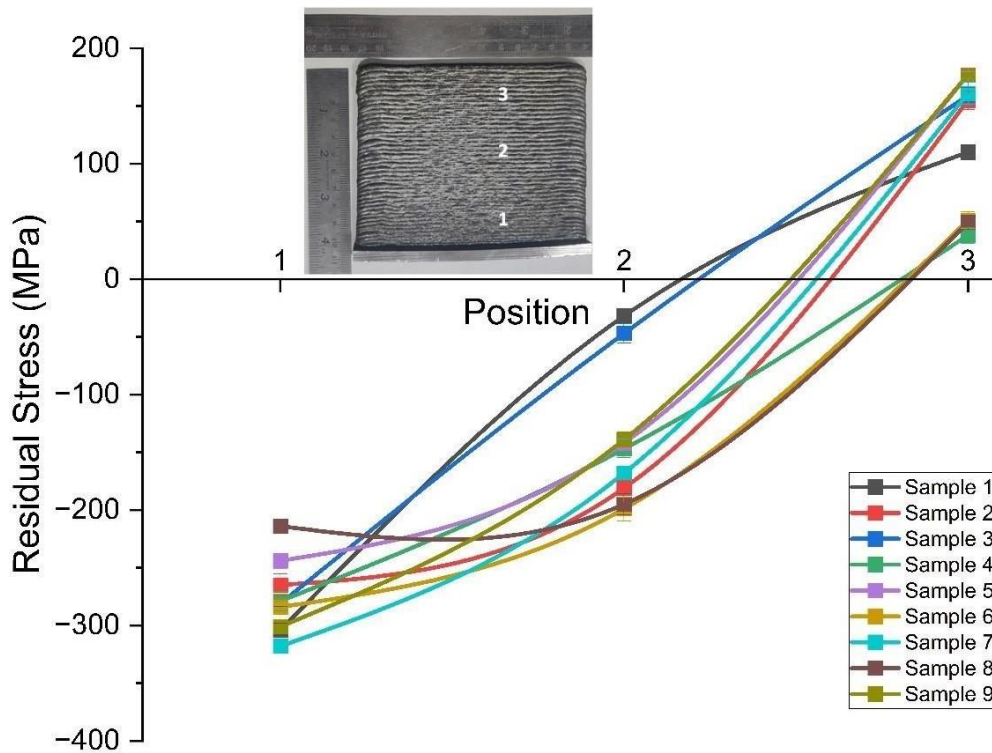
Fig 4.15 Residual Stress distribution of WAAM samples

RSM for samples with I - 110 A, WS - 0.5 m/min & CTWD - 3.0 mm were conducted at six specific positions in the vertical direction of SS316L WAAM from bottom (at base) to top. These

results are presented in Fig 4.16. The RS was measured at the base with a 280 MPa (compressive) value and progressively rises to 78 MPa (tensile) at the uppermost point. Across the entire surface of the SS316L WAAM, the average RS stands at 124 MPa (compressive), whereas the RS recorded for the wrought steel is 142 MPa (compressive). The observation reveals a transition in RS within the structure, shifting from compressive at the base to tensile at the uppermost part. The average RS in the AISI 316L WAAM is 87% of the wrought steel. Neto et al. conducted RSM on SS 304 WAAM components. Their findings consistently revealed the presence of compressive RS in the transverse direction. The RS remained compressive in the WAAM–Base interface, with a particularly high degree of compressive stress. Tensile longitudinal RS were observed in the uppermost layer, stemming from elevated constraints on metal shrinkage. This phenomenon arises due to already solidified metal in the longitudinal direction, leading to the development of compressive stresses. In the case of the uppermost layer, which is not reheated, this creates tensile stresses. Notably, the magnitudes of these RS remain below the material's YS.[148] WAAM yields superior results in RS compared to the SLM powder-based DED method.[149]
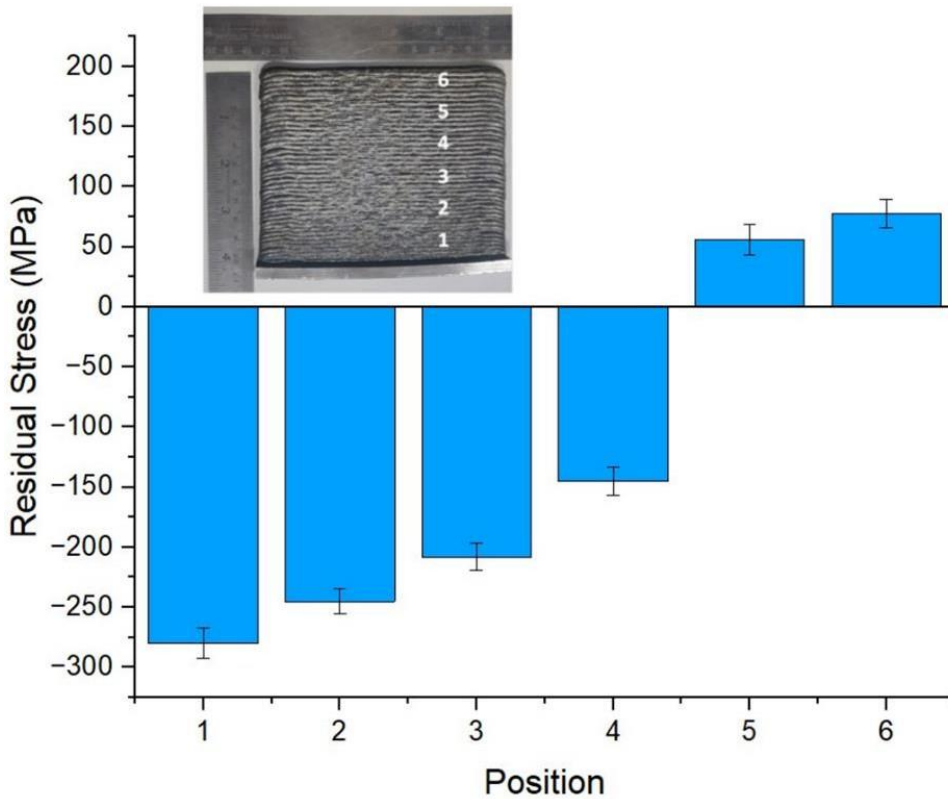
Fig 4.16 Residual Stress of SS316L WAAM

The graphical representation in Fig 4.17 (a) provides a visual depiction of the D-S ring distortion and the presence of the (311) peak across a range of SS316L WAAM in the vertical direction at six positions from bottom (at base) to top. Fig 4.17 (b) shows the wrought steel's D-S ring and Distortion Graph. The D-S ring observed on a two-dimensional detector through a single X-ray source is a crucial operational principle of the cos α method. This method is based on the assumption of continuous Debye-Scherrer (D-S) rings.

However, D-S rings may exhibit intermittent characteristics when the irradiated region lacks sufficient grains due to coarse grain sizes or a limited irradiated area. Ensuring the continuity of D-S rings necessitates an irradiated area that encompasses a sufficiently high number of diffracting grains. D-S rings serve as a valuable source of microstructural data, revealing pertinent information about grain sizes and texture.

Nevertheless, generating continuous D-S rings can be particularly challenging when dealing with coarse grain structure. The graphical representation in Fig 4.17 (a) is dedicated to cos α and sin α diagrams for the SS316L WAAM, meticulously examined at six locations in the transverse direction. The wrought steel is also presented in Fig 4.17 (b). Notably, the inclination angle of the red fitting line and the elastic constant values are crucial in representing RS (σx) in the cos α plots. Conversely, in the sin α plots, these parameters indicate shear stress (τxy).

A positive slope in the cos α diagram signifies the presence of compressive RS, while a negative slope indicates tensile RS. The cos α diagram slopes were calculated as 0.001143, 0.000927, 0.000849, 0.000807, -0.000115 & -0.000148 for SS316L WAAM & 0.000433 wrought steel. The measured shear stress values for the WAAM sample for six positions in a transverse direction from bottom (near base) to top and wrought steel are -36±5, -71±8, -26±7, -93±2 -79±4 and 105±3 MPa for SS316L WAAM & 25±5 MPa for wrought steel shown in Fig 4.18 (a). The findings align with the investigations carried out by Tanaka.[135] In Tanaka's study, it is highlighted that negative slopes of the cos α diagram are indications of tensile RS. Analysis of Fig 4.18 (b) highlights the presence of positive shear stress in the SS316L CR plate conversely, when examining the SS316L WAAM, a predominantly negative slope is observed, except in the topmost position.
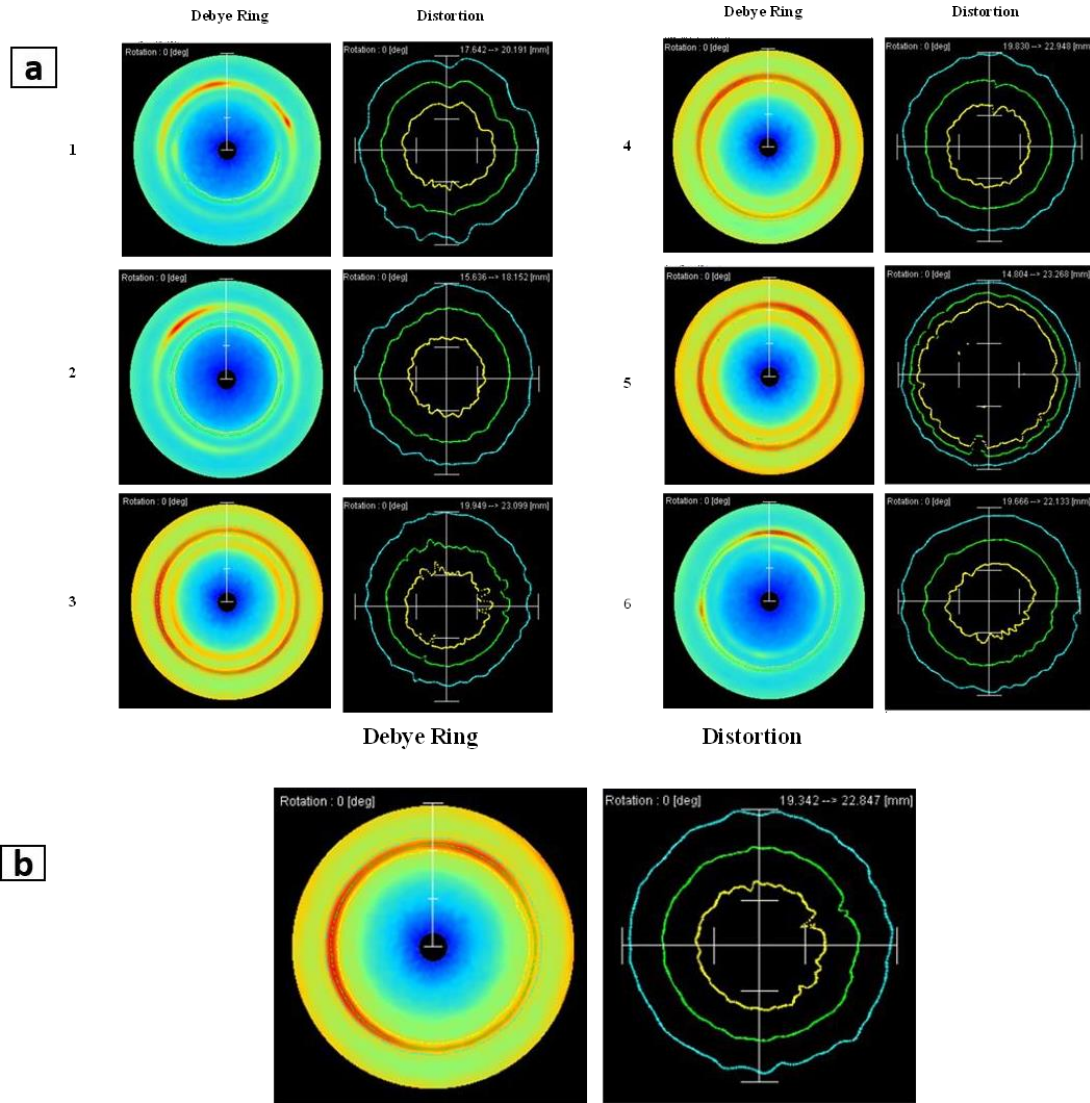
Fig 4.17 Debye Ring & Distortion Graph of (a) SS316L WAAM at 6 locations (b) Wrought Steel
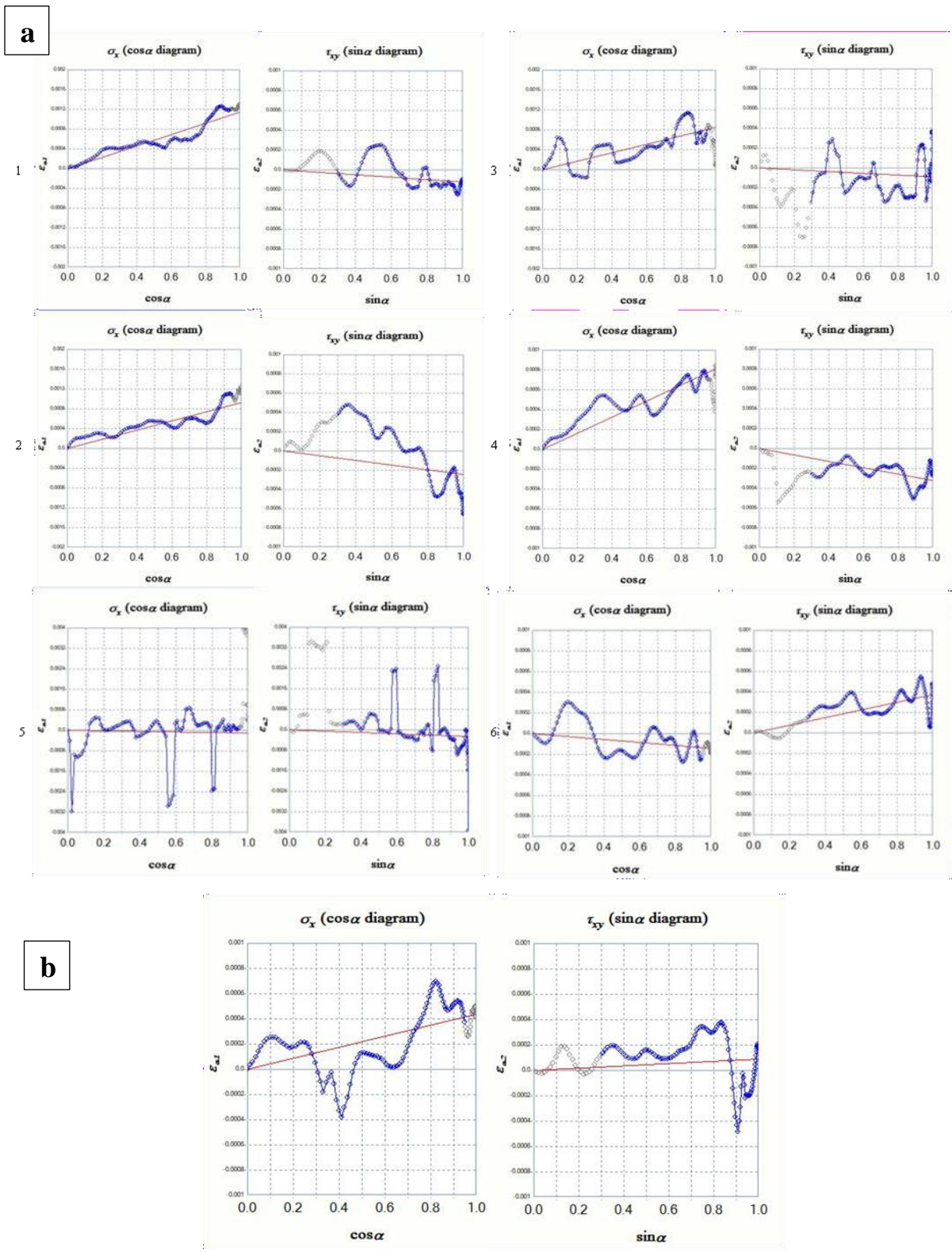
Fig 4.18 cos α and sin α diagrams for the (a) SS316L WAAM (b) Wrought Steel

Summary

The tensile testing of the fabricated samples reveals a significant enhancement in mechanical properties, particularly in ductility, when using the CMT process compared to traditional manufacturing methods. This marks a considerable advancement in material performance, demonstrating the effectiveness of the CMT process. The microhardness testing results indicate an uneven temperature distribution throughout the samples, leading to a gradual decrease in hardness from the base to the top. Despite this variation, the uniform microhardness values observed across all zones suggest consistent material behavior, which helps minimize the risk of brittle failure. However, it should be noted that the considerable heat accumulation between layers causes a steady decline in hardness as time progresses. The research primarily analyzes average residual stress, with consistent findings across nine samples, all indicating compressive stress values. This compressive stress is beneficial, as it contributes to the fabricated components' overall structural integrity and durability.

4.3 Thermal Properties of SS316L WAAM samples

In this section, the thermal conductivity of SS316L WAAM samples was measured and compared to that of wrought SS316L. The results offer valuable insights into the thermal performance and potential applications of the WAAM-fabricated material. The observed differences in thermal conductivity between the two forms underscore the influence of the additive manufacturing process on the material's properties. This comparison is essential for evaluating the suitability of SS316L WAAM for high-temperature applications. The findings contribute to a better understanding of the thermal characteristics of WAAM-fabricated SS316L.

4.3.1 Thermal Conductivity

Thermal conductivity is a fundamental property of a material that defines its ability to conduct heat. It indicates the speed at which heat is transmitted through the material in response to a

temperature gradient. Materials with high thermal conductivity, such as metals, transfer heat quickly, making them suitable for applications requiring efficient heat dissipation. On the other hand, materials with low thermal conductivity, such as insulators, resist heat flow and are used in applications where retaining heat is important. Principle of LFA is shown in Fig 4.19. The unit of thermal conductivity in the International System of Units (SI) is watts per meter-kelvin (W/m·K). Analysis was performed on LFA shown in Fig 4.20 for the thermal conductivity.
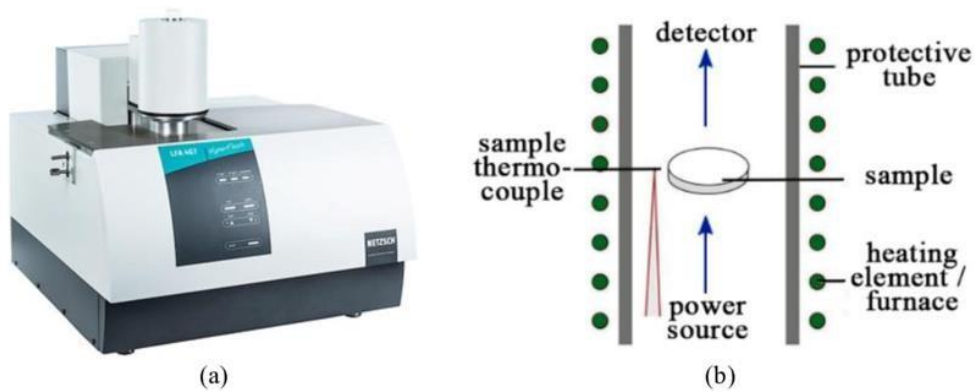
Fig 4.19 (a) Netzsch LFA Thermal Analyser (b) Principle of LFA
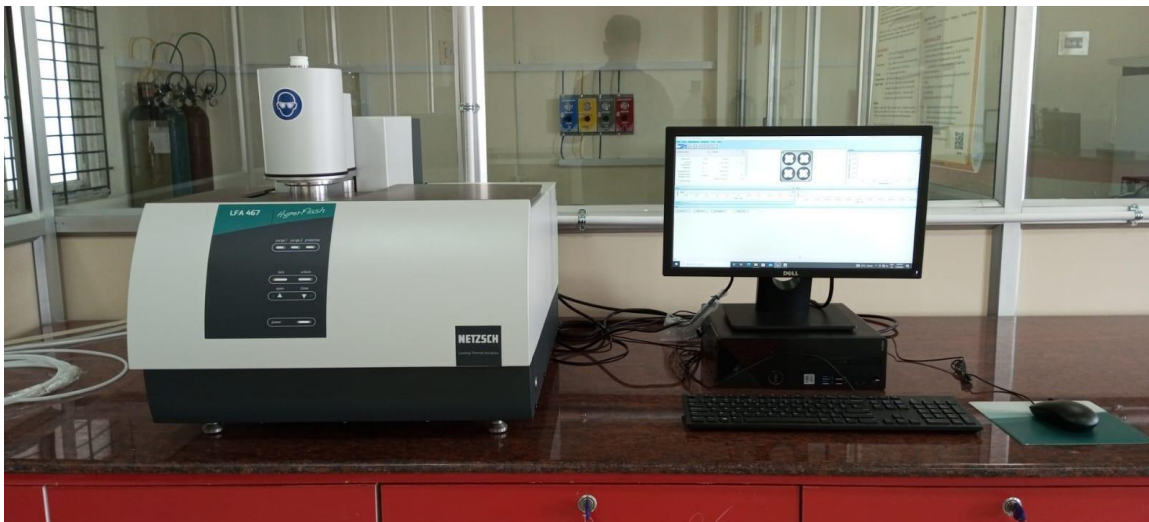
Fig 4.20 Netzsch LFA Thermal Analyser Setup

Fig 4.21 illustrates the variation in thermal conductivity of SS316L WAAM and wrought SS316L across different temperatures. The data reveals that the thermal conductivity of WAAM is greater than that of wrought SS316L. This increased thermal conductivity in WAAM-fabricated SS316L can be attributed to its higher density and thermal diffusivity than the wrought counterpart.
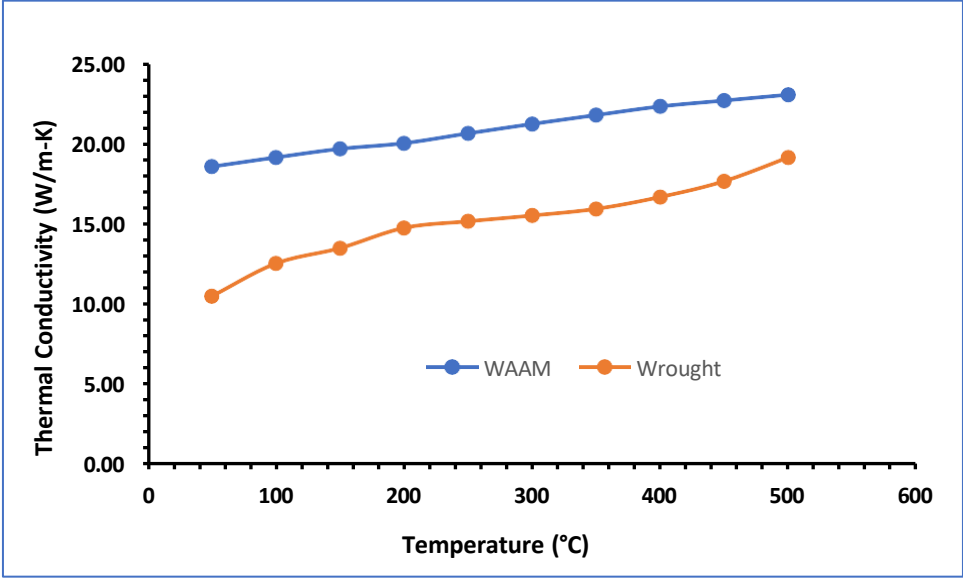
Fig 4.21 Thermal conductivity variation of SS316L WAAM & Wrought Steel

5. Multi-Response Optimization of Input Parameters

In this section optimization of process parameters of CMT-WAAM and their impact on mechanical properties is described. The study initiated additive experiments to explore the effects of input parameters, namely current, welding speed, and CTWD. The authors commenced this study with the primary aims: This study experimentally assesses the influence of process parameters in the CMT process on the mechanical properties of WAAM samples and then optimizes these parameters to obtain the most favorable results i.e. mechanical and microstructural properties across various responses.

5.1 Optimization of Input Parameters

This research aimed to enhance the performance of WAAM-fabricated components by refining key input parameters. The optimization focused on critical input parameters such as I, WS, and CTWD, which are vital in determining the quality and reliability of the final product. These parameters significantly influence heat input, cooling rates, and material deposition characteristics. Achieving consistent and superior mechanical and metallurgical properties without precise optimization remains challenging. To address this, Grey Relation Analysis was employed to optimize the WAAM samples, ensuring improved outcomes in the fabrication process.

5.2 Grey Relational Analysis (GRA)

Decision-making challenges are prevalent in daily life and the workplace, often requiring the identification of the best option from a range of alternatives. Recognizing that no singular alternative is universally optimal for all performance attributes is imperative. A MADM technique, namely GRA, has been utilized as a strategic and practical approach to tackle this issue. Taguchi method is a methodical approach to experimental design and analysis that aims to improve the

quality of the final output. Taguchi method's increasing importance in recent years is evidence of its effectiveness as a potent tool for raising productivity in R&D projects.[150]

Taguchi's tests usually focus on optimizing one quality attribute at once. The Taguchi method and GRA work better to find the best input parameters for various performance indices. An integral component of GRA is the computation of GRCs about various process characteristics. After the computation of GRCs, the GRA is calculated based on the average result of these coefficients. The current research acts as a comprehensive response metric in the framework of Taguchi's experimental design, and the ongoing research makes use of GRA using the response table obtained through the Taguchi method.[151] This optimization is customized to cater to multiple responses, including UTS, MH, and RS. The steps to evaluate and optimize processes with multiple performance criteria effectively are illustrated in Fig 5.1.

```
┌─────────────────────────────────────────────────────────┐
│      L9 orthogonal array and their experimental results    │
└─────────────────────────────────────────────────────────┘
                            ▼
┌─────────────────────────────────────────────────────────┐
│        Normalization of S/N ratio of experimental results  │
└─────────────────────────────────────────────────────────┘
                            ▼
┌─────────────────────────────────────────────────────────┐
│          Determination of deviation sequence and GRC        │
└─────────────────────────────────────────────────────────┘
                            ▼
┌─────────────────────────────────────────────────────────┐
│                  Calculation of GRG and rank               │
└─────────────────────────────────────────────────────────┘
                            ▼
┌─────────────────────────────────────────────────────────┐
│                  Analysis of variance for GRG              │
└─────────────────────────────────────────────────────────┘
                            ▼
┌─────────────────────────────────────────────────────────┐
│     Selection of optimal parameters from response table for GRG │
└─────────────────────────────────────────────────────────┘
                            ▼
┌─────────────────────────────────────────────────────────┐
│                  GRG calculation at optimal level          │
└─────────────────────────────────────────────────────────┘
                            ▼
┌─────────────────────────────────────────────────────────┐
│          Comparison of predicted GRG and experimental GRG   │
└─────────────────────────────────────────────────────────┘
```
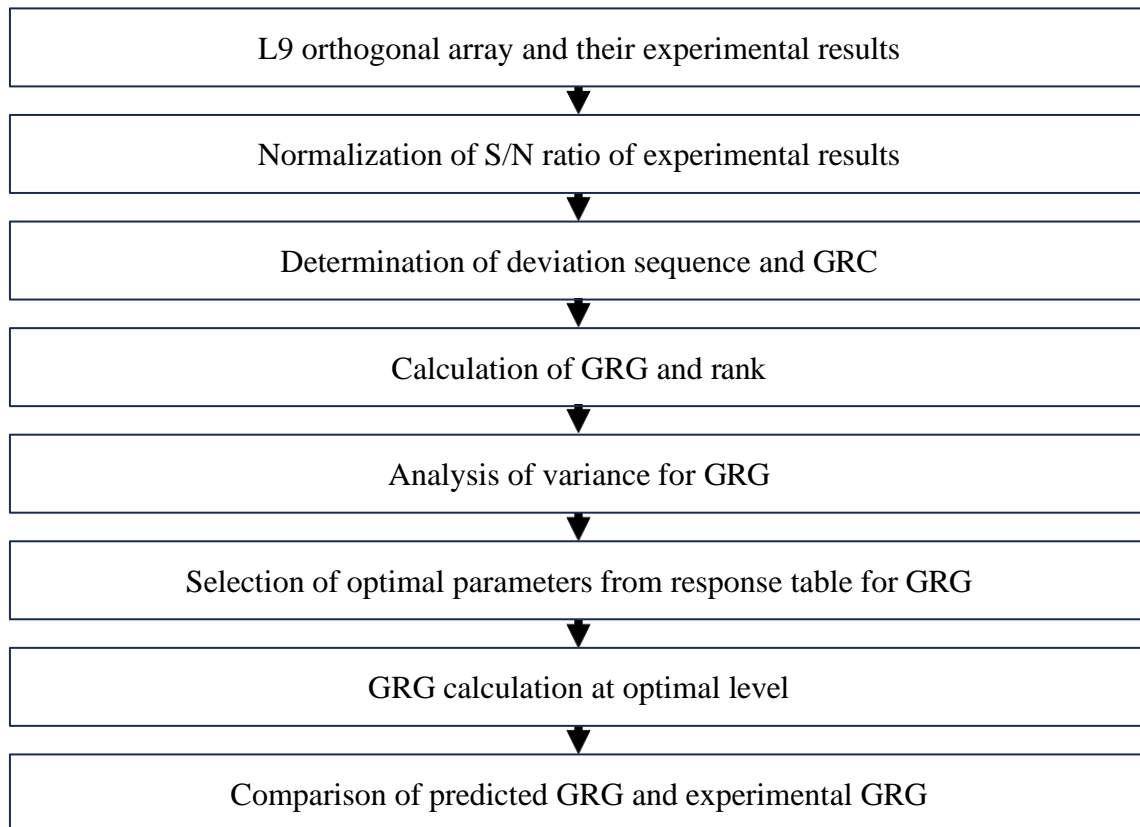
Fig 5.1 Steps followed in Optimization of Input Parameters

5.2.1 Data Pre-Processing

Using GRA requires an initial step of data pre-processing to mitigate variations in range and units observed across distinct data sequences. Additionally, the requirement for data pre-processing becomes apparent when the scatter range within a sequence is notably extensive or when there are variations in the directions of the targets across sequences. The data pre-processing methodology involves two key steps: firstly, the computation of the S/N ratio directly from the original data, and secondly, the conversion of this ratio into a format that facilitates standardized and comparable assessments.[152]

The experimental trials were conducted using the L9 orthogonal array, with a detailed record of the corresponding responses provided in Table 5.1. The S/N ratio for each response, adhering to a larger-the-better criterion, is computed utilizing Equation 1. The fabricated samples' MH, UTS, and RS are the significant responses in wire arc additive manufacturing.

$$ {}^S\!/_N \; ratio(\mu) \; = \; -10 \, log_{10} \left(\frac{1}{n}\right) \sum_{i=1}^{n} \frac{1}{y_{ij}^2} \qquad 1 $$

$$ where, n = number \; of \; replications $$
$$ y_{ij} = observed \; response \; values \; where \; i \; = \; 1,2 \ldots n \; ; j \; = \; 1,2 \ldots k $$

Table 5.1 Experimental results with responses

Sample	A	B	C	Responses		
				MH[1]	UTS[2]	RS[3]
S1	100	0.5	2.5	256.25	562.77	-75.33
S2	100	0.6	3.0	258.75	563.34	-97.32
S3	100	0.7	3.5	269.37	583.88	-56.33
S4	110	0.5	3.0	233.35	587.22	-129.33
S5	110	0.6	3.5	236.75	598.88	-69.66
S6	110	0.7	2.5	257.75	527.22	-144.18

S7	120	0.5	3.5	220.25	505.00	-108.33
S8	120	0.6	2.5	236.50	491.00	-120.25
S9	120	0.7	3.0	238.00	573.33	-87.66

[1]MH was tested at four points, and the mean value is considered.

[2]UTS values were measured in the vertical direction.

[3]RSM was measured at 3 points and the mean value is considered.

To achieve this, it is crucial to normalize the experimental data, bringing it within the standardized range of zero to one. Normalization is achieved through Equation 2 where ($0 \leq x_{ij} \leq 1$) to mitigate the impact of diverse units and minimize variability. This normalization step is essential before applying grey relation theory or alternative methodologies to analyze the original data. To align the values within the same array to approximate 1, an appropriate deduction is made. Notably, the normalization process can have an impact on result rankings. To explore this effect, a comprehensive assessment was conducted to gauge the sensitivity of normalization on sequencing outcomes.

Consequently, an assessment was undertaken to discern the sensitivity of normalization in the context of sequencing results. In light of these findings, we advocate adopting S/N ratio values when normalizing data for GRA. The corresponding values of S/N ratios and normalized S/N values for MH, UTS, and RS are provided in Table 5.2.

$$x_{ij} = \frac{y_{ij} - min\{y_{ij}\}}{max\{y_{ij}\} - min\{y_{ij}\}} \qquad\qquad 2$$

where y_{ij} are the S/N ratio of the responses for a given response j in the experiment, i, the processed value x_{ij} equals 1 or exhibits greater proximity to 1 than values derived from other

experiments, the experiment i is deemed to have the most favorable performance for the given response.

Table 5.2 S/N ratio and normalized S/N ratio values

Sample	S/N ratios			Normalized values of S/N ratios x_{ij}		
	MH	UTS	RS	MH	UTS	RS
S1	52.944	59.778	42.311	0.752	0.687	0.310
S2	53.029	59.787	44.507	0.800	0.692	0.579
S3	53.378	60.098	39.786	1.000	0.872	0.000
S4	52.131	60.147	47.005	0.287	0.901	0.886
S5	52.257	60.318	41.631	0.359	1.000	0.226
S6	52.995	59.211	47.938	0.781	0.358	1.000
S7	51.630	58.837	45.466	0.000	0.142	0.697
S8	52.248	58.593	46.355	0.354	0.000	0.806
S9	52.303	59.939	43.627	0.385	0.780	0.471

5.2.2 Grey Relational Coefficient, Grade and Rank

Next in the process, the determination of how close x_{ij} is to x_{0j} involves utilizing the grey relational coefficient. Greater grey relational coefficient indicates a higher degree of proximity between x_{ij} and x_{0j}. GRC is calculated using Equation 3.

$$\gamma(x_{0j}, x_{ij}) = \frac{\Delta_{min} + \varepsilon\,\Delta_{max}}{\Delta_{ij} + \varepsilon\Delta_{max}} \qquad 3$$

$$i = 1,2, \ldots., m \ and \ j = 1,2, \ldots n$$

$\gamma(x_{0j}, x_{ij})$ is the GRC between x_{0j} & x_{ij}

$$\Delta_{ij} = |x_{0j} - x_{ij}|$$

$$\Delta_{max} = \max(\Delta_{ij}) \text{ and } \Delta_{min} = min\,(\Delta_{ij})$$

$$i = 1, 2, ..., m$$

$$j = 1, 2, ..., n$$

In the present study, the assumed distinguishing coefficient ε is set to 0.5, a value falling within the inclusive range of (0,1]. This coefficient serves as an index for distinguishability and a smaller ε value corresponds to a higher level of distinguishability.

The mathematical expression used for quantification within the grey relational space is referred to as the grey relational grade. This grade is obtained as a weighted sum of grey relational coefficients, and its calculation is dictated by the defined Equation 4.

$$\Gamma\,(X_0, X_i) = \sum_{j=1}^{n} w_{j\gamma}\,(x_{0j}, x_{ij}) \qquad\qquad 4$$

$$for\ i = 1, 2, ..., m$$

Where $\sum_{j=1}^{n} w_{jj} = 1$

The GRG, represented by $\Gamma\,(X_0,\ X_i)$, serves as a metric quantifying the degree of comparability between the sequences X_i and X_0, with X_i being the comparability sequence and X_0 as the reference sequence. The weight assigned to response j is denoted as w_j and typically relies on the judgment of decision-makers. Serving as a vital indicator, the GRG acts as a metric, providing clarity on the level of similarity between the comparability sequence and the reference sequence. Attaining the highest GRG with the reference sequence signifies a close resemblance between the comparability sequence and the reference sequence. Thereby designating the experiment as the preferred choice. Table 5.3. shows GRG, GRC & rank.

Table 5.3 GRC, GRG and Rank

Sample	GRC			Grade	Rank
	MH	UTS	RS		
S1	0.668	0.615	0.420	0.568	6
S2	0.714	0.619	0.543	0.625	4
S3	1.000	0.797	0.333	0.710	2
S4	0.412	0.835	0.814	0.687	3
S5	0.438	1.000	0.393	0.610	5
S6	0.695	0.438	1.000	0.711	1
S7	0.333	0.368	0.622	0.441	9
S8	0.436	0.333	0.720	0.497	8
S9	0.448	0.695	0.486	0.543	7

When the GRG is higher, the associated parameter combination is assigned rank 1 in the experiment context. Experiment number 6, characterized I, WS, and CTWD by a 110 A (level 2), 0.7 m/min (level 3), and 2.5 mm (level 1), respectively, emerges as the closest optimal combination of controllable parameters. Table 5.4 summarizes the means of the GRG corresponding to each input process parameter level. Those entries with a larger GRG are denoted with an asterisk (*), indicating improved multiple performance characteristics. Hence, the optimal parameters for WAAM are specified as the I at 110 A (level 2), WS at 0.7 m/min (level 3), and CTWD of 3.0 mm (level 2), Fig 5.2 displays the graph of the GRG, where the overall mean value obtained from the corresponding table is 0.598.

Table 5.4 Response table for GRG's

Factors	1	2	3	Delta	Rank
A	0.634	0.669*	0.493	0.175	1
B	0.565	0.577	0.654*	0.089	2
C	0.591	0.618*	0.587	0.031	3

The overall mean value derived from the GRG = 0.598

(*) is representing optimal levels of the GRG
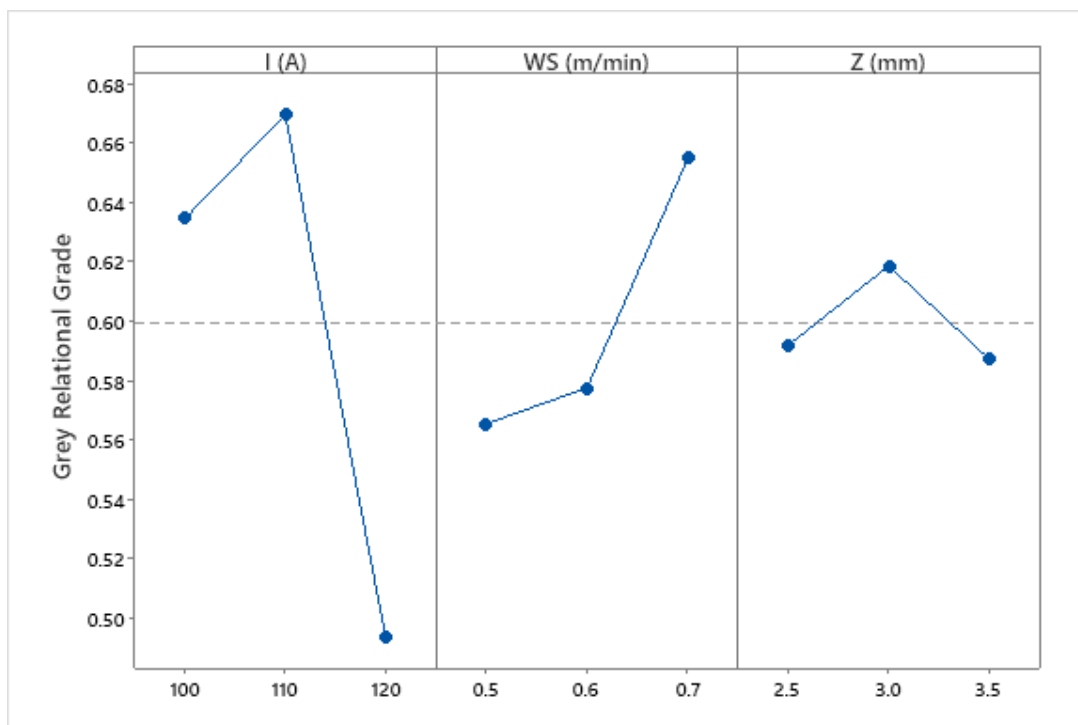
Fig 5.2 GRG Graph

5.3 Analysis of Variance

ANOVA is used as a robust statistical methodology to discern and quantify the notable impact of various controllable parameters on the mechanical properties of WAAM samples. The process involves separating the total variability in GRG's by measuring squared deviations from the average grade. Contributions from individual controllable parameters are identified, along with the

error component. The controllable parameter changes in performance were assessed by determining the contribution percent of each process parameter to the total sum of squared deviations. This determines how much each parameter influences the mechanical properties. ANOVA results in Table 5.5 showcase the impact of different factors on grey relational grades. The I, WS and CTWD contributed 76%, 21%, and 3%, respectively.

Table 5.5 Analysis of Variance

Source	DoF	Adj-SS	Adj-MS	Contribution
I	2	0.051	0.025	76.11%
WS	2	0.014	0.007	20.89%
CTWD	2	0.002	0.001	2.98%
Error	2	0.005	0.003	
Total	8	0.072		

DoF - Degree of freedom, SS - Sum of square, MS - Mean square.

5.4 Confirmation test

The improvement in the mechanical properties of CMT WAAM samples was subjected to a confirmation test. Optimal parameters, outlined in Table 5.4, were chosen for this confirmation test, ensuring consistency with the identified improvements. The equation 5 defines the estimated GRG γ_e using the optimal levels of input parameters.

$$\gamma_e = \gamma_t + \sum_{i=1}^{p}(\gamma_o - \gamma_t) \qquad 5$$

Here, γ_t represents the total mean of GRG, γ_o denotes the mean of the GRG at the optimal level, and p signifies the total number of input parameters.

Executing the confirmation experiment involved setting the input parameters at their optimal levels to validate their significant impact on the mechanical properties of WAAM samples. Table 5.6 presents the results of the confirmation experiment, displaying grey relational grade values for the initial, predicted, and confirmation phases. The observation in Table 5.6 reveals that the relational grade obtained at the optimal input parameters surpasses that of the sixth sample in the orthogonal array, indicating a substantial enhancement.

Table 5.6 Confirmation test & comparison between initial level & optimum level

	Initial parameters in S6 sample	Optimal input parameters	
		Prediction	Experiment
Setting level	$I_2\ WS_3\ Z_1$	$I_2\ WS_3\ Z_2$	$I_2\ WS_3\ Z_2$
UTS (MPa)	527.22		596.2
MH (HV)	257.75		249.3
RS (MPa)	144		120
GRG	0.711	0.745	0.747

Improvement in Grade = 0.036

Summary

Grey relational analysis was employed to optimize the input process parameters for UTS, MH, and RS. The optimal levels identified for I, WS, and CTWD are 110 A, 0.7 m/min, and 3 mm, respectively. These values are recommended as the optimal input parameters to achieve higher UTS, MH, and RS simultaneously. The ANOVA results for the grey relational grade across multiple responses reveal that current is the most significant parameter, with welding speed and CTWD following in importance. At the optimal input parameters, there is an increase in UTS and

MH, with a slight decrease in RS. Additionally, the confirmation results show an increment in the

grey relational grade by 0.036, further validating the optimization.

6. Conclusions & Future Work

The current study establishes WAAM as a highly effective and economically viable additive manufacturing process, particularly beneficial for fabricating large components due to its elevated deposition rates. CMT technology is crucial in enhancing product quality by mitigating defects caused by high thermal gradients, such as cracks. The investigation focused on evaluating the impact of three critical parameters in the CMT-WAAM process: I, WS, and CTWD on the mechanical properties of SS316L austenitic stainless-steel samples. Utilizing Taguchi's L9 orthogonal array and grey relational analysis, the study optimized these parameters to achieve higher UTS, MH, and RS. The optimal levels identified were 110 A for current, 0.7 m/min for welding speed, and 3 mm for CTWD. The ANOVA results highlighted that current is the most influential parameter, followed by welding speed and CTWD. UTS and MH showed an increase at the optimal input parameters, while RS experienced a slight decrease. The confirmation results demonstrated an increment in the grey relational grade by 0.036, validating the optimization. RS analysis revealed compressive RS at the base and tensile residual stress at the top of the samples. The sample fabricated under optimal conditions exhibited a microstructure and EDX profile characteristic of high-quality stainless steel suitable for industrial applications. Thermal conductivity measurements showed that WAAM-fabricated SS316L has greater thermal conductivity than wrought SS316L, attributed to its higher density and thermal diffusivity. The microstructural analysis identified the presence of γ-austenite and δ-ferrite, with significant Cr (21.6%) and Ni (3.6%) enrichment. Both WAAM and wrought SS316L samples showed favorable dendrite orientations with high diffraction peaks at {111} and {200} planes. The tensile fracture surfaces displayed equiaxed dimples and void deposition, indicating a ductile fracture mode and satisfactory toughness.

Overall, this study underscores the potential of WAAM using CMT technology for producing high-quality, structurally sound SS316L components, suitable for various industrial applications.

Future Work

❖ Investigating the performance of WAAM-fabricated SS316L under varying environmental conditions and loading scenarios would provide deeper insights into its suitability for diverse industrial applications.

❖ Develop comprehensive thermal and structural simulations to predict the heat distribution, thermal gradients, and resultant residual stresses during the WAAM process. This can help in fine-tuning process parameters to mitigate issues such as warping and distortion.

References

[1] Y. Zhai, D. A. Lados, and J. L. LaGoy, "Additive Manufacturing: Making Imagination the Major Limitation," *JOM*, vol. 66, no. 5, pp. 808–816, May 2014, doi: 10.1007/s11837-014-0886-2.

[2] T. D. Ngo, A. Kashani, G. Imbalzano, K. T. Q. Nguyen, and D. Hui, "Additive manufacturing (3D printing): A review of materials, methods, applications and challenges," *Compos B Eng*, vol. 143, pp. 172–196, Jun. 2018, doi: 10.1016/j.compositesb.2018.02.012.

[3] A. B. Badiru, V. V. Valencia, and D. Liu, Eds., *Additive Manufacturing Handbook*. CRC Press, 2017. doi: 10.1201/9781315119106.

[4] S. Rouf *et al.*, "Additive manufacturing technologies: Industrial and medical applications," *Sustainable Operations and Computers*, vol. 3, pp. 258–274, 2022, doi: 10.1016/j.susoc.2022.05.001.

[5] S. A. M. Tofail, E. P. Koumoulos, A. Bandyopadhyay, S. Bose, L. O'Donoghue, and C. Charitidis, "Additive manufacturing: scientific and technological challenges, market uptake and opportunities," *Materials Today*, vol. 21, no. 1, pp. 22–37, Jan. 2018, doi: 10.1016/j.mattod.2017.07.001.

[6] M. Javaid, A. Haleem, R. P. Singh, R. Suman, and S. Rab, "Role of additive manufacturing applications towards environmental sustainability," *Advanced Industrial and Engineering Polymer Research*, vol. 4, no. 4, pp. 312–322, Oct. 2021, doi: 10.1016/j.aiepr.2021.07.005.

[7] J. C. Najmon, S. Raeisi, and A. Tovar, "Review of additive manufacturing technologies and applications in the aerospace industry," in *Additive Manufacturing for the Aerospace Industry*, Elsevier, 2019, pp. 7–31. doi: 10.1016/B978-0-12-814062-8.00002-9.

[8] J. C. Vasco, "Additive manufacturing for the automotive industry," in *Additive Manufacturing*, Elsevier, 2021, pp. 505–530. doi: 10.1016/B978-0-12-818411-0.00010-0.

[9] A. Paolini, S. Kollmannsberger, and E. Rank, "Additive manufacturing in construction: A review on processes, applications, and digital planning methods," *Addit Manuf*, vol. 30, p. 100894, Dec. 2019, doi: 10.1016/j.addma.2019.100894.

[10] M. A. G. Calle, M. Salmi, L. M. Mazzariol, M. Alves, and P. Kujala, "Additive manufacturing of miniature marine structures for crashworthiness verification: Scaling technique and experimental tests," *Marine Structures*, vol. 72, p. 102764, Jul. 2020, doi: 10.1016/j.marstruc.2020.102764.

[11] S. Singh and S. Ramakrishna, "Biomedical applications of additive manufacturing: Present and future," *Curr Opin Biomed Eng*, vol. 2, pp. 105–115, Jun. 2017, doi: 10.1016/j.cobme.2017.05.006.

[12] B. Blakey-Milner *et al.*, "Metal additive manufacturing in aerospace: A review," *Mater Des*, vol. 209, p. 110008, Nov. 2021, doi: 10.1016/j.matdes.2021.110008.

[13] L. J. Tan, W. Zhu, and K. Zhou, "Recent Progress on Polymer Materials for Additive Manufacturing," *Adv Funct Mater*, vol. 30, no. 43, Oct. 2020, doi: 10.1002/adfm.202003062.

[14] Y. Lakhdar, C. Tuck, J. Binner, A. Terry, and R. Goodridge, "Additive manufacturing of advanced ceramic materials," *Prog Mater Sci*, vol. 116, p. 100736, Feb. 2021, doi: 10.1016/j.pmatsci.2020.100736.

[15]   J. Allen, "An Investigation into the Comparative Costs of Additive Manufacture vs. Machine from Solid for Aero Engine Parts." [Online]. Available: http://www.rto.nato.int/abstracts.asp.

[16]   B. Blakey-Milner *et al.*, "Metal additive manufacturing in aerospace: A review," *Mater Des*, vol. 209, p. 110008, Nov. 2021, doi: 10.1016/j.matdes.2021.110008.

[17]   M. Shah, D. R.Patel, and S. Pande, "Additive manufacturing integrated Casting- A review," *Mater Today Proc*, vol. 62, pp. 7199–7203, 2022, doi: 10.1016/j.matpr.2022.03.413.

[18]   Y. Huang and M. C. Leu, "Frontiers of Additive Manufacturing Research and Education An NSF Additive Manufacturing Workshop Report −."

[19]   "Metal Additive Manufacturing Market Size, Share, and Trends 2024 to 2034," Sep. 2023.

[20]   A. Vafadar, F. Guzzomi, A. Rassau, and K. Hayward, "Advances in Metal Additive Manufacturing: A Review of Common Processes, Industrial Applications, and Current Challenges," *Applied Sciences*, vol. 11, no. 3, p. 1213, Jan. 2021, doi: 10.3390/app11031213.

[21]   M. Rashid, S. Sabu, A. Kunjachan, M. Agilan, T. Anjilivelil, and J. Joseph, "'Advances in Wire-Arc Additive Manufacturing of Nickel-Based Superalloys: Heat Sources, DfAM Principles, Material Evaluation, Process Parameters, Defect Management, Corrosion Evaluation and Post-Processing Techniques,'" *International Journal of Lightweight Materials and Manufacture*, Jun. 2024, doi: 10.1016/j.ijlmm.2024.05.009.

[22]   S. Kumar, *Additive Manufacturing Processes*. Cham: Springer International Publishing, 2020. doi: 10.1007/978-3-030-45089-2.

[23]   G. Liu *et al.*, "Additive manufacturing of structural materials," *Materials Science and Engineering: R: Reports*, vol. 145, p. 100596, Jul. 2021, doi: 10.1016/j.mser.2020.100596.

[24]   Y. Cao, Y. Zhang, W. Ming, W. He, and J. Ma, "Review: The Metal Additive-Manufacturing Technology of the Ultrasonic-Assisted Wire-and-Arc Additive-Manufacturing Process," *Metals (Basel)*, vol. 13, no. 2, p. 398, Feb. 2023, doi: 10.3390/met13020398.

[25]   V. V. Popov *et al.*, "Powder Bed Fusion Additive Manufacturing Using Critical Raw Materials: A Review," *Materials*, vol. 14, no. 4, p. 909, Feb. 2021, doi: 10.3390/ma14040909.

[26]   D. Svetlizky *et al.*, "Directed energy deposition (DED) additive manufacturing: Physical characteristics, defects, challenges and applications," *Materials Today*, vol. 49, pp. 271–295, Oct. 2021, doi: 10.1016/j.mattod.2021.03.020.

[27]   T. Özel, H. Shokri, and R. Loizeau, "A Review on Wire-Fed Directed Energy Deposition Based Metal Additive Manufacturing," *Journal of Manufacturing and Materials Processing*, vol. 7, no. 1, p. 45, Feb. 2023, doi: 10.3390/jmmp7010045.

[28]   J.-S. Lim, W.-J. Oh, C.-M. Lee, and D.-H. Kim, "Selection of effective manufacturing conditions for directed energy deposition process using machine learning methods," *Sci Rep*, vol. 11, no. 1, p. 24169, Dec. 2021, doi: 10.1038/s41598-021-03622-z.

[29]   N. G. Mbodj, M. Abuabiah, M. El Kandaoui, S. Yaacoubi, and P. Plapper, "Parametric modeling approach in laser wire additive manufacturing process," *Welding in the World*, vol. 67, no. 4, pp. 885–895, Apr. 2023, doi: 10.1007/s40194-022-01454-7.

[30]   T. Pereira, J. V Kennedy, and J. Potgieter, "A comparison of traditional manufacturing vs additive manufacturing, the best method for the job," *Procedia Manuf*, vol. 30, pp. 11–18, 2019, doi: 10.1016/j.promfg.2019.02.003.

[31]   S.-H. Li, P. Kumar, S. Chandra, and U. Ramamurty, "Directed energy deposition of metals: processing, microstructures, and mechanical properties," *International Materials Reviews*, vol. 68, no. 6, pp. 605–647, Aug. 2023, doi: 10.1080/09506608.2022.2097411.

[32]   B. Soundararajan, D. Sofia, D. Barletta, and M. Poletto, "Review on modeling techniques for powder bed fusion processes based on physical principles," *Addit Manuf*, vol. 47, p. 102336, Nov. 2021, doi: 10.1016/j.addma.2021.102336.

[33]   A. H. Alami *et al.*, "Additive manufacturing in the aerospace and automotive industries: Recent trends and role in achieving sustainable development goals," *Ain Shams Engineering Journal*, vol. 14, no. 11, p. 102516, Nov. 2023, doi: 10.1016/j.asej.2023.102516.

[34]   F. Cerejo, D. Gatões, and M. T. Vieira, "Optimization of metallic powder filaments for additive manufacturing extrusion (MEX)," *The International Journal of Advanced Manufacturing Technology*, vol. 115, no. 7–8, pp. 2449–2464, Aug. 2021, doi: 10.1007/s00170-021-07043-0.

[35]   F. Zhang *et al.*, "The recent development of vat photopolymerization: A review," *Addit Manuf*, vol. 48, p. 102423, Dec. 2021, doi: 10.1016/j.addma.2021.102423.

[36]   P. C. Priarone, V. Lunetto, E. Atzeni, and A. Salmi, "Laser powder bed fusion (L-PBF) additive manufacturing: On the correlation between design choices and process sustainability," *Procedia CIRP*, vol. 78, pp. 85–90, 2018, doi: 10.1016/j.procir.2018.09.058.

[37]   H. Wang, A. M. Elliot, and M. P. Paranthaman, "Sintering-based Metal Additive Manufacturing Methods for Magnetic Materials," in *Solid-State Metal Additive Manufacturing*, Wiley, 2024, pp. 361–378. doi: 10.1002/9783527839353.ch16.

[38]   I. Gibson, D. Rosen, B. Stucker, and M. Khorasani, "Material Jetting," in *Additive Manufacturing Technologies*, Cham: Springer International Publishing, 2021, pp. 203–235. doi: 10.1007/978-3-030-56127-7_7.

[39]   D. Svetlizky *et al.*, "Directed energy deposition (DED) additive manufacturing: Physical characteristics, defects, challenges and applications," *Materials Today*, vol. 49, pp. 271–295, Oct. 2021, doi: 10.1016/j.mattod.2021.03.020.

[40]   I. Gibson, D. Rosen, B. Stucker, and M. Khorasani, "Sheet Lamination," in *Additive Manufacturing Technologies*, Cham: Springer International Publishing, 2021, pp. 253–283. doi: 10.1007/978-3-030-56127-7_9.

[41]   T. Blachowicz, G. Ehrmann, and A. Ehrmann, "Metal Additive Manufacturing for Satellites and Rockets," *Applied Sciences*, vol. 11, no. 24, p. 12036, Dec. 2021, doi: 10.3390/app112412036.

[42]   K. Treutler and V. Wesling, "The Current State of Research of Wire Arc Additive Manufacturing (WAAM): A Review," *Applied Sciences*, vol. 11, no. 18, p. 8619, Sep. 2021, doi: 10.3390/app11188619.

[43]   G. Casalino, M. Karamimoghadam, and N. Contuzzi, "Metal Wire Additive Manufacturing: A Comparison between Arc Laser and Laser/Arc Heat Sources," *Inventions*, vol. 8, no. 2, p. 52, Mar. 2023, doi: 10.3390/inventions8020052.

[44]   P. Wanjara, M. Brochu, and M. Jahazi, "Electron Beam Freeform Fabrication on Stainless Steel," *Materials Science Forum*, vol. 539–543, pp. 4938–4943, Mar. 2007, doi: 10.4028/www.scientific.net/MSF.539-543.4938.

[45]   S. Kapil, A. S. Rajput, and R. Sarma, "Hybridization in wire arc additive manufacturing," *Front Mech Eng*, vol. 8, Sep. 2022, doi: 10.3389/fmech.2022.981846.

[46] M. Chaturvedi, E. Scutelnicu, C. C. Rusu, L. R. Mistodie, D. Mihailescu, and A. V. Subbiah, "Wire Arc Additive Manufacturing: Review on Recent Findings and Challenges in Industrial Applications and Materials Characterization," *Metals (Basel)*, vol. 11, no. 6, p. 939, Jun. 2021, doi: 10.3390/met11060939.

[47] M. Srivastava, S. Rathee, A. Tiwari, and M. Dongre, "Wire arc additive manufacturing of metals: A review on processes, materials and their behaviour," *Mater Chem Phys*, vol. 294, p. 126988, Jan. 2023, doi: 10.1016/j.matchemphys.2022.126988.

[48] R. Reisch, T. Hauser, T. Kamps, and A. Knoll, "Robot Based Wire Arc Additive Manufacturing System with Context-Sensitive Multivariate Monitoring Framework," *Procedia Manuf*, vol. 51, pp. 732–739, 2020, doi: 10.1016/j.promfg.2020.10.103.

[49] S. Selvi, A. Vishvaksenan, and E. Rajasekar, "Cold metal transfer (CMT) technology - An overview," *Defence Technology*, vol. 14, no. 1, pp. 28–44, Feb. 2018, doi: 10.1016/j.dt.2017.08.002.

[50] W. Jin, C. Zhang, S. Jin, Y. Tian, D. Wellmann, and W. Liu, "Wire Arc Additive Manufacturing of Stainless Steels: A Review," *Applied Sciences*, vol. 10, no. 5, p. 1563, Feb. 2020, doi: 10.3390/app10051563.

[51] B. O. Omiyale, T. O. Olugbade, T. E. Abioye, and P. K. Farayibi, "Wire arc additive manufacturing of aluminium alloys for aerospace and automotive applications: A review," *Materials Science and Technology*, vol. 38, no. 7, pp. 391–408, May 2022, doi: 10.1080/02670836.2022.2045549.

[52] Z. Lin, K. Song, and X. Yu, "A review on wire and arc additive manufacturing of titanium alloy," *J Manuf Process*, vol. 70, pp. 24–45, Oct. 2021, doi: 10.1016/j.jmapro.2021.08.018.

[53] J. Baby and M. Amirthalingam, "Microstructural development during wire arc additive manufacturing of copper-based components," *Welding in the World*, vol. 64, no. 2, pp. 395–405, Feb. 2020, doi: 10.1007/s40194-019-00840-y.

[54] Yu. F. Ivanov, K. A. Osintsev, V. E. Gromov, S. V. Konovalov, and I. A. Panchenko, "Deformation Behavior of a High-Entropy Al–Co–Cr–Fe–Ni Alloy Fabricated by Means of Wire-Arc Additive Manufacturing," *Steel in Translation*, vol. 51, no. 1, pp. 27–32, Jan. 2021, doi: 10.3103/S0967091221010046.

[55] J. Liu, Y. Xu, Y. Ge, Z. Hou, and S. Chen, "Wire and arc additive manufacturing of metal components: a review of recent research developments," *The International Journal of Advanced Manufacturing Technology*, vol. 111, no. 1–2, pp. 149–198, Nov. 2020, doi: 10.1007/s00170-020-05966-8.

[56] J. Z. Li, M. R. Alkahari, N. A. B. Rosli, R. Hasan, M. N. Sudin, and F. R. Ramli, "Review of Wire Arc Additive Manufacturing for 3D Metal Printing," *International Journal of Automation Technology*, vol. 13, no. 3, pp. 346–353, May 2019, doi: 10.20965/ijat.2019.p0346.

[57] S. Chauhan and A. Narasimhulu, "Comprehensive Study on Wire Arc Additive Manufacturing (WAAM)," 2024, pp. 281–305. doi: 10.1007/978-981-99-5613-5_22.

[58] J. Xiong, Y.-J. Li, Z.-Q. Yin, and H. Chen, "Determination of Surface Roughness in Wire and Arc Additive Manufacturing Based on Laser Vision Sensing," *Chinese Journal of Mechanical Engineering*, vol. 31, no. 1, p. 74, Dec. 2018, doi: 10.1186/s10033-018-0276-8.

[59] H. E. Coules, "Contemporary approaches to reducing weld induced residual stress," *Materials Science and Technology*, vol. 29, no. 1, pp. 4–18, Jan. 2013, doi: 10.1179/1743284712Y.0000000106.

[60] W. J. Sames, F. A. List, S. Pannala, R. R. Dehoff, and S. S. Babu, "The metallurgy and processing science of metal additive manufacturing," *International Materials Reviews*, vol. 61, no. 5, pp. 315–360, Jul. 2016, doi: 10.1080/09506608.2015.1116649.

[61] C. Li, Z. Y. Liu, X. Y. Fang, and Y. B. Guo, "Residual Stress in Metal Additive Manufacturing," *Procedia CIRP*, vol. 71, pp. 348–353, 2018, doi: 10.1016/j.procir.2018.05.039.

[62] A. Busachi, J. Erkoyuncu, P. Colegrove, F. Martina, and J. Ding, "Designing a WAAM Based Manufacturing System for Defence Applications," *Procedia CIRP*, vol. 37, pp. 48–53, 2015, doi: 10.1016/j.procir.2015.08.085.

[63] W. J. Sames, F. A. List, S. Pannala, R. R. Dehoff, and S. S. Babu, "The metallurgy and processing science of metal additive manufacturing," *International Materials Reviews*, vol. 61, no. 5, pp. 315–360, Jul. 2016, doi: 10.1080/09506608.2015.1116649.

[64] C. Panwisawas, Y. Gong, Y. T. Tang, R. C. Reed, and J. Shinjo, "Additive manufacturability of superalloys: Process-induced porosity, cooling rate and metal vapour," *Addit Manuf*, vol. 47, p. 102339, Nov. 2021, doi: 10.1016/j.addma.2021.102339.

[65] W. J. Sames, F. A. List, S. Pannala, R. R. Dehoff, and S. S. Babu, "The metallurgy and processing science of metal additive manufacturing," *International Materials Reviews*, vol. 61, no. 5, pp. 315–360, Jul. 2016, doi: 10.1080/09506608.2015.1116649.

[66] P. Das, R. Nandan, and P. M. Pandey, "A Review on Corrosion Properties of High Entropy Alloys Fabricated by Additive Manufacturing," *Transactions of the Indian Institute of Metals*, vol. 75, no. 10, pp. 2465–2476, Oct. 2022, doi: 10.1007/s12666-022-02610-9.

[67] M. Chaturvedi and S. Arungalai Vendan, *Advanced Welding Techniques*. Singapore: Springer Singapore, 2021. doi: 10.1007/978-981-33-6621-3.

[68] D. K. Singh, "Arc Welding Processes," in *Fundamentals of Manufacturing Engineering*, Singapore: Springer Nature Singapore, 2024, pp. 223–250. doi: 10.1007/978-981-99-8767-2_10.

[69] P. Kah, R. Suoranta, and J. Martikainen, "Advanced gas metal arc welding processes," *The International Journal of Advanced Manufacturing Technology*, vol. 67, no. 1–4, pp. 655–674, Jul. 2013, doi: 10.1007/s00170-012-4513-5.

[70] N. R. Mandal, "Fusion Welding Power Source," 2017, pp. 145–157. doi: 10.1007/978-981-10-2955-4_13.

[71] L. L. Wang, H. L. Wei, J. X. Xue, and T. DebRoy, "Special features of double pulsed gas metal arc welding," *J Mater Process Technol*, vol. 251, pp. 369–375, Jan. 2018, doi: 10.1016/j.jmatprotec.2017.08.039.

[72] R. N. Lumley, "Introduction to aluminium metallurgy," in *Fundamentals of Aluminium Metallurgy*, Elsevier, 2011, pp. 1–19. doi: 10.1533/9780857090256.1.

[73] S. Selvi, A. Vishvaksenan, and E. Rajasekar, "Cold metal transfer (CMT) technology - An overview," *Defence Technology*, vol. 14, no. 1, pp. 28–44, Feb. 2018, doi: 10.1016/j.dt.2017.08.002.

[74] P. N. Bellamkonda, M. Dwivedy, and R. Addanki, "Cold metal transfer technology - A review of recent research developments," *Results in Engineering*, vol. 23, p. 102423, Sep. 2024, doi: 10.1016/j.rineng.2024.102423.

[75] D. Srinivasan, P. Sevvel, I. John Solomon, and P. Tanushkumaar, "A review on Cold Metal Transfer (CMT) technology of welding," *Mater Today Proc*, vol. 64, pp. 108–115, 2022, doi: 10.1016/j.matpr.2022.04.016.

[76] S. Selvi, A. Vishvaksenan, and E. Rajasekar, "Cold metal transfer (CMT) technology - An overview," *Defence Technology*, vol. 14, no. 1, pp. 28–44, Feb. 2018, doi: 10.1016/j.dt.2017.08.002.

[77] D. Varshney and K. Kumar, "Application and use of different aluminium alloys with respect to workability, strength and welding parameter optimization," *Ain Shams Engineering Journal*, vol. 12, no. 1, pp. 1143–1152, Mar. 2021, doi: 10.1016/j.asej.2020.05.013.

[78] TWF The Weld FAB, "Types of Metal Transfer in Welding."

[79] B. Cong, J. Ding, and S. Williams, "Effect of arc mode in cold metal transfer process on porosity of additively manufactured Al-6.3%Cu alloy," *The International Journal of Advanced Manufacturing Technology*, vol. 76, no. 9–12, pp. 1593–1606, Feb. 2015, doi: 10.1007/s00170-014-6346-x.

[80] A. Nouri and C. Wen, "Stainless steels in orthopedics," in *Structural Biomaterials*, Elsevier, 2021, pp. 67–101. doi: 10.1016/B978-0-12-818831-6.00008-2.

[81] G. George and H. Shaikh, "Introduction to Austenitic Stainless Steels," in *Corrosion of Austenitic Stainless Steels*, Elsevier, 2002, pp. 1–36. doi: 10.1533/9780857094018.37.

[82] D. D'Andrea, "Additive Manufacturing of AISI 316L Stainless Steel: A Review," *Metals (Basel)*, vol. 13, no. 8, p. 1370, Jul. 2023, doi: 10.3390/met13081370.

[83] "Materials Science and Engineering_ An Introduction, 10th Australia and New Zealand Edition".

[84] A. Lescur, E. Stergar, J. Lim, S. Hertelé, and R. H. Petrov, "Microstructural investigation and identification of intermetallic σ-phase in solution annealed 316L-type austenitic stainless steel," *Mater Charact*, vol. 182, p. 111524, Dec. 2021, doi: 10.1016/j.matchar.2021.111524.

[85] J. Verma and R. V. Taiwade, "Effect of welding processes and conditions on the microstructure, mechanical properties and corrosion resistance of duplex stainless steel weldments—A review," *J Manuf Process*, vol. 25, pp. 134–152, Jan. 2017, doi: 10.1016/j.jmapro.2016.11.003.

[86] P. S. Gowthaman, S. Jeyakumar, and D. Sarathchandra, "Effect of Heat Input on Microstructure and Mechanical Properties of 316L Stainless Steel Fabricated by Wire Arc Additive Manufacturing," *J Mater Eng Perform*, vol. 33, no. 11, pp. 5536–5546, Jun. 2024, doi: 10.1007/s11665-023-08312-7.

[87] P. Bilmes, A. Gonzalez, C. Llorente, and M. Solari, "Effect of δ ferrite solidification morphology of austenitic stainless steel weld metal on properties of welded joints," *Welding International*, vol. 10, no. 10, pp. 797–808, Jan. 1996, doi: 10.1080/09507119609549091.

[88] H. Abe and Y. Watanabe, "Low-Temperature Aging Characteristics of Type 316L Stainless Steel Welds: Dependence on Solidification Mode," *Metallurgical and Materials Transactions A*, vol. 39, no. 6, pp. 1392–1398, Jun. 2008, doi: 10.1007/s11661-008-9511-8.

[89] Y. Feng and D. Fan, "Investigating the Forming Characteristics of 316 Stainless Steel Fabricated through Cold Metal Transfer (CMT) Wire and Arc Additive Manufacturing," *Materials*, vol. 17, no. 10, p. 2184, May 2024, doi: 10.3390/ma17102184.

[90]   O. Trad, A. Ben Khalifa, F. Zemzemi, H. Hamdi, and B. Louhichi, "Parameters Effect Study on Bead Geometry Deposited by CMT Technology Based Wire Additive Manufacturing (WAAM) Process," 2024, pp. 201–211. doi: 10.1007/978-3-031-47784-3_24.

[91]   Y. Huang, L. Yang, and Q. Xin, "Novel geometrical model and design mechanical parameters for CMT-WAAM stainless steel," *J Constr Steel Res*, vol. 210, p. 108071, Nov. 2023, doi: 10.1016/j.jcsr.2023.108071.

[92]   J. Junwen *et al.*, "CMT-based wire arc additive manufacturing of Inconel 625 alloy," *Emerging Materials Research*, vol. 12, no. 3, pp. 315–322, Sep. 2023, doi: 10.1680/jemmr.23.00053.

[93]   D. D'Andrea, "Additive Manufacturing of AISI 316L Stainless Steel: A Review," *Metals (Basel)*, vol. 13, no. 8, p. 1370, Jul. 2023, doi: 10.3390/met13081370.

[94]   M. Nabeel, A. Farooq, S. Miraj, U. Yahya, K. Hamad, and K. M. Deen, "Comparison of the Properties of Additively Manufactured 316L Stainless Steel for Orthopedic Applications: A Review," *World Scientific Annual Review of Functional Materials*, vol. 01, Jan. 2023, doi: 10.1142/S281092282230001X.

[95]   J. P. Kumar, R. A. Prakash, and R. J. Raman, "Wire ARC Additive Manufacturing of Functional Metals - A Review," *International Journal of Research and Review*, vol. 10, no. 6, pp. 572–589, Jun. 2023, doi: 10.52403/ijrr.20230671.

[96]   Y. Zhao, Y. Chen, Z. Wang, J. Ye, and W. Zhao, "Mechanical properties, microstructural characteristics and heat treatment effects of WAAM stainless-steel plate material," *Journal of Building Engineering*, vol. 75, p. 106988, Sep. 2023, doi: 10.1016/j.jobe.2023.106988.

[97]   A. Karpagaraj, S. Baskaran, T. Arunnellaiappan, and N. R. Kumar, "A review on the suitability of wire arc additive manufacturing (WAAM) for stainless steel 316," 2020, p. 050001. doi: 10.1063/5.0004148.

[98]   W. Wu, J. Xue, L. Wang, Z. Zhang, Y. Hu, and C. Dong, "Forming Process, Microstructure, and Mechanical Properties of Thin-Walled 316L Stainless Steel Using Speed-Cold-Welding Additive Manufacturing," *Metals (Basel)*, vol. 9, no. 1, p. 109, Jan. 2019, doi: 10.3390/met9010109.

[99]   U. Gürol, E. Kocaman, S. Dilibal, and M. Koçak, "A comparative study on the microstructure, mechanical properties, wear and corrosion behaviors of SS 316 austenitic stainless steels manufactured by casting and WAAM technologies," *CIRP J Manuf Sci Technol*, vol. 47, pp. 215–227, Dec. 2023, doi: 10.1016/j.cirpj.2023.10.005.

[100]   J. Vora, H. Parmar, R. Chaudhari, S. Khanna, M. Doshi, and V. Patel, "Experimental investigations on mechanical properties of multi-layered structure fabricated by GMAW-based WAAM of SS316L," *Journal of Materials Research and Technology*, vol. 20, pp. 2748–2757, Sep. 2022, doi: 10.1016/j.jmrt.2022.08.074.

[101]   L. B. O. Souza, M. R. N. Santos, R. P. Garcia, D. B. Fernandes, and L. O. Vilarinho, "Characterization of an austenitic stainless steel preform deposited by wire arc additive manufacturing," *The International Journal of Advanced Manufacturing Technology*, vol. 123, no. 9–10, pp. 3673–3686, Dec. 2022, doi: 10.1007/s00170-022-10382-1.

[102]   J. P. Pragana, I. M. Bragança, L. Reis, C. M. Silva, and P. A. Martins, "Formability of wire-arc deposited AISI 316L sheets for hybrid additive manufacturing applications," *Proceedings of the Institution of Mechanical Engineers, Part L: Journal of Materials:*

Design and Applications, vol. 235, no. 12, pp. 2839–2850, Dec. 2021, doi: 10.1177/14644207211037033.

[103] V. T. Le *et al.*, "Prediction and optimization of processing parameters in wire and arc-based additively manufacturing of 316L stainless steel," *Journal of the Brazilian Society of Mechanical Sciences and Engineering*, vol. 44, no. 9, p. 394, Sep. 2022, doi: 10.1007/s40430-022-03698-2.

[104] R. Chaudhari, H. Parmar, J. Vora, and V. K. Patel, "Parametric Study and Investigations of Bead Geometries of GMAW-Based Wire–Arc Additive Manufacturing of 316L Stainless Steels," *Metals (Basel)*, vol. 12, no. 7, p. 1232, Jul. 2022, doi: 10.3390/met12071232.

[105] R. P. Meena, N. Yuvaraj, and Vipin, "Optimization of process parameters of cold metal transfer welding-based wire arc additive manufacturing of super Duplex stainless steel using response surface methodology," *Proceedings of the Institution of Mechanical Engineers, Part E: Journal of Process Mechanical Engineering*, Feb. 2024, doi: 10.1177/09544089241230878.

[106] R. P. Meena, N. Yuvaraj, and V. Vipin, "Investigations and Optimization of Cold Metal Transfer-based WAAM Process Parameters for Fabrication of Inconel 718 Samples using Response Surface Methodology," *Arab J Sci Eng*, Apr. 2024, doi: 10.1007/s13369-024-08947-1.

[107] R. Mamedipaka and S. Thapliyal, "Data-Driven Model for Predicting Tensile Properties of Wire Arc Additive Manufactured 316L Steels and Its Validation," *J Mater Eng Perform*, vol. 33, no. 3, pp. 1083–1091, Feb. 2024, doi: 10.1007/s11665-023-08071-5.

[108] B. Prasanna Nagasai, S. Malarvizhi, and V. Balasubramanian, "A study on wire arc additive manufacturing of 308L austenitic stainless steel cylindrical components: Optimisation, microstructure and mechanical properties," *Proc Inst Mech Eng B J Eng Manuf*, vol. 237, no. 9, pp. 1391–1404, Jul. 2023, doi: 10.1177/09544054221129471.

[109] Y. Koli, S. Arora, S. Ahmad, Priya, N. Yuvaraj, and Z. A. Khan, "Investigations and Multi-response Optimization of Wire Arc Additive Manufacturing Cold Metal Transfer Process Parameters for Fabrication of SS308L Samples," *J Mater Eng Perform*, vol. 32, no. 5, pp. 2463–2475, Mar. 2023, doi: 10.1007/s11665-022-07282-6.

[110] J. S. de Lima, J. F. da Silva Neto, T. M. Maciel, E. A. T. López, R. A. C. de Santana, and T. F. de Abreu Santos, "Effect of wire arc additive manufacturing parameters on geometric, hardness, and microstructure of 316LSi stainless steel preforms," *The International Journal of Advanced Manufacturing Technology*, vol. 131, no. 12, pp. 5981–5996, Apr. 2024, doi: 10.1007/s00170-024-13240-4.

[111] G. G. de Sousa Figueiredo, I. B. de Mello Picchi, M. Lima dos Santos, E. A. T. López, J. P. Oliveira, and T. F. de Abreu Santos, "Parametric study and response optimization for the wire + arc additive manufacturing of 316LSi via pulsed GMAW," *The International Journal of Advanced Manufacturing Technology*, vol. 129, no. 7–8, pp. 3073–3092, Dec. 2023, doi: 10.1007/s00170-023-12470-2.

[112] V. Kumar, A. Mandal, A. K. Das, and S. Kumar, "Parametric study and characterization of wire arc additive manufactured steel structures," *The International Journal of Advanced Manufacturing Technology*, vol. 115, no. 5–6, pp. 1723–1733, Jul. 2021, doi: 10.1007/s00170-021-07261-6.

[113] J. Gu, R. Li, Y. Qiu, H. Yue, B. Liu, and H. Gu, "Microstructure, Mechanical Properties, and Residual Stress Distribution of AISI 316L Stainless Steel Part Fabricated by Laser Metal Deposition," *Scanning*, vol. 2020, pp. 1–10, Jul. 2020, doi: 10.1155/2020/4831798.

[114] P. S. Gowthaman, S. Jeyakumar, and D. T. Sarathchandra, "Experimental characteristics of 316L stainless steel thin wall processed in wire-based arc additive manufacturing process," *Proceedings of the Institution of Mechanical Engineers, Part E: Journal of Process Mechanical Engineering*, Nov. 2023, doi: 10.1177/09544089231213329.

[115] J. Chen *et al.*, "Dynamic mechanical properties of 316L stainless steel fabricated by an additive manufacturing process," *Journal of Materials Research and Technology*, vol. 11, pp. 170–179, Mar. 2021, doi: 10.1016/j.jmrt.2020.12.097.

[116] K. Yang, Q. Wang, Y. Qu, Y. Jiang, and Y. Bao, "Microstructure and Corrosion Resistance of Arc Additive Manufactured 316L Stainless Steel," *Journal of Wuhan University of Technology-Mater. Sci. Ed.*, vol. 35, no. 5, pp. 930–936, Oct. 2020, doi: 10.1007/s11595-020-2339-9.

[117] L. Palmeira Belotti, J. A. W. van Dommelen, M. G. D. Geers, C. Goulas, W. Ya, and J. P. M. Hoefnagels, "Microstructural characterisation of thick-walled wire arc additively manufactured stainless steel," *J Mater Process Technol*, vol. 299, p. 117373, Jan. 2022, doi: 10.1016/j.jmatprotec.2021.117373.

[118] Y. Zhong, Z. Zheng, J. Li, and C. Wang, "Fabrication of 316L nuclear nozzles on the main pipeline with large curvature by CMT wire arc additive manufacturing and self-developed slicing algorithm," *Materials Science and Engineering: A*, vol. 820, p. 141539, Jul. 2021, doi: 10.1016/j.msea.2021.141539.

[119] H. Xu *et al.*, "Effect of in-situ rolling and heat treatment on microstructure, mechanical and corrosion properties of wire-arc additively manufactured 316L stainless steel," *Journal of Materials Research and Technology*, vol. 27, pp. 3349–3361, Nov. 2023, doi: 10.1016/j.jmrt.2023.10.168.

[120] T. A. Rodrigues *et al.*, "Effect of heat treatments on 316 stainless steel parts fabricated by wire and arc additive manufacturing : Microstructure and synchrotron X-ray diffraction analysis," *Addit Manuf*, vol. 48, p. 102428, Dec. 2021, doi: 10.1016/j.addma.2021.102428.

[121] V. T. Le, D. S. Mai, T. K. Doan, and H. Paris, "Wire and arc additive manufacturing of 308L stainless steel components: Optimization of processing parameters and material properties," *Engineering Science and Technology, an International Journal*, vol. 24, no. 4, pp. 1015–1026, Aug. 2021, doi: 10.1016/j.jestch.2021.01.009.

[122] C. Wang, P. Zhu, Y. H. Lu, and T. Shoji, "Effect of heat treatment temperature on microstructure and tensile properties of austenitic stainless 316L using wire and arc additive manufacturing," *Materials Science and Engineering: A*, vol. 832, p. 142446, Jan. 2022, doi: 10.1016/j.msea.2021.142446.

[123] J. Wang, Y. Huo, and J. Fan, "Effect of Heat Inputs on the Microstructures and Properties of 316L Stainless Steel Parts Manufactured by Wire and Arc Additive Manufacturing Processing," *J Mater Eng Perform*, Jun. 2024, doi: 10.1007/s11665-024-09696-w.

[124] V. H. M. *et al.*, "Effects of arc current and travel speed on the processing of stainless steel *via* wire arc additive manufacturing (WAAM) process," *J Adhes Sci Technol*, vol. 38, no. 12, pp. 2222–2239, Jun. 2024, doi: 10.1080/01694243.2023.2289770.

[125] P. Long, D. Wen, J. Min, Z. Zheng, J. Li, and Y. Liu, "Microstructure Evolution and Mechanical Properties of a Wire-Arc Additive Manufactured Austenitic Stainless Steel:

Effect of Processing Parameter," *Materials*, vol. 14, no. 7, p. 1681, Mar. 2021, doi: 10.3390/ma14071681.

[126] C. Li, Z. Y. Liu, X. Y. Fang, and Y. B. Guo, "Residual Stress in Metal Additive Manufacturing," *Procedia CIRP*, vol. 71, pp. 348–353, 2018, doi: 10.1016/j.procir.2018.05.039.

[127] G. G. Goviazin, D. Rittel, and A. Shirizly, "Achieving high strength with low residual stress in WAAM SS316L using flow-forming and heat treatment," *Materials Science and Engineering: A*, vol. 873, p. 145043, May 2023, doi: 10.1016/j.msea.2023.145043.

[128] J. Théodore *et al.*, "Relationship between microstructure, and residual strain and stress in stainless steels in-situ alloyed by double-wire arc additive manufacturing (D-WAAM) process," *Materialia (Oxf)*, vol. 30, p. 101850, Aug. 2023, doi: 10.1016/j.mtla.2023.101850.

[129] J. V. Gordon, C. V. Haden, H. F. Nied, R. P. Vinci, and D. G. Harlow, "Fatigue crack growth anisotropy, texture and residual stress in austenitic steel made by wire and arc additive manufacturing," *Materials Science and Engineering: A*, vol. 724, pp. 431–438, May 2018, doi: 10.1016/j.msea.2018.03.075.

[130] D. Guo *et al.*, "Solidification microstructure and residual stress correlations in direct energy deposited type 316L stainless steel," *Mater Des*, vol. 207, p. 109782, Sep. 2021, doi: 10.1016/j.matdes.2021.109782.

[131] R. Scharf-Wildenhain *et al.*, "Influence of Heat Control on Properties and Residual Stresses of Additive-Welded High-Strength Steel Components," *Metals (Basel)*, vol. 12, no. 6, p. 951, May 2022, doi: 10.3390/met12060951.

[132] G. Feng, H. Wang, Y. Wang, D. Deng, and J. Zhang, "Numerical Simulation of Residual Stress and Deformation in Wire Arc Additive Manufacturing," *Crystals (Basel)*, vol. 12, no. 6, p. 803, Jun. 2022, doi: 10.3390/cryst12060803.

[133] "KR 8 R1440-2 arc HW".

[134] D. Shindo and T. Oikawa, "Energy Dispersive X-ray Spectroscopy," in *Analytical Electron Microscopy for Materials Science*, Tokyo: Springer Japan, 2002, pp. 81–102. doi: 10.1007/978-4-431-66988-3_4.

[135] K. Tanaka, "X-ray measurement of triaxial residual stress on machined surfaces by the cosα method using a two-dimensional detector," *J Appl Crystallogr*, vol. 51, no. 5, pp. 1329–1338, Oct. 2018, doi: 10.1107/S1600576718011056.

[136] A. Zavdoveev *et al.*, "Optimization of the pulsed arc welding parameters for wire arc additive manufacturing in austenitic steel applications," *The International Journal of Advanced Manufacturing Technology*, vol. 119, no. 7–8, pp. 5175–5193, Apr. 2022, doi: 10.1007/s00170-022-08704-4.

[137] M. Dinovitzer, X. Chen, J. Laliberte, X. Huang, and H. Frei, "Effect of wire and arc additive manufacturing (WAAM) process parameters on bead geometry and microstructure," *Addit Manuf*, vol. 26, pp. 138–146, Mar. 2019, doi: 10.1016/j.addma.2018.12.013.

[138] P. S. Gowthaman, S. Jeyakumar, and D. Sarathchandra, "Effect of Heat Input on Microstructure and Mechanical Properties of 316L Stainless Steel Fabricated by Wire Arc Additive Manufacturing," *J Mater Eng Perform*, vol. 33, no. 11, pp. 5536–5546, Jun. 2024, doi: 10.1007/s11665-023-08312-7.

[139] R. P. Meena, N. Yuvaraj, and V. Vipin, "Investigations and Optimization of Cold Metal Transfer-based WAAM Process Parameters for Fabrication of Inconel 718 Samples using

Response Surface Methodology," *Arab J Sci Eng*, Apr. 2024, doi: 10.1007/s13369-024-08947-1.

[140] V. T. Le *et al.*, "Prediction and optimization of processing parameters in wire and arc-based additively manufacturing of 316L stainless steel," *Journal of the Brazilian Society of Mechanical Sciences and Engineering*, vol. 44, no. 9, p. 394, Sep. 2022, doi: 10.1007/s40430-022-03698-2.

[141] L. B. O. Souza, M. R. N. Santos, R. P. Garcia, D. B. Fernandes, and L. O. Vilarinho, "Characterization of an austenitic stainless steel preform deposited by wire arc additive manufacturing," *The International Journal of Advanced Manufacturing Technology*, vol. 123, no. 9–10, pp. 3673–3686, Dec. 2022, doi: 10.1007/s00170-022-10382-1.

[142] V. Kumar, S. Dwivedi, A. Mandal, and A. R. Dixit, "Experimental investigations on the microstructural evolution and their influence on mechanical, tribological and corrosion performance of wire-arc additive manufactured SS316L structure," *Mater Today Commun*, vol. 38, p. 107673, Mar. 2024, doi: 10.1016/j.mtcomm.2023.107673.

[143] M. Dinovitzer, X. Chen, J. Laliberte, X. Huang, and H. Frei, "Effect of wire and arc additive manufacturing (WAAM) process parameters on bead geometry and microstructure," *Addit Manuf*, vol. 26, pp. 138–146, Mar. 2019, doi: 10.1016/j.addma.2018.12.013.

[144] V. Kumar, S. Dwivedi, A. Mandal, and A. R. Dixit, "Experimental investigations on the microstructural evolution and their influence on mechanical, tribological and corrosion performance of wire-arc additive manufactured SS316L structure," *Mater Today Commun*, vol. 38, p. 107673, Mar. 2024, doi: 10.1016/j.mtcomm.2023.107673.

[145] S.-W. Han *et al.*, "Parameter Optimization of WAAM with Pulsed GMAW for Manufacturing Propeller-Shaped Blade," *International Journal of Precision Engineering and Manufacturing*, vol. 24, no. 7, pp. 1103–1110, Jul. 2023, doi: 10.1007/s12541-023-00797-5.

[146] N. Brubaker *et al.*, "Investigating Microstructure and Properties of 316L Stainless Steel Produced by Wire-Fed Laser Metal Deposition," *J Mater Eng Perform*, vol. 31, no. 5, pp. 3508–3519, May 2022, doi: 10.1007/s11665-021-06477-7.

[147] S. Mahendiran and R. Ramanujam, "Investigation of Surface Residual Stress, Mechanical Properties, and Metallurgical Characterization of Inconel 625 Multilayer Thin-Wall Component Using Cold Metal Transfer Technique," *J Mater Eng Perform*, Jan. 2024, doi: 10.1007/s11665-023-09119-2.

[148] S. Yusuf, Y. Chen, R. Boardman, S. Yang, and N. Gao, "Investigation on Porosity and Microhardness of 316L Stainless Steel Fabricated by Selective Laser Melting," *Metals (Basel)*, vol. 7, no. 2, p. 64, Feb. 2017, doi: 10.3390/met7020064.

[149] G. G. Goviazin, D. Rittel, and A. Shirizly, "Achieving high strength with low residual stress in WAAM SS316L using flow-forming and heat treatment," *Materials Science and Engineering: A*, vol. 873, p. 145043, May 2023, doi: 10.1016/j.msea.2023.145043.

[150] D. M. Neto, M. F. Borges, E. R. Sérgio, and F. V. Antunes, "Effect of Residual Stresses on Fatigue Crack Growth: A Numerical Study Based on Cumulative Plastic Strain at the Crack Tip," *Materials*, vol. 15, no. 6, p. 2156, Mar. 2022, doi: 10.3390/ma15062156.

[151] I. Yadroitsev and I. Yadroitsava, "Evaluation of residual stress in stainless steel 316L and Ti6Al4V samples produced by selective laser melting," *Virtual Phys Prototyp*, vol. 10, no. 2, pp. 67–76, Apr. 2015, doi: 10.1080/17452759.2015.1026045.

[152] Y. Kuo, T. Yang, and G.-W. Huang, "The use of grey relational analysis in solving multiple attribute decision-making problems," *Comput Ind Eng*, vol. 55, no. 1, pp. 80–93, Aug. 2008, doi: 10.1016/j.cie.2007.12.002.

[153] N. D. Ghetiya, K. M. Patel, and A. J. Kavar, "Multi-objective Optimization of FSW Process Parameters of Aluminium Alloy Using Taguchi-Based Grey Relational Analysis," *Transactions of the Indian Institute of Metals*, vol. 69, no. 4, pp. 917–923, May 2016, doi: 10.1007/s12666-015-0581-1.

[154] A. N. Haq, P. Marimuthu, and R. Jeyapaul, "Multi response optimization of machining parameters of drilling Al/SiC metal matrix composite using grey relational analysis in the Taguchi method," *The International Journal of Advanced Manufacturing Technology*, vol. 37, no. 3–4, pp. 250–255, May 2008, doi: 10.1007/s00170-007-0981-4.

RESEARCH PUBLICATIONS:

Publications

The details of the papers in Journal/Conference are as under:

Papers Published/Accepted in SCIE Journals:

I.   **Sudeep Kumar Jain**, Qasim Murtaza, Pushpendra Singh (2024). Investigations and Multi-response Optimization of Process Parameters for SS316L Cold Metal Transfer-Wire Arc Additive Manufactured Samples. Journal of Material Engineering & Performance (SCIE indexed, Impact Factor: 2.2) (Published).

II.   **Sudeep Kumar Jain**, Qasim Murtaza, Pushpendra Singh (2024). CMT-Assisted Wire Arc Additive Manufacturing of SS316L: Fabrication, Characterization, and Fractography. Archives of Metallurgy and Materials (SCIE indexed, Impact Factor: 0.7) (Accepted for Publication)

III. **Sudeep Kumar Jain**, Qasim Murtaza, Pushpendra Singh (2024). Microstructural and Mechanical Characterization of Wire Arc Additive Manufactured Stainless Steel 316L. Archives of Metallurgy and Materials (SCIE indexed, Impact Factor: 0.7) (Accepted for Publication)

IV.   **Sudeep Kumar Jain**, Qasim Murtaza, Pushpendra Singh. Microstructural and Mechanical Properties Analysis of SS316L Structure Fabricated using CMT-Wire Arc Additive Manufacturing. Journal of Adhesion Science & Technology (SCIE indexed, Impact Factor: 2.7) (Published)

Papers presented in International Conferences:

I. **Sudeep Kumar Jain**, Qasim Murtaza, Pushpendra Singh (2024). Experimental Modal Analysis of CMT WAAM and Validation Using Comsol Multiphysics, *Paper presented at*: 10th International Symposium on Fusion of Science and Technology-2024, 04-08 Jan 2024, J C Bose University of Science & Technology, YMCA, Faridabad, Haryana, INDIA

II. **Sudeep Kumar Jain**, Qasim Murtaza, Pushpendra Singh (2022). A Critical Review on Dissimilar Metals Joining Using Cold Metal Transfer (CMT) Welding, Paper presented at: International Conference on Optimization Techniques in Engineering and Technology, 08-09 July 2022, Dronacharya Group of Institutions, Greater Noida

ORIGINAL RESEARCH ARTICLE

Investigations and Multi-response Optimization of Process Parameters for SS316L Cold Metal Transfer-Wire Arc Additive Manufactured Samples

Sudeep Kumar Jain ⬥, Qasim Murtaza, and Pushpendra Singh

Wire and arc additive manufacturing (WAAM) utilizes an electric arc as the primary heat source and solid wire as the material feedstock. Despite potential limitations in precision compared to powder-bed systems, WAAM boasts remarkable deposition rates. This characteristic enables the rapid manufacture of large metallic structural parts, making WAAM a preferred choice for academic research and industrial applications. This study explores the impact of three input process parameters—current (I), welding speed (WS), and Contact Tip to Work Distance (CTWD)—each at three varying levels on three key mechanical properties of SS316L austenitic stainless steel fabricated samples. Through experimentation and analysis, the study evaluates three crucial mechanical properties: ultimate tensile strength (UTS), microhardness (MH), and residual stress (RS). The investigation uses Taguchi's Gray Relational Analysis method, employing an L9 orthogonal array design. Analysis of Variance (ANOVA) has been utilized to assess the impact of parameters on gray relational grade (GRG). The ANOVA analysis for the gray relational grade across various responses indicates that the current is the most significant factor, followed by welding speed and contact tip-to-work distance (CTWD). The contributions of current, welding speed, and CTWD are 76%, 21%, and 3%, respectively. The findings from Gray Relational Analysis (GRA) highlight that optimal performance in terms of maximum UTS, MH, and RS is achieved when employing specific parameter configurations: a I (110 A), WS (0.7 m/min), and CTWD of (3 mm).

1. Introduction

In the realm of advanced manufacturing, Wire Arc Additive Manufacturing (WAAM) stands out as a pioneering technology within the domain of Direct Energy Deposition (DED). Utilizing an electric arc, the welding nozzle positioned at the tip of the arm melts and deposits the metal precisely, aligning with a digital 3D design. The rapid deposition rates, economical utilization of materials and equipment, and consistent structural reliability position WAAM as a disruptive force with the potential to replace conventional manufacturing methods (Ref 1).

In a direct comparison with conventional subtractive manufacturing techniques, the Wire Arc Additive Manufacturing (WAAM) system has shown remarkable time-efficiency gains, cutting fabrication time by 40-60%. This reduction rate is subjected to variation based on the size of the specific component. Simultaneously, post-machining time is streamlined by approximately 15-20% (Ref 2). In welding technology, the Fronius Cold Metal Transfer (CMT) is a refined variation of MIG welding. This unique approach aims to produce high-quality weld beads while minimizing thermal heat input and spatter-free welding (Ref 3). WAAM is a technology of growing importance for the car, aerospace, defense, construction, nuclear energy, and biomedical engineering industries. Maritime and shipbuilding companies increasingly adopt WAAM technology in their design and manufacturing processes. A critical recent development is the creation of ship propellers, known as "WAAMpeller," through a collaborative effort involving RAMLAB, Promarin, Autodesk, Bureau Veritas, and Damen (Ref 4). The aerospace sector is witnessing significant progress in WAAM, the fabrication of substantial components, including large parts, tanks, trusses/spars, and airframes. STELIA Aerospace, based in Toulouse, France, is actively designing aluminum airframes and frame sections as part of this emerging trend (Ref 5). Incorporating WAAM into architectural projects holds great promise for advancing sustainable and innovative growth within the industry. The MX3D Bridge in Amsterdam is the first full-

Sudeep Kumar Jain, Qasim Murtaza, and Pushpendra Singh, Department of Mechanical Engineering, Delhi Technological University, Delhi 110042, India. Contact e-mail: sudeepjain16@gmail.com.

Taylor & Francis
Taylor & Francis Group

Check for updates

Microstructural and mechanical properties analysis of SS 316L structure fabricated using CMT-wire arc additive manufacturing

Sudeep Kumar Jain [ID], Qasim Murtaza [ID] and Pushpendra Singh

Department of Mechanical Engineering, Delhi Technological University, Delhi, India

ABSTRACT

Integrating robotic arm technology with cold metal transfer (CMT) has revolutionized wire arc additive manufacturing (WAAM). The research work consists of the fabrication of SS 316L WAAM using the CMT technique. Investigations of mechanical and microstructural properties, i.e. residual stress measurement (RSM), microhardness (MH), ultimate tensile strength (UTS), percentage elongation (PE), and microstructure of WAAM sample and cold rolled (CR) plate, results were compared. WAAM attained an UTS of 590 MPa, with an average yield strength (YS) of around 302 MPa, exceeding the CR plate's UTS of 557 MPa while maintaining a similar YS of 305 MPa. WAAM and the CR plate exhibited nearly identical PE, with 64% and 62% values, respectively. Residual stress analysis revealed that the WAAM sample showed an average compressive residual stress of 124 MPa, accounting for 87% of the average residual stress observed in the CR plate, which measured 142 MPa. The MH profile of WAAM revealed an average value of 230 $HV_{0.5}$, accounting for 88% of the MH observed in the CR plate at 260 $HV_{0.5}$. The performance of WAAM closely matched that of the CR plate in terms of residual stress and MH.

1. Introduction

In response to the increased demand for the swift production of components and finished goods, this research scrutinizes the substantial alterations in production infrastructure. The study aims to provide valuable insights into the evolving landscape of modern manufacturing. Advancements in manufacturing processes have simplified the fabrication of intricate metal components, contributing to increased efficiency and cost reduction when compared to methods employed in the past, such as casting [1], machining [1,2] and forming [2]. The designated nomenclature for this procedural methodology within academic circles is 'additive manufacturing,' a concept that has retained significance over a considerable span. Producing in three

---

Decision: **accept without changes**

Dear SUDEEP JAIN,

I am pleased to inform you that your manuscript, entitled: Microstructural and Mechanical
Characterization of Wire Arc Additive Manufactured Stainless Steel 316L, has been finally
accepted for publication in Archives of Metallurgy and Materials.

Please be informed that due to a backlog of accepted manuscripts we are not yet able to
allocate your manuscript to a volume and issue. When your manuscript is allocated to an
issue you will receive a pdf proofs for corrections together with DOI number. If any queries
arise when preparing pdf proofs you will be contacted beforehand.

Thank you for submitting your work to us.

Kindest regards,
Prof. Paweł Zięba
Managing Editor
Archives of Metallurgy and Materials

Microstructural and Mechanical Characterization of Wire Arc Additive Manufactured Stainless Steel 316L

Sudeep Kumar Jain[1]*, Qasim Murtaza[1], Pushpendra Singh[1]

[1]Department of Mechanical Engineering, Delhi Technological University, Delhi-110042 (India)

*Corresponding Author: sudeepjain16@gmail.com (Sudeep Kumar Jain)

Abstract:

Robotic arm technology coupled with Cold metal transfer (CMT) has revolutionized Wire arc additive manufacturing (WAAM), gaining widespread recognition in the aerospace, marine, and automotive sectors. In WAAM, managing residual stress poses challenges due to temperature gradients, phase transformations, and uneven cooling, leading to distortion and potential crack failures. This study is centered on the CMT-assisted fabrication of SS 316L WAAM utilizing a 1.2 mm diameter. It involves a comparative analysis of residual stress, microhardness, ultimate tensile strength, and percentage elongation between SS 316L WAAM, and the results were compared with those of wrought SS 316L. The WAAM sample quantified an average residual stress of 90.73 MPa (compressive), marking an 18% increase compared to the wrought stainless steel's residual stress of 76.68 MPa (compressive). The microhardness profile of the WAAM sample revealed an average value of 269.51 HV0.5, signifying a substantial 4.48% increase over the wrought SS 316L microhardness of 257.94 HV0.5. The WAAM sample's ultimate tensile strength was 577 MPa, 16.56% greater than the wrought SS 316L, having an ultimate tensile strength of 495 MPa, while their respective percentage elongation was 86% and 87%. WAAM demonstrated superior performance in terms of ultimate tensile strength, residual stress, and microhardness.

Keywords: SS 316L, WAAM, FESEM, Microhardness, Tensile.

Decision on manuscript AMM-00106-2024-02

1 message

June 26, 2024
AMM-00106-2024-02
CMT Assisted Wire Arc Additive Manufacturing of SS 316L: Fabrication, Characterization, and Fractography

Dear SUDEEP JAIN,

I am pleased to inform you that your manuscript, entitled: CMT Assisted Wire Arc Additive Manufacturing of SS 316L: Fabrication, Characterization, and Fractography, has been finally accepted for publication in Archives of Metallurgy and Materials.

Please be informed that due to a backlog of accepted manuscripts we are not yet able to allocate your manuscript to a volume and issue. When your manuscript is allocated to an issue you will receive a pdf proofs for corrections together with DOI number. If any queries arise when preparing pdf proofs you will be contacted beforehand.

Thank you for submitting your work to us.

Kindest regards,
Prof. Paweł Zięba
Managing Editor
Archives of Metallurgy and Materials

CMT Assisted Wire Arc Additive Manufacturing of SS 316L: Fabrication, Characterization, and Fractography

Sudeep Kumar Jain[1*], Qasim Murtaza[2], Pushpendra Singh[3]

[1,2,3]Department of Mechanical Engineering, Delhi Technological University, Delhi-110042

(India)

*Corresponding Author: sudeepjain16@gmail.com (SUDEEP KUMAR JAIN)

Abstract:

CMT-WAAM, an advanced manufacturing technology, garners significant attention due to its ability to fabricate intricate components efficiently. In this investigation, a 40-layered structure was manufactured from SS 316L using the CMT-WAAM process, with the utilization of optimized process parameters. This research involved the analysis of microstructure and mechanical properties, including microhardness, tensile testing, and fractography, for both WAAM and wrought SS 316L. The UTS of WAAM reached 592.31 MPa and YS of 276.46 MPa, outperforming the UTS of wrought 316L, which was 557.62 MPa, and YS of 284.35 MPa. The PE of WAAM was 59.85%, while for wrought 316L, it was 53.20%, indicating that wrought 316L demonstrated a higher ductility than the WAAM part. The microhardness profile of WAAM showed an average value of 238.14 HV, indicating a 28% increase compared to the MH of wrought 316L, which was measured at 192.37 HV. The microstructure of CMT-WAAM displays δ-ferrite and γ-austenite, along with skeletal and lathy ferrites, similar in wrought 316L. The fractography analysis of tensile specimens exhibited numerous dimples, indicating favorable ductility in the fabricated structure. Therefore, the findings indicate that the CMT-WAAM process meets industrial requirements.

Keywords: WAAM, SS 316L, Tensile Test, Microhardness, Fractography

ISFT-2024.360

10ᵗʰ International Symposium
on
Fusion of Science and Technology– 2024

(ISFT-2024)

CERTIFICATE OF PRESENTATION

This is to certify that

Mr. Sudeep Kumar Jain

Department of Mech. Engeering DTU, Delhi

has presented paper in this conference (ISFT-2024) bearing the title as

Experimental Modal Analysis of CMT WAAM and Validation using Comsol Multiphysics

organized by

J C Bose University of Science & Technology, YMCA, Faridabad, Haryana, INDIA

during 04–08 January 2024.

Prof. Poonam Singhal
(Co-Convener)

Prof. Vikram Singh
(Convener)

Dr. A.P.J. ABDUL KALAM TECHNICAL UNIVERSITY, UTTAR PRADESH, LUCKNOW

INSTITUTION'S INNOVATION COUNCIL (Ministry of HRD Initiative)

DRONACHARYA Group of Institutions | Scopus®

International Conference On
Optimization Techniques In Engineering & Technology

ICOTET 2022

CERTIFICATE OF PARTICIPATION

This certificate is awarded to **Prof./Dr./Mr./Ms.** Sudeep Kumar Jain

for participating/presenting a **paper titled** A critical review on dissimilar

metals joining using cold metal transfer (CMT) welding

in **International Conference On Optimization Techniques In Engineering & Technology,**

Organized by **Dronacharya Group of Institutions, Gr. Noida, (U.P.), India.**

during **8-9 July, 2022**

(Prof. K.K. Saini)
Director

(Prof. Shailesh Kr. Singh)
Convener

(Prof. Pawan Sharma)
Organizing Chair

ICOTET 2022

DELHI TECHNOLOGICAL UNIVERSITY
(Formerly Delhi College of Engineering)
Shahbad Daulatpur, Main Bawana Road, Delhi-42

PLAGIARISM VERIFICATION

Title of the Thesis **"Fabrication And Investigation of 3D Metallic Wire Weld Deposition Using Cold Metal Transfer Technique"**

Total Pages   **122**   Name of Scholar   **Sudeep Kumar Jain**

Supervisor (s)

(1)   **Prof. Qasim Murtaza**

(2)   **Prof. Pushpendra Singh**

Department   **Mechanical Engineering**

This is to report that the above thesis was scanned for similarity detection. Process and outcome is given below:

Software used: **Turnitin**   Similarity Index: **8% after excluding self citations**

Total Word Count: **26129**

Date: **21/11/2024**

Candidate's Signature   **Signature of Supervisor(s)**

PLAGIARISM REPORT

BRIEF PROFILE

I, **Sudeep Kumar Jain**, completed **B.E.** in Mechanical Engineering from **Rajiv Gandhi Proudyogiki Vishwavidyalaya (R.G.P.V), Bhopal, India**, and **M.E** (honors) in **Advanced Production Systems** from **NITTTR (Bhopal, India).** I have enrolled **Ph.D**. in Department of Mechanical Engineering at **Delhi Technological University, Delhi-110042, (India)** under the supervision of **Prof. Qasim Murtaza and Prof. Pushpendra Singh**. I have published **4 SCI/SCIE** papers in the reputed journals.